isvr Institute of Sound and Vibration Research

Semi-Active Isolation of a Single Degree-of-Freedom System using a Magneto-Rheological Damper

P. Jean, P. Gardonio and B.R. Mace

ISVR Technical Memorandum No 955

December 2005

University of Southampton

SCIENTIFIC PUBLICATIONS BY THE ISVR

Technical Reports are published to promote timely dissemination of research results by ISVR personnel. This medium permits more detailed presentation than is usually acceptable for scientific journals. Responsibility for both the content and any opinions expressed rests entirely with the author(s).

Technical Memoranda are produced to enable the early or preliminary release of information by ISVR personnel where such release is deemed to the appropriate. Information contained in these memoranda may be incomplete, or form part of a continuing programme; this should be borne in mind when using or quoting from these documents.

Contract Reports are produced to record the results of scientific work carried out for sponsors, under contract. The ISVR treats these reports as confidential to sponsors and does not make them available for general circulation. Individual sponsors may, however, authorize subsequent release of the material.

UNIVERSITY OF SOUTHAMPTON

INSTITUTE OF SOUND AND VIBRATION RESEARCH

SIGNAL PROCESSING & CONTROL GROUP

Semi-Active Isolation of a Single Degree-of-Freedom System using a Magneto-Rheological Damper

by

P Jean, P Gardonio and B R Mace

ISVR Technical Memorandum N° 955

December 2005

Authorised for issue by
Prof R Allen
Group Chairman

CONTENTS

CONTENTS

ABSTRACT

Vibration isolation is a widespread problem in the systems where it is desired to protect sensitive substructures. This is the case of satellites during their ascent into orbit. In this respect, vibration isolation of launch dynamics loads is a key challenge for the next generation of launchers. Among passive, active, hybrid passive-active and semi-active isolation systems, a semi-active damping solution is very attractive because of the industrial constraints inherent in the launcher environment. A particular controllable damping device, the so-called magneto-rheological damper, has several advantages for semi-active isolation. This document reports a preliminary study of semi-active isolation using magneto-rheological dampers. In the single degree of freedom configuration, semi-active damping is shown to offer interesting isolation performance, particularly for narrowband vibration, but also for broadband disturbances. For this last type of excitation, which is typical of the launch environment, an appropriate semi-active control strategy is implemented and it is shown, both by simulations and by experimental measurements, that the isolation performance is significantly better with a semi-active controlled damper than with any passive damper. This improvement of performance fully justifies the implementation of a semi-active isolation system in a single degree of freedom configuration.

INTRODUCTION

The launch is one of the most severe environments that a spacecraft is subjected to during its lifetime. Large dynamic loads imply stringent design requirements on the spacecraft and the launch environment accounts for much of the expense of designing, qualifying and testing satellite components. Reduction of launch loads would reduce qualifying costs and durations, allow more sensitive equipment to be included in missions and reduce risks of equipment failure. In this context, whole-spacecraft vibration isolation of axial and lateral loads in the frequency range of 5-100 Hz using smart materials is studied. The case study is ARIANE 5 and the excitations taken into account are lift-off (random broadband), booster pressure oscillations (periodic) and shocks (transient).

There are three types of potential approaches to vibration isolation: passive, active and semi-active. Passive isolators featuring viscoelastic materials provide design simplicity and cost-effectiveness. However, passive systems are faced to two main conflicts in the choice of stiffness and damping. The stiffness conflict is the following: a soft mount is desired for a good vibration isolation but leads to high quasi-static deflections. As regards the damping conflict, low damping is suitable for a good high frequency vibration isolation but leads to high resonances of the suspension modes. On the other hand, active isolation systems are not faced to these trade-offs. Active isolators featuring electromagnetic, hydraulic or piezoceramic actuators may provide high control performance over a wide frequency range. However, active isolators require high power sources and all actuators are not suitable to the launch case due to the required strokes or forces. Recently, in order to overcome the disadvantages of active isolators, semi-active isolators have been introduced, which adapt the passive properties of the mount, usually the damping, with a control system. Among them, we focus on magnetorheological (MR) fluid-based semi-active isolators. MR fluids are suspensions of micron-sized, ferro-magnetic particles in an appropriate carrier liquid such as silicon oil. Their essential characteristic is their ability to reversibly change from free flowing, linear viscous liquids to semi-solids having a controllable yield stress in milliseconds when exposed to a magnetic field. When this fluid is used in a damper, this change is manifested by a very large change in the resisting force

of the damper.

The specifications of EADS-ST [1] is the reduction of 12 dB of payload vibration levels in 5-100 Hz frequency range. To attain such a goal, a soft Payload Attach Fitting (PAF), composed of a set of springs in parallel with MR dampers, is investigated. The main anticipated interest of semi-active control using MR dampers, besides intrinsic stability, simplicity and low cost, is to minimise low frequency vibration due to potential resonance of the suspension modes, inherent to passive systems, while adequately attenuating excitations at higher frequencies.

In an exploratory phase, a single degree of freedom isolator using MR dampers has been studied both numerically and experimentally. This report is mainly dedicated to the key issues of this problem.

First, a review of isolation is presented, introducing the concept of semi-active control using MR dampers. Then, in order to make realistic simulations of control, a model of the non-linear behaviour of a commercial MR damper is proposed. In the third part, a theoretical and simulation study of single axis semi-active isolation is carried out. The assumptions made in this work and the performance criteria used to evaluate various control implementations are discussed. Different types of semi-active control laws are tested. Simulation results show promising performance of some control laws, for tonal disturbances as well as certain types of broadband disturbances. The simulation results are finally confirmed by some experimental results in the fourth part. This report ends with some preliminary results on a single axis multiple degrees of freedom configuration.

[1] European Air Defense and Strategy - Space Transportation

CHAPTER 1 REVIEW OF ISOLATION

This sections contains brief reviews of approaches to vibration isolation and the use of Magneto-Rheological (MR) fluids in dampers.

1.1 Classes of isolation systems

1.1.1 Passive isolation

Passive control systems aim to reduce the response in some sensitive region by changing damping, stiffness, mass, or more generally modal properties. However, passive control systems are limited in that they are designed and implemented for certain operating conditions, and hence they can not adapt to some changes of external loading conditions. Here, we are concerned with vibration isolation systems.

In figure 1.1, a single dof passive isolator is shown. The transmissibility transfer function between payload and base displacements, payload and base velocities, or payload and base accelerations is given by

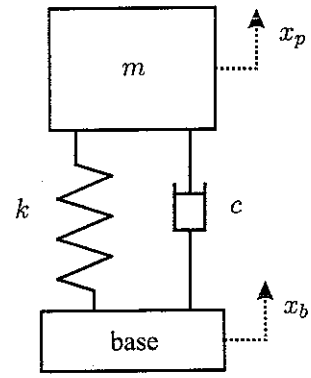

Figure 1.1: Passive single dof isolator.

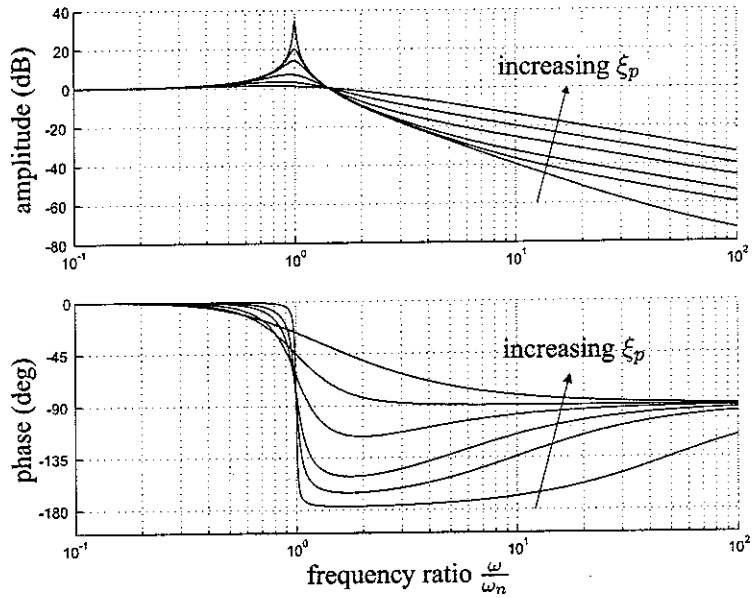

Figure 1.2: Payload/base transmissibility of the passive single dof isolator for ξ_p = [0.01 0.05 0.1 0.25 0.5 1].

$$H_p = \frac{x_p}{x_b} = \frac{\dot{x}_p}{\dot{x}_b} = \frac{\ddot{x}_p}{\ddot{x}_b} = \frac{1 + 2\xi_p \frac{s}{\omega_n}}{1 + 2\xi_p \frac{s}{\omega_n} + \frac{s^2}{\omega_n^2}} \tag{1.1}$$

where s is the Laplace variable, $\omega_n = \sqrt{k/m}$ is the natural frequency and $\xi_p = \frac{c}{2m\omega_n}$ is the passive damping ratio. m is the payload mass, k and c are respectively stiffness and damping of the isolation mount. x_p and x_b are payload and base displacements. The transmissibility modulus and phase for various damping ratios are shown as functions of the frequency ratio $\frac{\omega}{\omega_n}$ in figure 1.2.

From equation 1.1, it can be noticed that for $\frac{\omega}{\omega_n} >> 1$,the decay rate of the modulus of the transmibility is -20dB/dec (except for $\zeta_p = 0$ where it is -40 dB/dec). Notice that at low passive damping ratios, the modulus of the transmissibility has a resonance around $\omega = \omega_n$, which can be large and detrimental to the payload if the base excitation spectrum contains some energy around ω_n. However the advantage of a low damping ratio is that the transmissibility at frequencies above the corner frequency[1] is quite low. The opposite is true for relatively high damping ratios. Figure 1.2 demonstrates the inherent trade-off of passive isolation systems. If we choose a low damping ratio, we gain superior high

[1]the corner frequency ω_c is the non-zero frequency such that $|H_p| = 1$, whatever the damping ratio. Thus, $\omega_c = \frac{\omega_n}{\sqrt{2}}$

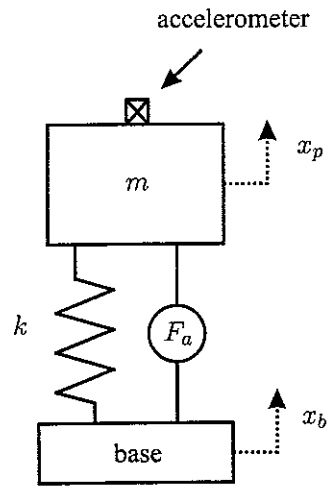

Figure 1.3: Single dof soft active isolator.

frequency isolation but poor resonant frequency control. However, as we increase the damping ratio, we begin to trade off the high frequency isolation for resonance control.

1.1.2 Active isolation

To avoid such a trade-off, we can resort to the use of actuators instead of passive elements. Such a configuration is called active isolation. Contrary to a passive system, an active isolator has the capability to introduce some energy into the structure it is required to isolate. To illustrate active isolation, the well-known control algorithm called "Skyhook Damper Control" (SDC) is discussed. As illustrated in figure 1.3, this control consists of a spring k acting in parallel with a force actuator generating a control force F_a applied to the structure in order to reduce its vibration.

The SDC isolator is based on absolute payload velocity feedback[2]. Indeed, the force F_a is directly proportional to the velocity of the payload. In figure figure 1.4(a), this velocity is estimated by integrating the acceleration $s^2 x_p$ using an integral controller $-c_{sky}/s$. The control force becomes

$$F_a = -c_{sky}\, s\, x_p \tag{1.2}$$

The equivalent representation (figure 1.4(b)) is obvious: the actuator generates a force

[2]the controller based on absolute payload displacement is skyhook spring control

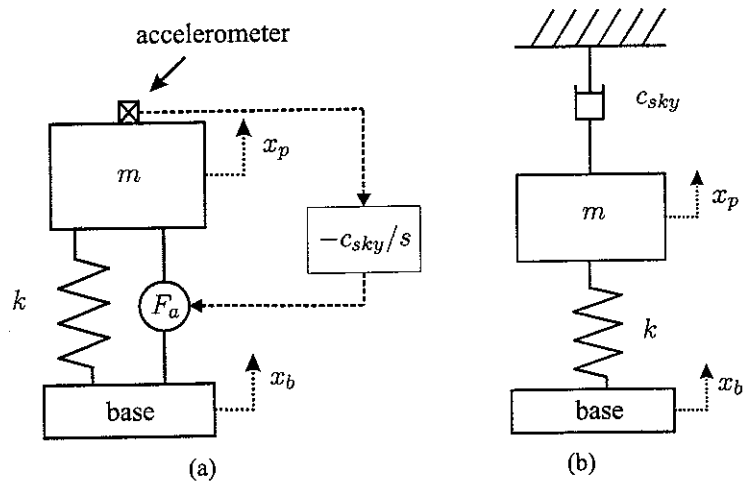

Figure 1.4: (a) Soft isolator with velocity feedback. (b)Equivalent skyhook damper.

equivalent to a damper that is connected to a fixed inertial reference represented as "the sky".

The transmissibility of this configuration is

$$H_a = \frac{\ddot{x}_p}{\ddot{x}_b} = \frac{1}{1 + 2\xi_{sky}\frac{s}{\omega_n} + \frac{s^2}{\omega_n^2}} \tag{1.3}$$

where, in this case, $\xi_{sky} = \frac{c_{sky}}{2m\omega_n}$ is the skyhook damping ratio.

If c_{sky} is chosen in such a way that the system is critically damped ($\xi_{sky} = 1$), we achieve a low-pass filter without overshoot at corner frequency and with a -40dB/dec roll-off as illustrated in figure 1.5. This removes the trade-off of passive isolators. Relating these considerations to the specifications of isolation in a launcher, the modulus of the tranmissibility is -12 dB at $1.73\omega_n$. To provide isolation from 5 Hz upwards, such an isolator should have a natural frequency of at most 2.9 Hz.

The root locus of the closed-loop poles as the gain c_{sky} of the controller increases is shown in figure 1.6, for an isolation frequency of 3 Hz. The open-loop poles are the crosses (complex conjugate poles)located on the imaginary axis. They correspond to the mode of the isolator without damping. The 2 closed-loop poles for a gain such that $\xi_{sky} = 1$ are the crosses on the real axis. These real poles are identical. Continuing increasing the gain of the feedback loop would lead to 2 real poles, one going to zero, the other one going to

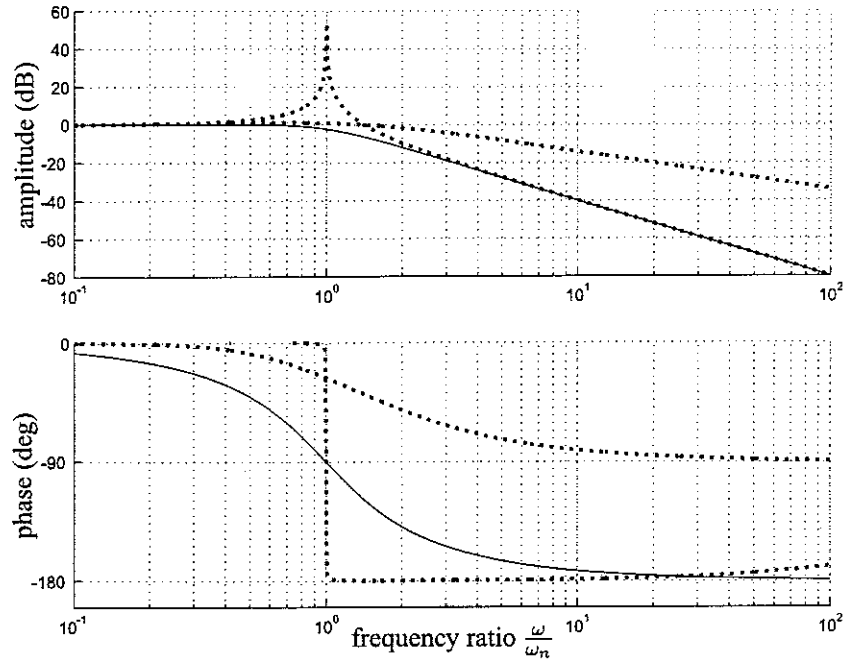

Figure 1.5: Payload/base transmissibility of (-) the skyhook single dof isolator for $\xi_{sky} = 1$ and of (.)passive single dof isolator for $\xi_p = [0.01\ 1]$

$-\infty$. In such a case, the isolation performance is increased around the natural frequency of isolation, but to the detriment of the time response. A far way pole along the real axis leads to long response time, which can be detrimental in position control, which is the primary goal of satellite launch, since the satellite is put into orbit.

An important limitation to the skyhook control approach can be due to the passive response of the isolator. If we include some damping by adding a dashpot in parallel with the spring [3], the transmissibility becomes

$$H_{pa} = \frac{\ddot{x}_p}{\ddot{x}_b} = \frac{1 + 2\xi_p \frac{s}{\omega_n}}{1 + 2\left(\xi_p + \xi_{sky}\right)\frac{s}{\omega_n} + \frac{s^2}{\omega_n^2}} \tag{1.4}$$

If ξ_p is small compared to $\xi_{sky} = 1$, the detrimental effect of added damping becomes visible for high frequencies, as can be seen in figure 1.7. Indeed, at low frequency, the transmisibility of the combined active/passive systems tends to the purely active controller whereas at high frequency, it tends to the transmissibility of the purely passive isolator.

[3] typical of residual damping of the actuation system and the spring

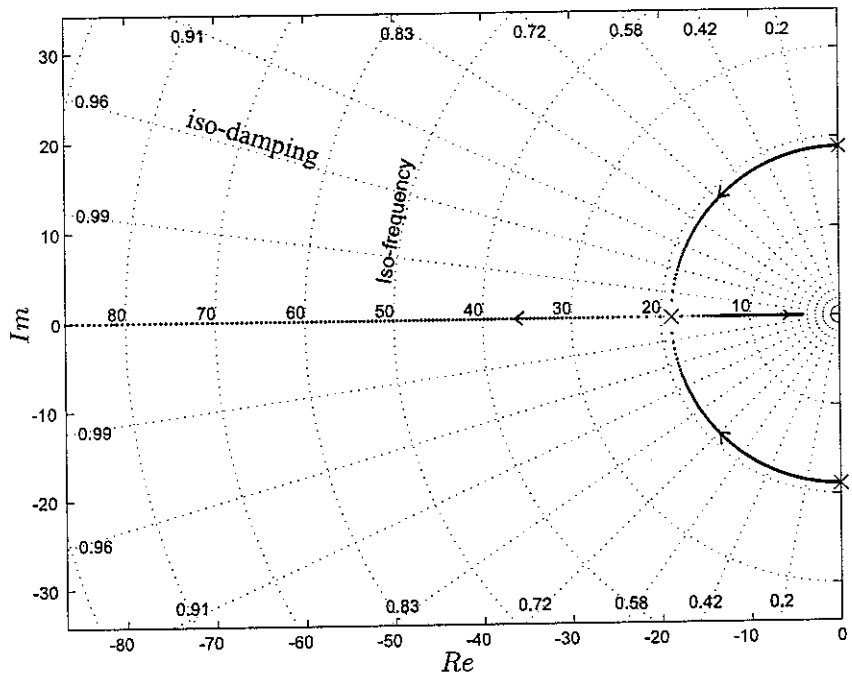

Figure 1.6: Root locus of the skyhook damper for an isolation frequency of 3 Hz (the oblique lines are iso-damping ratio lines, the circle lines are iso-frequency (in rad/s) lines).

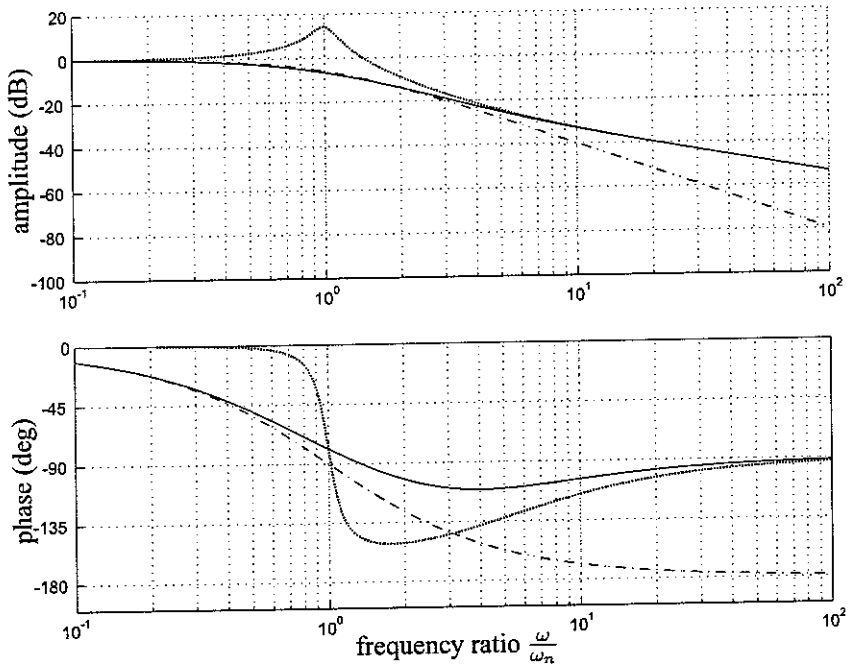

Figure 1.7: Payload/base transmissibilities of (-. pure active skyhook isolation $\xi_{sky} = 1$, $\xi_p = 0$), (. pure passive isolation $\xi_{sky} = 0$, $\xi_p = 0.1$) and (- combined active skyhook $\xi_{sky} = 1$ and passive damping $\xi_p = 0.1$)

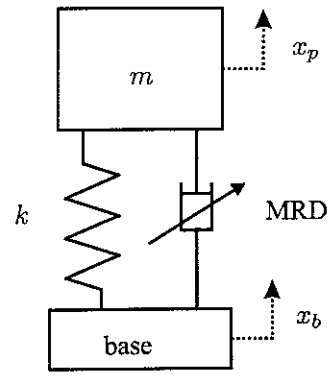

Figure 1.8: Semi-active isolator with a MR damper.

There are numerous studies of the effectiveness of SDC along with other optimal control techniques. Most of these studies indicate that in general SDC is the optimal control policy in terms of its ability to isolate the suspended mass from base excitations [1].

1.1.3 Semi-active isolation

The active isolation system emulating the skyhook damper is very efficient. However, the resulting system requires a significant amount of power, as does many active control systems sofar. Another way of achieving similar performance is to implement a semi-active isolation system.

The semi-active skyhook damper isolator, based on a damping control strategy, is composed of a spring in parallel with an ajustable damper[4], as shown in figure 1.8. Controllable dampers allow for the damping coefficient to be varied between high and low levels of damping. Early semi-active dampers were mechanically adjustable by opening or closing a bypass valve of an hydraulic cylinder. The only power required for the damper is the relatively small power to actuate the valve. For this research, we use a Magneto-Rheological Damper (MRD) for which the damping is varied by changing the magnetic field applied to the magnetorheological fluid. The concept of the MR damper is explained in 1.2.

In active control, the actuator is capable of either supplying or absorbing energy, whereas a semi-active damper is only able to dissipate energy. As a consequence, it can not produce

[4]there exists as well controllable stiffness systems, but they are not as mature as controllable dampers at the moment

a force such as that in equation 1.2. If F_{sa} is the force produced by the semi-active damper, it can be written as

$$F_c = -c_c \left(\dot{x}_p - \dot{x}_b \right) \tag{1.5}$$

where c_c is the controllable damping. The power associated with F_c is only dissipative, that is

$$- F_c \left(\dot{x}_p - \dot{x}_b \right) \geq 0 \tag{1.6}$$

An active controller sometimes demands a control force that is dissipative. Under these circumstances, a semi-active damper is able to provide this force. To illustrate this point, we take the case of the skyhook control strategy. A semi-active damper controlled to emulate this control is called a "semi-active skyhook damper".

The desired force to reproduce the SDC force is $-c_{sky}\dot{x}_p$, as given by equation 1.6. A semi-active damper can provide such a force if and only if $\dot{x}_p \cdot (\dot{x}_p - \dot{x}_b) \geq 0$[5]. If this condition is not satisfied, the power associated with the desired force is no longer dissipative and it is not possible to produce such a force. Thus the well-known semi-active skyhook strategy can be written as

$$F_c = \begin{cases} -c_{sky}\dot{x}_p & \text{if } \dot{x}_p \cdot (\dot{x}_p - \dot{x}_b) \geq 0 \\ \\ 0 & \text{if } \dot{x}_p \cdot (\dot{x}_p - \dot{x}_b) < 0 \end{cases} \tag{1.7}$$

In term of the damping constant of the semi-active damper, equation 1.7 can be rewritten as

$$c_c = \begin{cases} c_{sky}\frac{\dot{x}_p}{\dot{x}_p - \dot{x}_b} & \text{if } \dot{x}_p \cdot (\dot{x}_p - \dot{x}_b) \geq 0 \\ \\ 0 & \text{if } \dot{x}_p \cdot (\dot{x}_p - \dot{x}_b) < 0 \end{cases} \tag{1.8}$$

[5]indeed, the associated power is $P = 1/2 F_c \left(\dot{x}_p - \dot{x}_b \right) = -1/2 c_{sky} \dot{x}_p \left(\dot{x}_p - \dot{x}_b \right)$

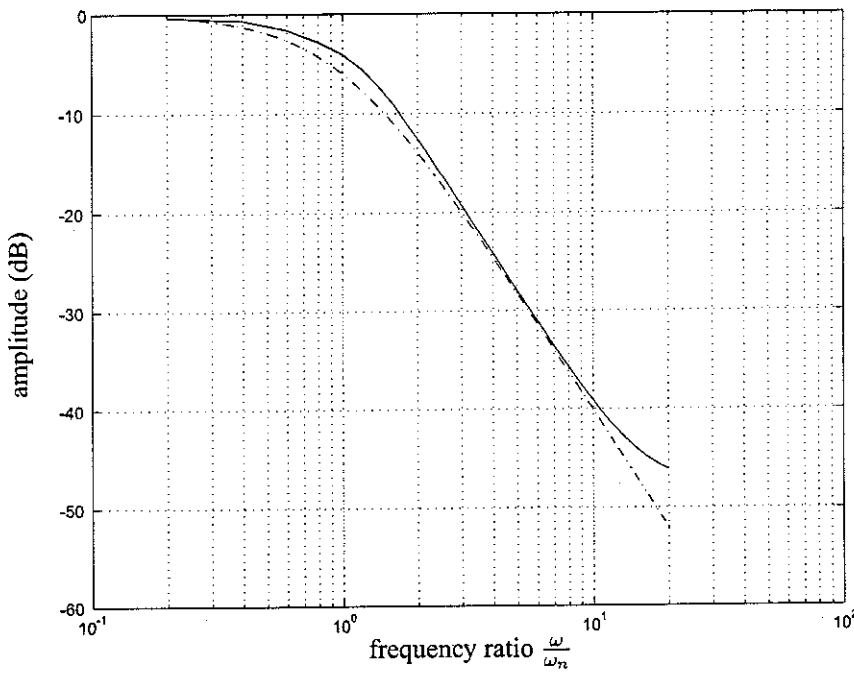

Figure 1.9: Payload/base displacement transmissibilities of -. active skyhook and - equivalent semi-active skyhook.

and in term of the damping ratio $\xi_c = \frac{c_c}{2m\omega_n}$ of the semi-active damper

$$\xi_c = \begin{cases} \xi_{sky}\frac{\dot{x}_p}{\dot{x}_p - \dot{x}_b} & \text{if } \dot{x}_p \cdot (\dot{x}_p - \dot{x}_b) \geq 0 \\ 0 & \text{if } \dot{x}_p \cdot (\dot{x}_p - \dot{x}_b) < 0 \end{cases} \tag{1.9}$$

To illustrate the performance of semi-active isolation, figure 1.9 compares displacement transmissibilities provided by a purely active skyhook control and its semi-active equivalent, apart from any consideration of hardware limitations of the damper, such as its time delays and its limited force range (this point is discussed in section 3.3).

We can observe that in theory, the performance with respect to displacement transmissibility is very similar, even though the semi-active system demands far less energy than active control. However, in practice, hardware limitations result in detrimental effects on performance, as shown in section 3.3.

The concept of semi-active control described above can be generalised to any type of active control law. The general method to emulate an active control law is developed in section 3.2.

1.2 Magneto-Rheological Damper (MRD)

MR fluids are suspensions of micron-sized, ferro-magnetic particles in an appropriate carrier liquid such as silicon oil. Their essential characteristic is their ability to reversibly change from free flowing, linear viscous liquids to semi-solids having a controllable yield stress in milliseconds when exposed to a magnetic field. When this fluid is used in a damper, this change is manifested by a very large change in the resisting force of the damper. This makes them excellent contenders for semi-active devices. However, as they are designed to operate in the "post-yield" region, when the stress exceeds some controllable threshold, this makes them inappropriate for vibrations of small enough amplitude. In the launcher isolation case, however, a preliminary study of excitations showed that displacement amplitudes are of the order of millimeters, which makes MR fluids an appropriate technology.

1.2.1 Principle of action

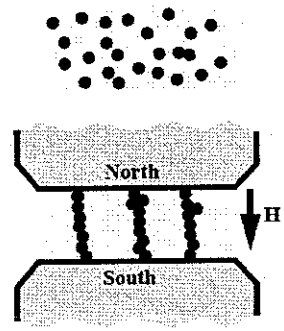

Figure 1.10: Chain-like structure formation under the applied magnetic field.

MR fluids are composed of a carrier fluid and magnetizable particles. When a magnetic field is applied, the particles create columnar structures parallel to the applied field (see figure 1.10). These chain-like structures restrict the flow of the fluid, requiring a minimum shear stress to initiate the flow. This phenomenon is reversible, very fast and consumes very little energy. When no field is applied, the rheological behaviour of the fluid is nearly Newtonian.

To date, several MR fluid devices have been developed for commercial use by the LORD Corporation ([2]; [3]). Linear MR fluid dampers have been designed for use as secondary

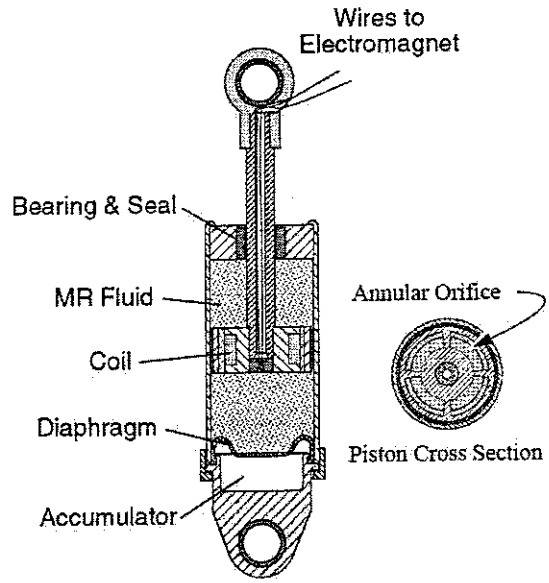

Figure 1.11: Small-scale RD-1005-3 MR fluid damper, by Lord Corporation.

suspension elements in vehicles. The MR damper used in this study is shown in figure 1.11. In such a geometry, the fluid operates in valve mode, i.e. the boundary conditions imposed by the parallel surfaces around the fluid are identical (figure 1.12).

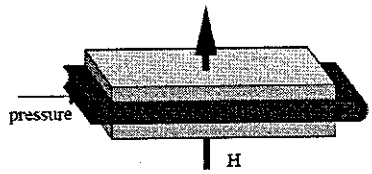

Figure 1.12: Valve mode of flow

1.2.2 Modeling approaches

The quasi-steady behaviour of MR fluids is often represented as a Bingham visco-plastic model ([4], [5], [6]) with a variable yield strength τ_y depending on the applied field H (figure 1.13).

The flow is governed by the equation

$$\tau = \tau_y(H) + \eta\dot{\gamma} \quad , \quad \tau > \tau_y(H) \tag{1.10}$$

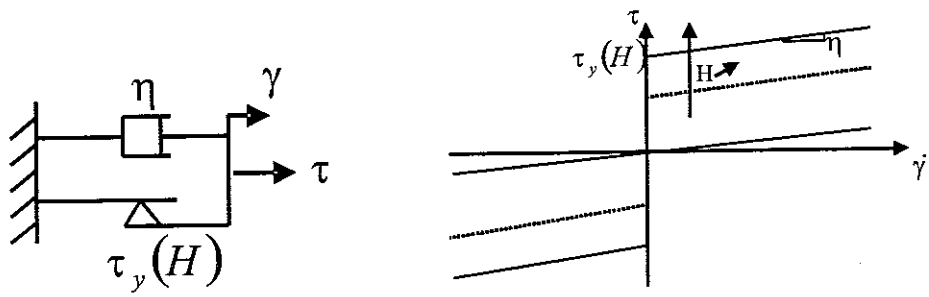

(a) Mechanical analog (b) Behaviour

Figure 1.13: Bingham model

where τ is the shear stress, τ_y the yield stress, γ the shear strain and η the post-yield viscosity. Below the yield stress, (at strains of order 10^{-3}), the fluid behaves visco-elastically [7]. In complex notation, for time harmonic sollicitations, this visco-elastic behaviour is described by

$$\tau = (G' + jG'')\gamma \quad , \quad \tau < \tau_y(H) \tag{1.11}$$

where G' is the shear storage modulus and G'' the shear loss modulus.

Equation 1.10 is valid for high shear strain rates. For a better fitting over a wider range of strain rates, there exist other rheological models such as Herschell-Bulkley ([8], [9]), biviscous([10], [11]) and modified Bingham ([12]). Those studies solve the quasi-steady flow in valve mode (figure 1.12).

Solving the equations of flow inside the valve enables one to find a constitutive relationship between the damper force and piston velocity. However this relationship is valid only for a quasi-steady state motion. In practical applications of vibration control, excitations may include some moderate or high frequencies and the motion may not be steady-state.

In this context, there is no existing predictive model. To predict correctly the dynamic behaviour of a MR damper, the pre-yield behaviour of MR fluids (equation 1.11) should be taken into account in the description of the flow. There exist some theories of visco-elastic flows such as those of polymers or paste flows. Such fluids exhibit a Kelvin-Voigt-like visco-elastic behaviour. These theories use the concept of objective derivatives. For instance, [13] proposes a model that describes a large-amplitude oscillatory shearing flow of a wheat-flour dough, which exhibits a soft solid-like viscoelastic behaviour. Solving the flow of an elasto-visco-plastic controllable fluid would be an interesting research topic,

unexplored at the moment, to the knowledge of the author. There is a clear lack of predictive models for MR devices. Nevertheless, non-predictive models based on experimental characterization have been proposed extensively. A review of some of these models is given in the chapter 2. Basically, three classes of models exist:

- parametric: use of lumped parameters such as Coulomb friction elements, springs, dashpots, masses;
- non-parametric: use of shape functions such as hyperbolic tangent, bilinear (biviscous);
- hybrid models involving both parametric/non-parametric components. These models are generally referred as non-parametric models as well.

The following chapter decribes a model developed for use in the simulation of semi-active control. This model is a hybrid parametric/non-parametric model based on the work of [14].

1.3 Summary

Passive isolation systems have been used for a long time because of their simplicity, but have two major inherent drawbacks:

- the stiffness conflict: trade-off between high attenuation of high frequencies and limitation of quasi-static deflections;
- the damping conflict: trade-off between high attenuation of high frequencies and control of suspension resonance.

Although an active vibration control system is not subject to these trade-offs and has better performance than the best possible passive systems, they are generally more costly, more complex, might be unstable and therefore are often less reliable than passive systems.

An alternative to those concepts of vibration isolation is offered by semi-active systems, among which those using controllable damping devices. In purpose of payload isolation during launch, a semi-active isolation system using Magneto-Rheological dampers is

proposed. These devices offer a continuously variable damping, while having a simple geometry (no movable parts). However, their behaviour is highly non-linear and is difficult to characterize over a wide range of operating conditions (displacement amplitude, frequency, current). Such a characterization is the subject of the following chapter.

For narrowband disturbances, semi-active damping is known not to be subject to the damping conflict, provided the implementation of an appropriate controller. For broadband disturbances, the performance of such systems is more arguable and there is no clear consensus on this point, which is discussed in this report. On the other hand, semi-active damping is subject to the stiffness conflict. To respond to the specifications of launch vibration isolation, a soft isolator is required. Thus, the question, not treated in this report, is whether the available clearance space between the payload and the launcher structure is sufficient. The natural frequency of the isolator should be as low as possible, taking into account this clearance limitation. With the current knowledge we have on this point, suspension frequencies of 2 Hz to 8 Hz are envisaged.

CHAPTER 2 MAGNETO-RHEOLOGICAL DAMPER MODEL

2.1 Review of models

As already seen, the Bingham constitutive equation (see section 1.2.2), which excludes preyield deformation, provides a convenient tool for estimating the relationship between the force capacity of the Magneto-Rheological Damper (MRD), the piston velocity and the current applied to the coil. The Bingham constitutive model does not, however, capture the dynamic behaviour of the MR fluid and MR damper at low transient strain rates and low velocity. Dynamic effects, arising from preyield visco-elasticity inside the valve and bulk compressibility of the fluid chambers, are especially important when the damper velocity changes sign: as seen in figure 2.1, a hysteresis loop due to stiffness effects is present at low velocities and is not captured by the Bingham model.
Because of the complexity of the micro-structural behaviour of MR fluids, there are no predictive models of MR dampers. As a consequence, phenomenological descriptions are adopted. As seen in section 1.2.2, three classes of models exist: parametric, non-parametric and hybrid parametric/non-parametric models.

Parametric models have been widely used. These models are expansions of the Bingham plastic model [15] and one-dimensional mechanical analogues for visco-elasticity, yielding and viscosity: [16], [17], [18] and [19]. The mechanical analogues for the preyield behaviour [1] of the device should be motivated by an analogy with the preyield behaviour of the fluid itself. By carrying out some viscometric measurements on the MR fluid at very low strains and various frequencies (oscillatory shear between two plates), it is possible to extract a linear behaviour that can be modelled by a mechanical analog. Recently, it was claimed in [20] that fluid-like models (such as the Maxwell model) for the preyield regime were not physical. Indeed, it is well-known that MR fluids exhibit a Kelvin-Voigt-like linear viscoelastic behaviour at very low strain (under 0.005) ([7], [21]). That is why fluid-like preyield models are not robust in the frequency domain that is to say that the

[1] Note that the concept of preyield is originally defined from a continuum mechanics point of view for the fluid. The expression has been extended to the scale of the damper because the damper exhibits a visco-plastic behaviour similar to the fluid.

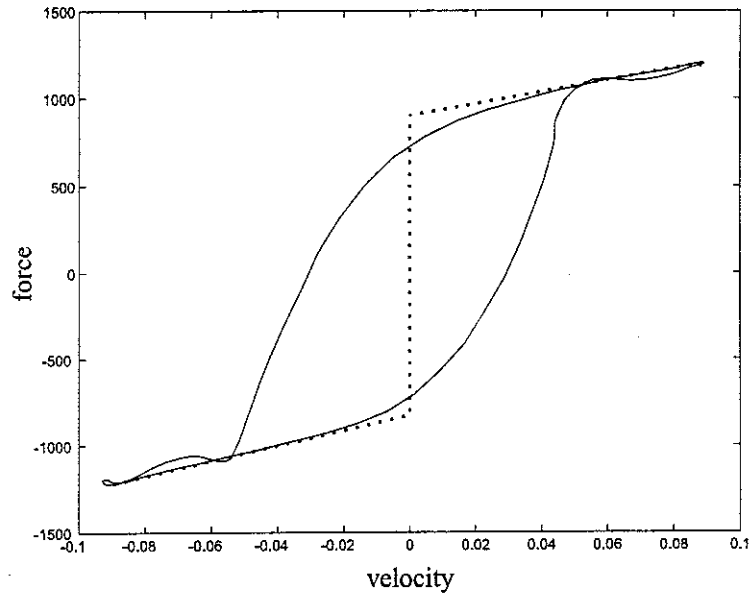

Figure 2.1: Typical behaviour of a MRD in the velocity-force plan: (-) experimental (damper: RD-1005-3, Lord Corp., frequency: 10 Hz, current: 0.9 amp), (..) Bingham model.

elements should be frequency-dependent, which is really inconvenient for simulations. However, the authors of [20] haven't proposed an alternative model, with a solid-like preyield model. Thus, the models encountered in the literature are fluid-like preyield types.

There are very few purely non-parametric models. We can cite [5], which has proposed a hysteretic biviscous function, a conditional bilinear function. Often, the use of algebraic functions is mixed with a parametric model, to produce a hybrid parametric/non-parametric model. Actually, this type of model is commonly referred as non-parametric, and we can thus distinguish two classes of models: parametric and non-parametric.

A very famous hybrid model is the Bouc-Wen model proposed in [22], and the many variations of this model. It utilizes the Bouc-Wen equation for the yielding component and linear elastic, or viscous elements for the hysteretic effects. These models reproduce quite well the behaviour of ER/MR devices, but, however, suffer from a lack of physical meaning and are sometimes quite complicated. The increase in complexity of the model may make it hard to identify relationships between the parameters and the control signal (coil current for the MRD) and difficult to use in control simulations.

In hybrid models (that we henceforth also describe as non-parametric models), shape

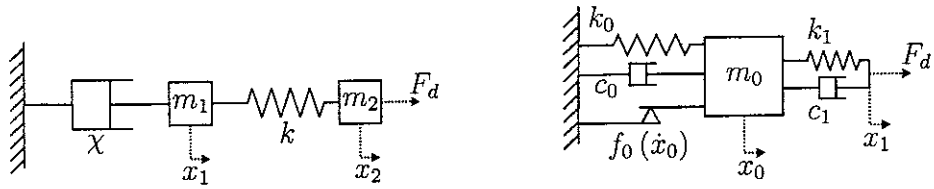

(a) Sims' model (b) Gavin's model

Figure 2.2: Mechanical analogues.

functions are used to capture the yielding process. These shape functions are more elaborate than the classical Bingham model. Shape functions are also referred as quasi-steady functions [14]. On the other hand, the use of lumped parameters in hybrid models is motivated by the hysteretic effect. A simple elastic element in series with the quasi-steady function can capture the hysteretic behaviour well, but sometimes more complicated mechanical analogues are used to offer better frequency robustness. Recently, Sims [14] has proposed a model that incorporates a series combination of a spring, a mass, and a nonlinear biviscous element as a shape function. The mechanical analog is shown in 2.2(a). Though simple, this model offers quite a good reproduction of the MRD behaviour. In this model, the preyield analog is equivalent to a Maxwell fluid model (a spring and a dashpot in series, the dashpot represented the preyield part of the biviscous element). Gavin [23] developed a similar model, shown in 2.2(b). This model uses a hyperbolic tangent function for the quasi-steady state behaviour in series with a Kelvin-Voigt analogue. This model is equivalent in the preyield regime to a three-parameter fluid model. In accordance with figure 2.2(b), the algebraic function proposed in [23] is defined as

$$f_0(\dot{x}_0, H) = f_y(H) tanh\left(\frac{\dot{x}_0}{v_{ref}}\right) \tag{2.1}$$

where f_y is the yield force depending on the control signal H. This function is a smooth variation of a Coulomb friction model and the smoothness is adjusted by v_{ref}, a parameter analogous to a velocity. Putting the damping element c_0 in parallel with the shape function, we recognize a variation on the Bingham model.

Actually, the models presented in figure 2.2 are very similar. In 2.2(b), k_0 and c_1 are added, whereas the second mass $m_2 = 0$. Apart from these differences, Gavin's model proposes a quasi-steady function close to the biviscous function, but smoother at the preyield-postyield transition. These two functions are shown in figure 2.3 and compared to the classical Bingham model.

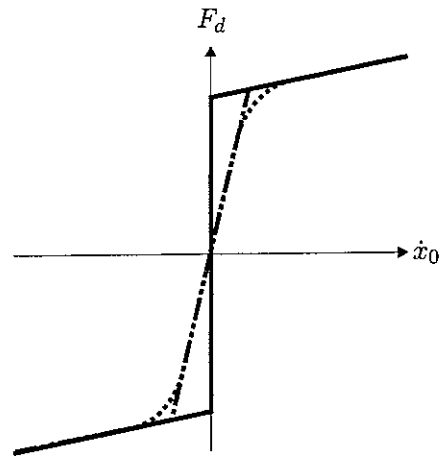

Figure 2.3: Three possible shape function models: (-) Bingham, (-..-) biviscous, (..) hyperbolic tangent.

2.2 Theory

2.2.1 Model format

The proposed model borrows theory from those of Sims [14] and Gavin [23] (see figure 2.2). Modelling the behaviour of MRD is a trade-off between precision and complexity. The model in [14] has the advantage of simplicity, and thus can be easily implemented. Moreover, [14] provides a standard identification procedure that can be automatized easily. On the other hand, the model in [23] is too complicated, but this model offers probably a better robustness with frequency because of the presence of a damping term c_1 and a better representation of the transition between preyield and postyield regimes because of a smooth quasi-steady function. However, there is a parameter that appears useless: k_0. Indeed this stiffness acts especially in the post-yield region (it enlarges the hysteresis loop in the postyield region, which is actually nearly flat), whereas k_1 and c_1 determine the size of the preyield hysteresis loop.

From the literature review, the chosen mechanical analogue for this study is shown in figure 2.4(a). It is very similar to the model in [23] (figure 2.2(b)). However, the method of identification is borrowed from [14]. With the model presented in figure 2.4(a), this identification procedure is impossible to carry out due to the presence of c_{pre}. As a consequence, as a first step the procedure is done with the mechanical analogue shown in figure 2.4(b). This mechanical analogue is very similar to figure 2.2(a), but doesn't have the second mass element m_2 (which is assumed to represent the piston mass, which has

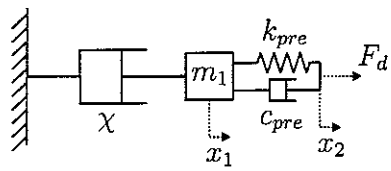

(a) The complete proposed model

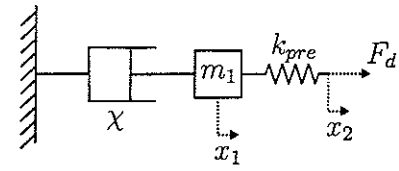

(b) A simplified model for identification purpose

Figure 2.4: Mechanical analogs of the proposed model.

no effect on the behaviour). The preyield damping c_{pre} is added only at the end of the procedure, in order to offer a better frequency robustness.

Thus, the corresponding equations of the lumped-parameter model shown in figure 2.4(b) are

$$\begin{cases} k_{pre}\left(x_2 - x_1\right) - \chi\left(\dot{x}_1, i_c\right) = m_1 \ddot{x}_1 \\ F_d - k_{pre}(x_2 - x_1) = 0 \end{cases} \tag{2.2}$$

where the quasi-steady valve flow is represented by the nonlinear function χ, which is a function of the quasi-steady velocity $\dot{x}_1$ and the control current i_c in the coil of the damper. In this study we use a hyperbolic tangent function for χ instead of the biviscous function used in [14]. This function is smoother in the transition between preyield and postyield, as seen in figure 2.3 and expanded upon in the following section.

2.2.2 Identification procedure

2.2.2.1 Identification of stiffness

According to equations 2.2, the two parameters k_{pre} and m_1 and the function χ are to be identified. The laboratory tests are carried out by imposing the base displacement of the damper, i.e. x_2, and measuring the corresponding force F_d. The quasi-steady velocity $\dot{x}_1$, which is a fictious velocity proportional to the flow velocity inside the valve, is unknown. The aim of the identification procedure is then to estimate the parameters of the model so as to fit these measurements.

It is apparent from equations 2.2 that given an estimate value $\hat{k}_{pre}$ of the stiffness k_{pre}, an

estimate $\hat{x}_1$ of the coordinate x_1 can be determined by

$$\hat{x}_1 = x_2 - \frac{F_d}{\hat{k}_{pre}} \tag{2.3}$$

Moreover, during identification, m_1 is neglected (introducing m_1 is especially useful to decrease the stiffness of the equations and thus improve the convergence of numerical simulations described in section 2.2.3). This enables ones to find that, according to equation 2.2

$$\chi\left(\dot{x}_1, i_c\right) = \hat{k}_{pre}\left(x_2 - \hat{x}_1\right) = F_d \tag{2.4}$$

In [14], the estimation of $\hat{k}_{pre}$ is done graphically by an iterative procedure. Indeed, by definition, the quasi-steady behaviour defined by the function χ is non-hysteretic. As said in [14] "by making iterative guesses at the stiffness k, and plotting the resulting estimate of the quasi-steady behaviour, the optimal value of k can be chosen which minimizes the hysteresis in the quasi-steady behaviour". By plotting the graph of $F_d\left(\hat{v}_1\right)$ for different values of $\hat{k}_{pre}$, an optimal value of $\hat{k}_{pre}$ can be identified. This process is illustrated in figure 2.5. Here, this process has been automated by noting that the hysteresis is minimised when $\hat{k}_{pre}$ reaches such a value that $F_d = 0$ when $\hat{v}_1 = 0$. To quickly reach an acceptable value of $\hat{k}_{pre}$, an iterative procedure with an initial estimate of $\hat{k}_{pre}$ is used. If the value of $\hat{k}_{pre}$ is larger than the optimal value of k_{pre} (the case in figure 2.5(b)), then the estimate of $\hat{k}_{pre}$ is reduced. If this value is too small (the case in figure 2.5(c)), then the estimate is increased. Usually, the final value is reached after about ten iterations. This automation is useful when it comes to identify the parameters for many experimental conditions, as is the case in the present study. Note that we use only the decelerating part of the signal (see figure 2.5(a)) to determine k_{pre} and the quasi-steady curve in order not to be disturbed by inertia effects [2].

[2] At high velocities and positive accelerations, force overshoots and secondary loops can occur. Note that the hysteretic curve progresses counter-clockwise with time.

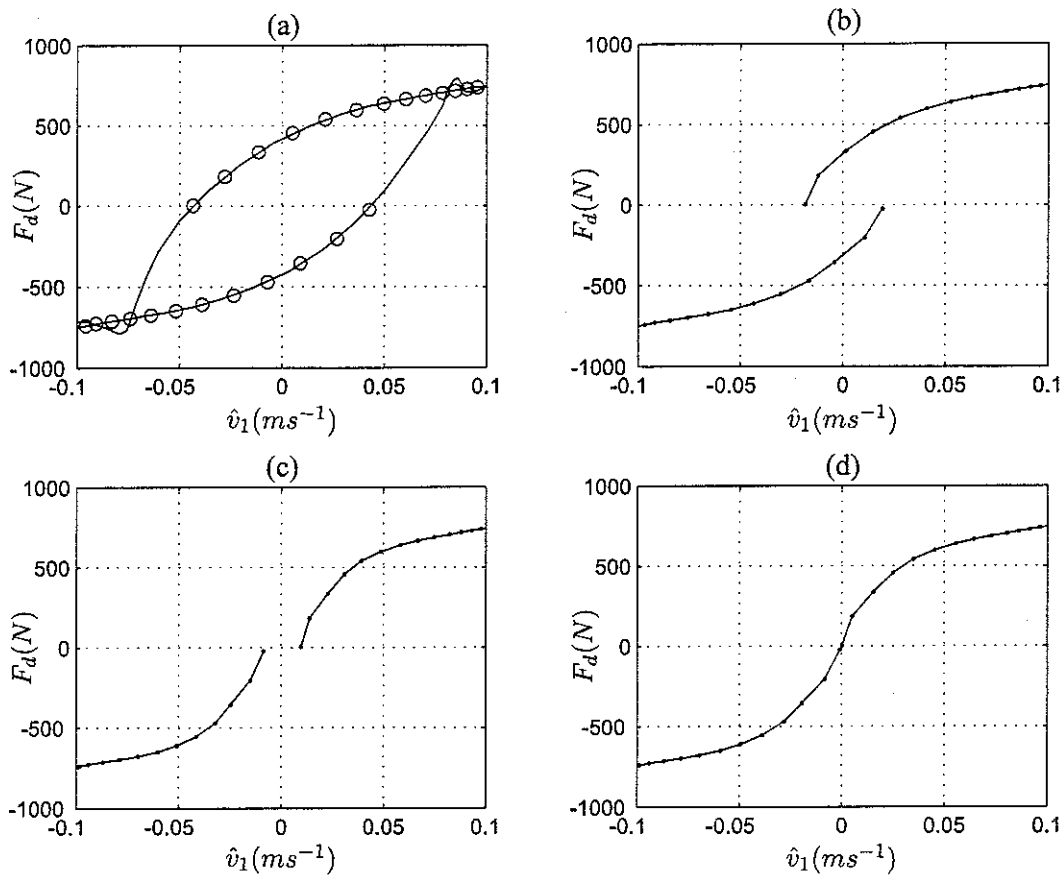

Figure 2.5: Iterative procedure of determination of k_{pre} after n iterations (1.5 mm, 15 Hz, 0.4 amp): (a)original signal (-) and decelerating part of the signal (o) (b) n=4, $\hat{k}_{pre} = 15.8e6Nm^{-1}$ (c) n=7, $\hat{k}_{pre} = 6.1e6Nm^{-1}$ (d)final iteration n=12, $k_{pre} = 7.5e6Nm^{-1}$: quasi-steady function.

2.2.2.2 *Identification of the quasi-steady function*

As seen in the previous section, an optimal value of k_{pre} results in a quasi-steady curve, as shown in figure 2.5(d). The second step is to identify a function that fits this $F_d - \hat{v}_1$ curve. In [14], a biviscous function was used. The biviscous function is a 3-parameter function, which is non-differentiable at the passage from preyield to postyield. Here, we use the hyperbolic tangent function. It has the advantage of offering a smoother transition between preyield and postyield while also using only 3 parameters. Our quasi-steady function is defined by

$$\chi(v_1) = F_y tanh(\alpha v_1) + c_{post} v_1 \tag{2.5}$$

where F_y is the yield force, α is a parameter with dimension equal to velocity^{-1} and c_{post} is the post-yield damping coefficient. The curve fitting is performed using a non-linear least-square method ("lsqcurvefit" in Matlab). Both biviscous and hyperbolic tangent functions fitted to the experimental quasi-steady curve are shown in figure 2.6. We see that the hyperbolic tangent function gives a better fit than the biviscous function, especially in the preyield-postyield transition. Note that the transition is smooth for small displacements. In our study the displacement amplitudes are smaller than most of the studies in the literature. F_y and c_{post} are similar to the parameters used in [14] and there is a clear relationship between the preyield damping coefficient C_{pre} defined in [14] and the parameters defined in equation 2.5, i.e.

$$\left(\frac{\partial \chi}{\partial v_1}\right)_{v_1=0} = C_{pre} = F_y \alpha + c_{post} \tag{2.6}$$

2.2.3 Simulation procedure

Once all the parameters of the model are identified, it is possible to calculate the damper force, given the displacement of the piston x_2. The equations 2.2 were implemented in Simulink, and solved numerically either using a Runge-Kutta 4 (in matlab the function "ode45") method or using a modified Rosenbrock formula of order 2 (in matlab the function "ode23s"). This latter method converges faster because it is suitable for stiff equations, which is the case in this study, especially when the preyield postyield transition is

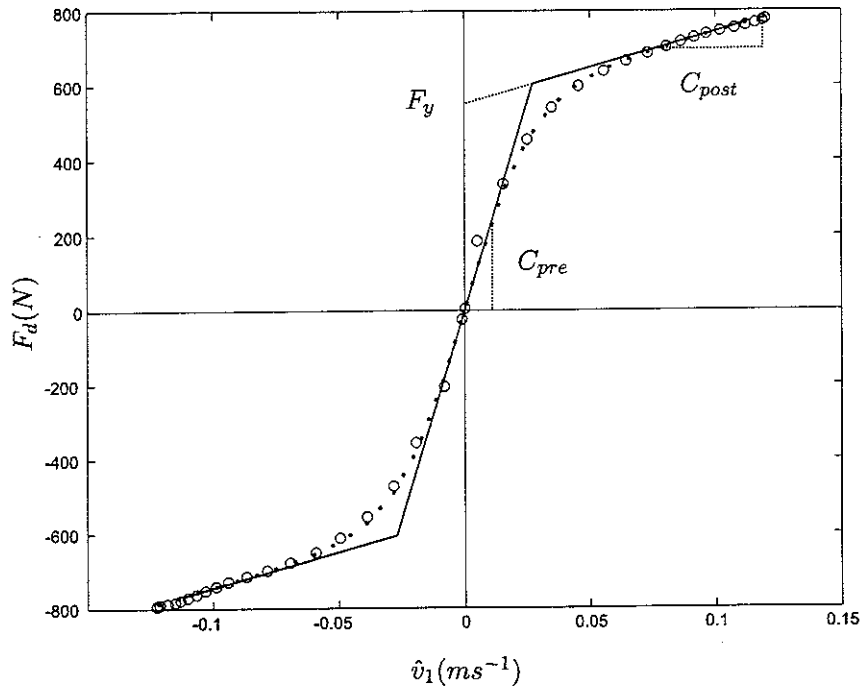

Figure 2.6: Quasi-steady damping curves (1.5 mm, 15 Hz, 0.4 amp): (o) experimental curve, (-)biviscous, (..)hyperbolic tangent. C_{pre} here is defined according to [14] and is different from c_{pre} in this study.

sharp.

To illustrate the quality of the procedure, the case of 1.5mm displacement amplitude, 15Hz, frequency, and 0.4 amp, current, is treated. The identified parameters are given in table 2.1.

k_{pre}	F_y	α	c_{post}
$7449.4kNm^{-1}$	$551.2N$	37.67	$1.93kNms^{-1}$

Table 2.1: Parameter values for the case of 1.5mm displacement amplitude, 15Hz, frequency, and 0.4 amp, current.

The presence of the mass m_1 in the model is essentially motivated by a practical reason: it makes the numerical scheme converge faster. Indeed, without any mass, the equations are very stiff. In [14] it is also claimed that this mass has a physical justification: it would represent fluid inertia terms that are at the significant when "force overshoots" might occur (see figure 2.5(a) at high velocities). Another possible explanation of these force overshoots could be the existence of the stiction phenomenon, occuring when the MR chains break. This phenomenon was observed in [7] in viscometric tests on MR fluids.

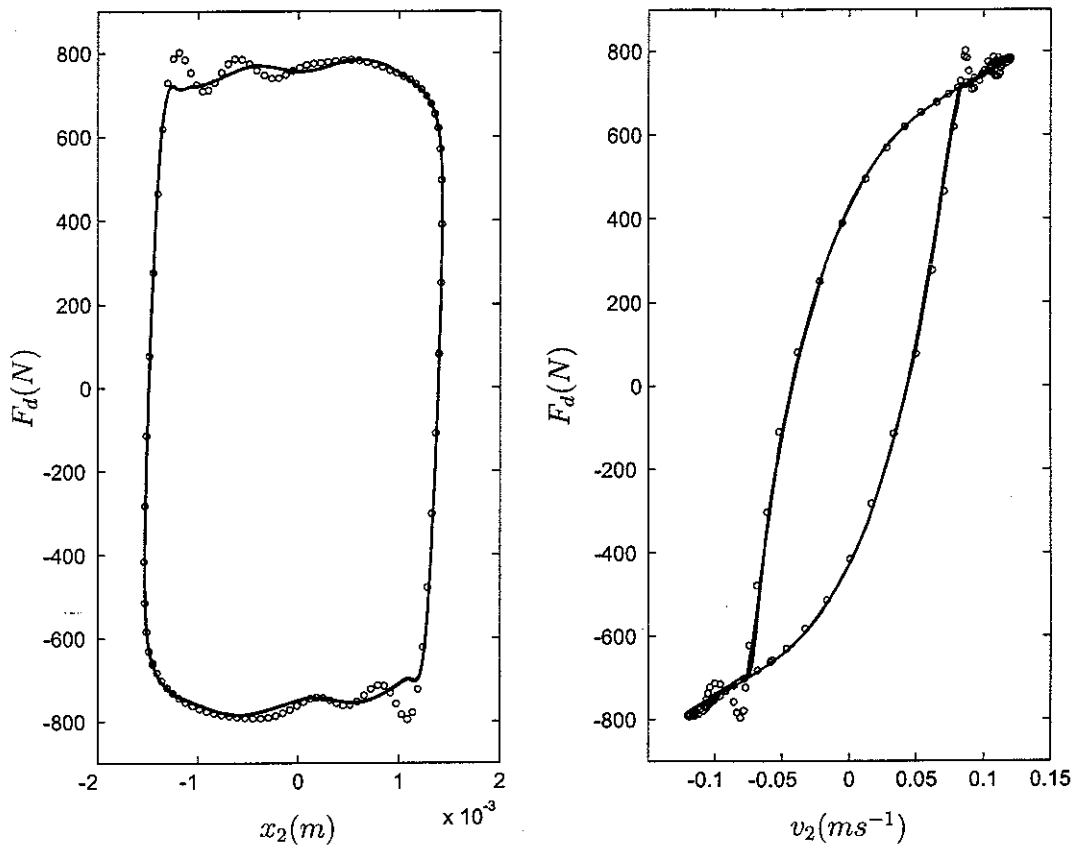

Figure 2.7: Experimental (o) and simulation curves (-) for (1.5 mm, 15 Hz, 0.4 amp) test: (a) displacement-Force diagram. (b) velocity-Force diagram.

Whatever the origin of force overshoots, we choose not to take these effects into account. An arbitrary mass of 1 kg was set to carry out simulations. The comparison between experimental and simulation curves are shown in figure 2.7. We can see the agreement between measurements and simulation is generally good.

2.3 Experimental study

The MR damper that is used in this study is a commercial device from the Lord Corporation and is the same apparatus as the one characterised in [14]. The model described and identified in the previous section works particularly well because the values of the parameters used in simulation are exactly the output values of the identification process[3]. However, in most of engineering problems, the disturbance source is non-sinusoidal and

[3] Moreover, the presented case has a sinusoidal excitation of good quality. In other cases treated in this section, harmonics of the excitation frequency appear due to inherent non-linearities of the excitation jack and perturb the identification procedure.

is not an explicit function of frequency and displacement amplitude, but of time. So it is necessary to find parameters that describe behaviour over the whole frequency range relevant for the application investigated for vibration control.

An analysis of the disturbance data of the launcher application has shown that the displacements amplitudes are typically in the order of a millimeter. Moreover, as the damper is aimed at controlling the resonance of a soft isolator mode, the required control bandwidth is up to 15 Hz. Above this frequency, the damper works primarily in its passive mode (no current). Finally, a preliminary experimental study of a simple on-off skyhook control has indicated that the maximum current is not likely to exceed 1 amp. As a consequence, it has been decided to carry out characterisation with the following sinusoidal excitations and the following current values:

- displacement amplitude: $x_2 = 1.5$ mm (peak).
- excitation frequencies: $f = 2$ to 15 Hz in steps of 1 Hz.
- current: i_c = [0 25 50 75 100 200 300 400 600 700 800 900] (mA).

A current-dependent model is built. For a fixed current, the identification procedure described in section 2.2.2 is performed for the entire frequency range: the values of the parameters for the whole frequency range are then taken to be the mean values of the discrete frequency cases.

2.3.1 Identification of stiffness

The identification of stiffness is carried out for each case of frequency and current. A database of $k_{pre}\,(f, i_c)$ and quasi-steady curves is obtained. For instance, figure 2.8 shows the damper force capacity. As the current increases, the force increases. For each current, a set a 15 quasi-steady curves and stiffness values (see figure 2.9) is obtained. It appears that k_{pre} is dependent on frequency and current (and probably on displacement as well). As underlined in [14], the stiffness dependency with current and frequency is the most critical part of the modelling work. In [14], a constant value of stiffness of 13MN/m is chosen. In this work, in order to have a frequency-dependent preyield stiffness, it has been chosen to replace the stiffness by a Kelvin-Voigt model, as shown in figure 2.4(a).

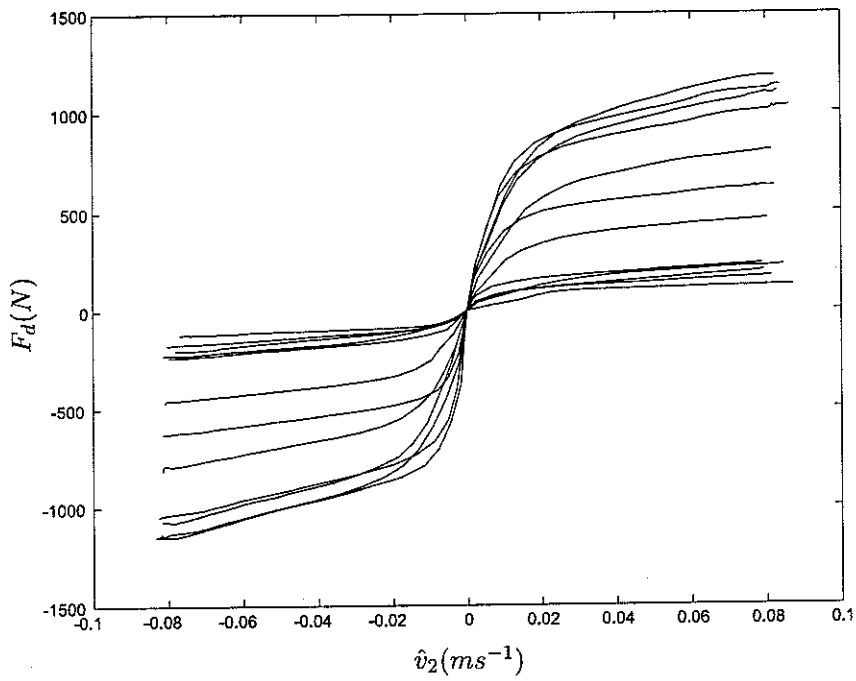

Figure 2.8: Damper effort range at 9 Hz.

Indeed k_{pre} is found to increase generally with frequency, which is the case of the complex stiffness modulus of a Kelvin-Voigt model which is given by

$$k^*_{pre} = k_{pre} + j\omega c_{pre} \tag{2.7}$$

A constant value of $c_{pre} = 10kNms^{-1}$ was finally chosen empirically (during the model validation process, see section 2.4). Moreover, to account for current-dependency of the stiffness, it has been chosen to define a law $k_{pre}\,(i_c)$ defined as

$$k_{pre} = a_{pr} + b_{pr}tanh\,(c_{pr}i_c) \tag{2.8}$$

This function exhibits an increase with current with saturation at high currents. This trend is observed in figure 2.9, despite the wide scatter values at low currents, which are unexplained (it might be some uncontrolled experimental conditions such as temperature increases during loading or the fact that excitation is not purely sinusoidal). The parameters are chosen so that the curve circumscribes the lower boundary of the values. This part of the identification process is quite empirical but gives quite reasonable results in the end (see section 2.4).

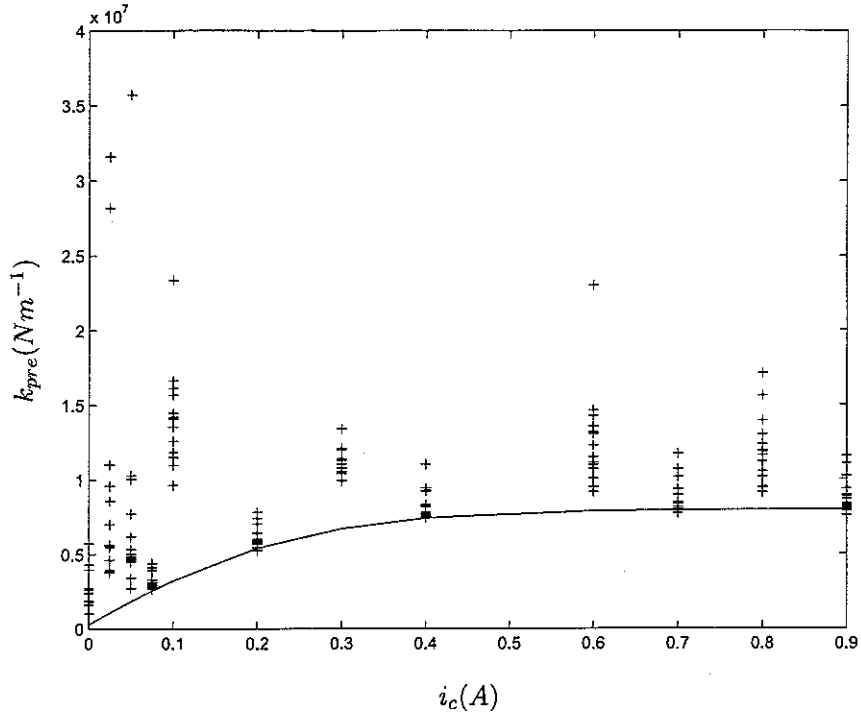

Figure 2.9: (+) Values of k_{pre} with for different currents and frequencies. (-) Proposed current-dependent law.

2.3.2 Identification of the quasi-steady-state model

2.3.2.1 Stiffness and quasi-steady curves

As discussed in section 2.2.2, and recalled below, the quasi-steady function involves three parameters F_y, α and c_{post}.

$$\chi(v_1) = F_y tanh(\alpha v_1) + c_{post} v_1 \tag{2.9}$$

Again, these parameters are found to be dependent on both current and frequency. The identification of preyield stiffness yields a set of 15 quasi-steady curves for each value of current (one curve per frequency). The results are shown in figure 2.10. The frequency dependence has a clear effect on α: the preyield slope decreases with frequency. This decrease seems quite physical since at high frequency, the flow velocity in the valve increases, then the passage time through the valve decreases, preventing the chains from completely forming (the chain deformation at low strain is the physical phenomenon that explains the existence of the preyield stiffness and viscosity). In the high frequency limit,

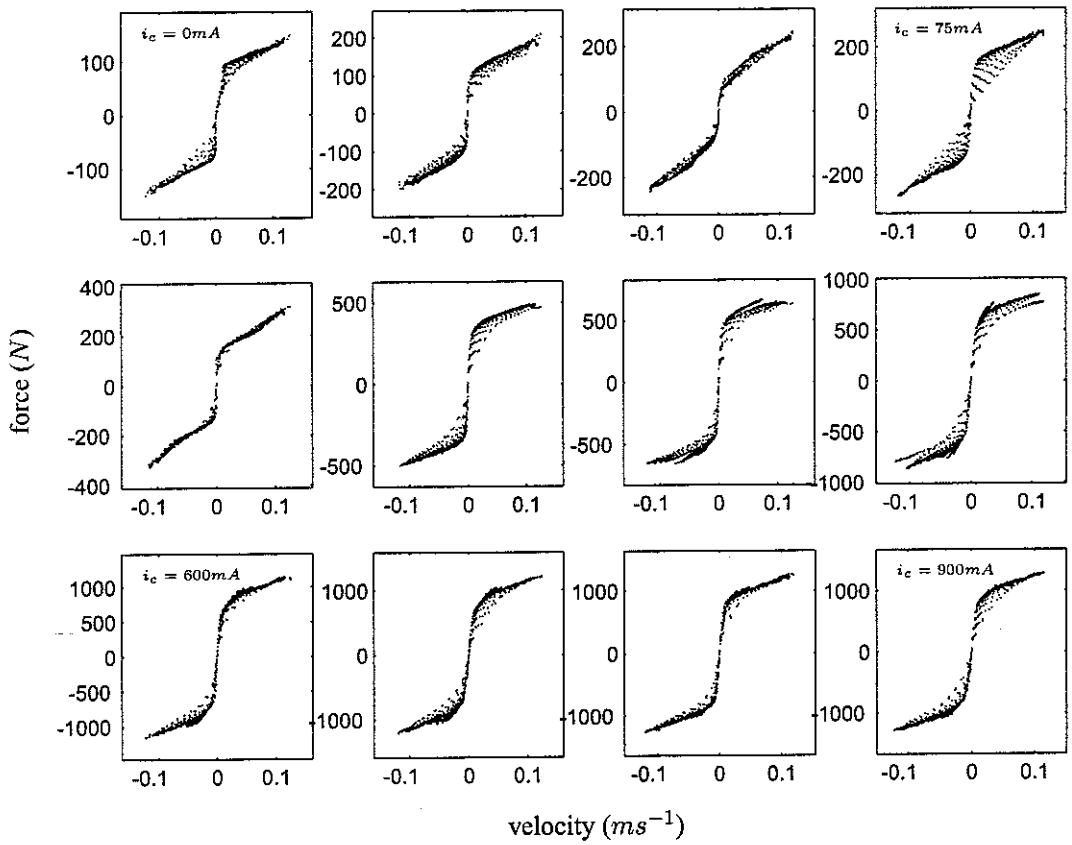

Figure 2.10: Quasi-steady curves (velocity-force diagrams). From left to right and top to bottom: increasing currents. From blue to red: increasing frequency.

the chains do not form at all and the fluid flows easily: the preyield slope, and therefore α, tends to 0. At the quasi-steady state limit, the passage time of the particles is infinite, and the chains are completely formed when the MR fluid passes through the valve. Thus the fluid is "choked" or "blocked" and does not easily flow: α becomes large.

From the results, at a constant current, it is interesting to note that there would appear to asymptotes at high values of force/velocity, which might be the same as the quasi-steady curve that is usually observed in studies, where displacement amplitudes are large and frequencies very low. We could define a unique curve that fits this asymptote and which would account for the different excitation frequencies. However, a slightly different, but similar approach has been adopted: a non-linear least-squares curve fitting of the whole velocity-force data, at each value of current, has been performed, for the function presented in equation 2.5. For a given current, the function is fitted on average, for all frequency cases. The result of fitting for a current of 0.9 amp is shown in figure 2.11.

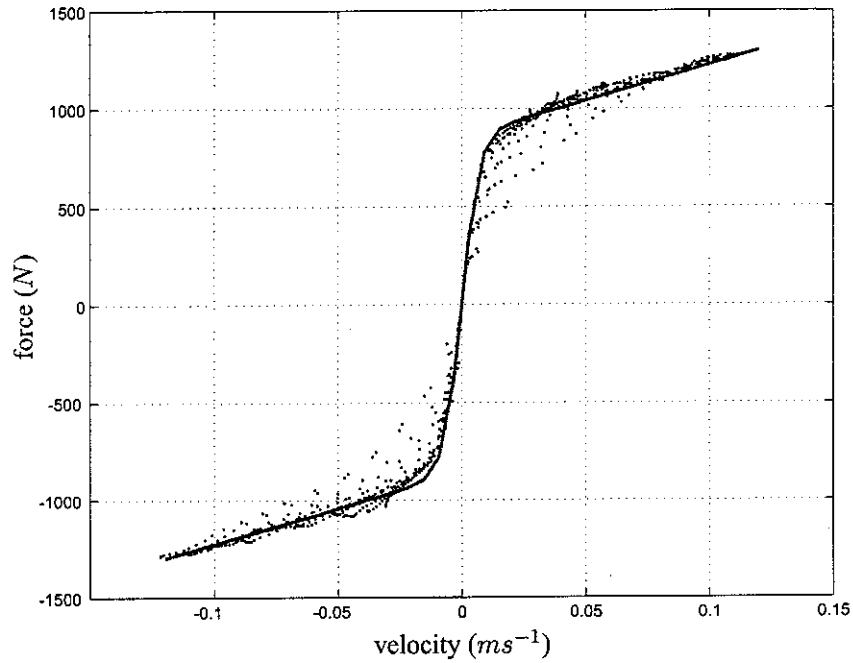

Figure 2.11: Quasi-steady curves at $i_c = 0.9$ amp. (.) experimental, (red lines) curve fitting.

2.3.2.2 *Dependence of the model parameters on current*

Finally, the parameters of the quasi-steady damping function are identified and their dependence on current is found. Similarly to [14] and to equation 2.8, a hyperbolic tangent function is used to model c_{post}, i.e.

$$c_{post} = a_{po} + b_{po} tanh\left(c_{po} i_c\right) \tag{2.10}$$

Again a non-linear least-squares fit is performed and the fit is shown in figure 2.12(b). With regard to F_y, according to experimental data shown in figure 2.12(a), it would appear that the rate of change of F_y with i_c is small for low currents, then increases, and finally gradually decreases at large values of i_c. This seems to be in accordance with some physical models of MR fluids (see [24]), where the yield stress is found to follow a power law of the magnetic field (power of 1.5) for small magnetic field, before a saturation occurs. To fit such a behaviour, a function using a linear combination of two exponential functions is used. The function is written as

$$F_y = a_y + b_y \left(1 + \frac{c_y}{d_y - c_y} e^{-i_c/c_y} + \frac{d_y}{c_y - d_y} e^{-i_c/d_y}\right) \tag{2.11}$$

k_{pre}			c_{pre}	m_1	F_y				α	c_{post}		
a_{pr}	b_{pr}	c_{pr}			a_y	b_y	c_y	d_y		a_{po}	b_{po}	c_{po}
3e5	7.7e6	3.95	1e4	1	65	814.5	0.06	0.36	143.8	686.3	8.57e3	0.60

Table 2.2: Values of the coefficients (in SI units) of the current laws.

and the least-squares fit to the data is also shown in figure 2.12(a).

With regard to α, a constant was found chosen, since the data show a erratic behaviour (see figure 2.12(c)). Finally, the model coefficients of equations 2.10 and 2.11 were fitted once again, using the mean value of α. Table 2.2 shows final values of the coefficients used to model the dependence on current.

As we can see, the fit is quite good for F_y but more debatable for c_{post} and α. However, as it will be seen in section 2.4, the quality of the model depends much more on the quality of fit of F_y than of c_{post} and α.

To summarize, we have a model of the MR damper that enables one to predict the damper force as a function of piston displacement and velocity (relative to the damper body displacement and velocity) and of the current in the damper coil. This model is used in chapter 3 for simulations of semi-active control. For realistic simulations, we first validate our identified model with the current-dependent parameters described in section 2.4 by comparing the model with experimental results. The set of equations used in the model is summarized below

$$\begin{cases} F_d = k_{pre}\left(i_c\right)\left(x_2 - x_1\right) + c_{pre}\left(\dot{x}_2 - \dot{x}_1\right) \\ m_1\ddot{x}_1 = k_{pre}\left(i_c\right)\left(x_2 - x_1\right) + c_{pre}\left(\dot{x}_2 - \dot{x}_1\right) - \chi\left(\dot{x}_1, i_c\right) \\ \chi\left(\dot{x}_1, i_c\right) = F_y\left(i_c\right) tanh\left(\alpha\dot{x}_1\right) + c_{post}\left(i_c\right)\dot{x}_1 \\ k_{pre}\left(i_c\right) = a_{pr} + b_{pr} tanh\left(c_{pr} i_c\right) \\ c_{pre} = constant \\ F_y\left(i_c\right) = a_y + b_y\left(1 + \frac{c_y}{d_y - c_y} e^{-i_c/c_y} + \frac{d_y}{c_y - d_y} e^{-i_c/d_y}\right) \\ \alpha = constant \\ c_{post}\left(i_c\right) = a_{po} + b_{po} tanh\left(c_{po} i_c\right) \end{cases} \tag{2.12}$$

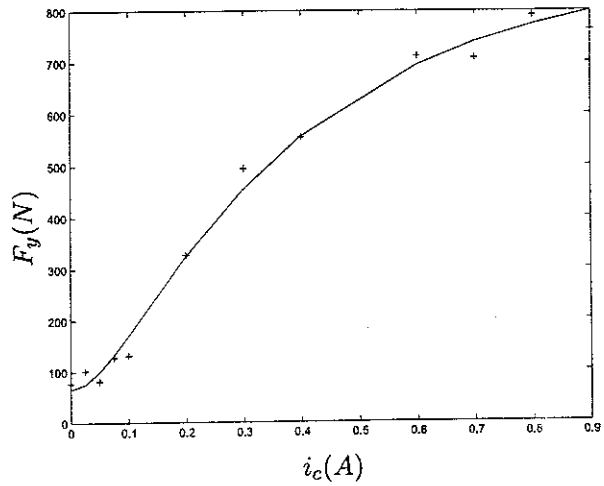

(a) Yield force

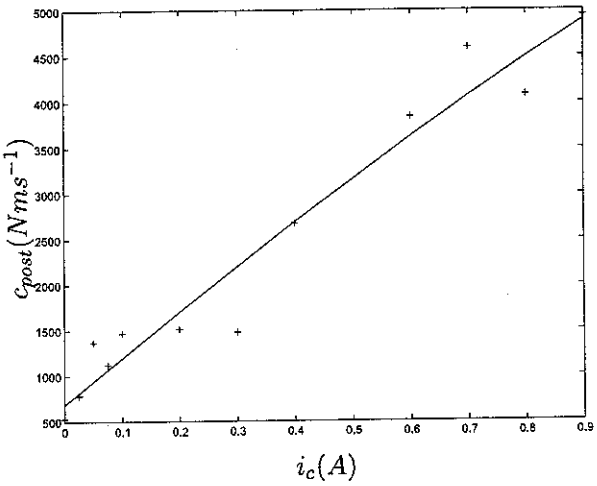

(b) Postyield damping coefficient

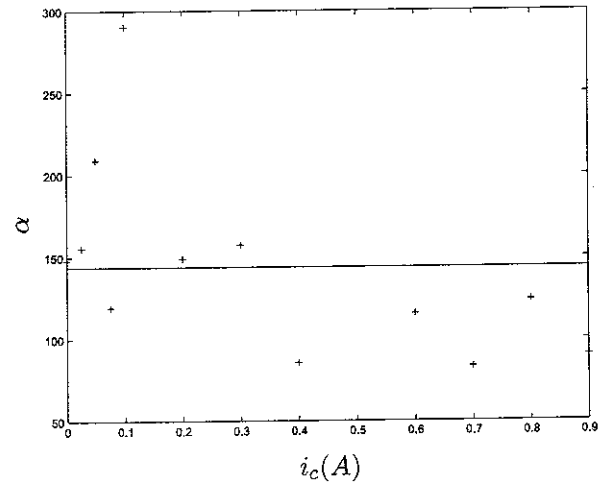

(c) α

Figure 2.12: Dependence of quasi-steady damping function parameters on the current.

2.4 Model validation and discussion

When the model was identified, the damper force was calculated according to the equations described in the previous section. A Matlab-Simulink model was developed based on these equations. In this section, results of simulations of the model are compared with experimental measurements.

2.4.1 Qualitative comparison of the simulation and the experimental results

To begin with, to illustrate the model, the velocity-force diagrams derived from the experiment and the model are compared. The question is whether the model faithfully reproduces the measurements over a wide range of frequencies and currents (these ranges are the same as in section 2.3). Five criteria enable one to evaluate the quality of the model:

- the yield force level;
- the width of hysteresis loop;
- the preyield slope;
- the postyield slope;
- the smoothness of preyield/postyield transition.

Obviously the quality of the model depends on the errors and approximation in the different fitting procedures shown in figures 2.9 and 2.12 and on the ability of the quasi-steady function to capture as a whole the behaviour of the curves for different frequency cases (see figure 2.11). In figure 2.12, the fit seems reasonable for F_y, but less good c_{post} and α. However, it will be seen that the quality of the model depends essentially on the predictability of F_y. As shown in figure 2.13, on the whole a good correlation between the model and the measurements is observed. We notice however that the results appear better for the larger currents, which is only to be expected since the parameters increase with current, so relative errors decrease. In figure 2.13, the series of velocity-force diagrams for frequencies from 2 to 15 Hz, for two cases of current are shown: results are shwon for the worst case (2.13(a), $i_c = 0.05$ amp) and the best case (2.13(b), $i_c = 0.9$ amp) of all

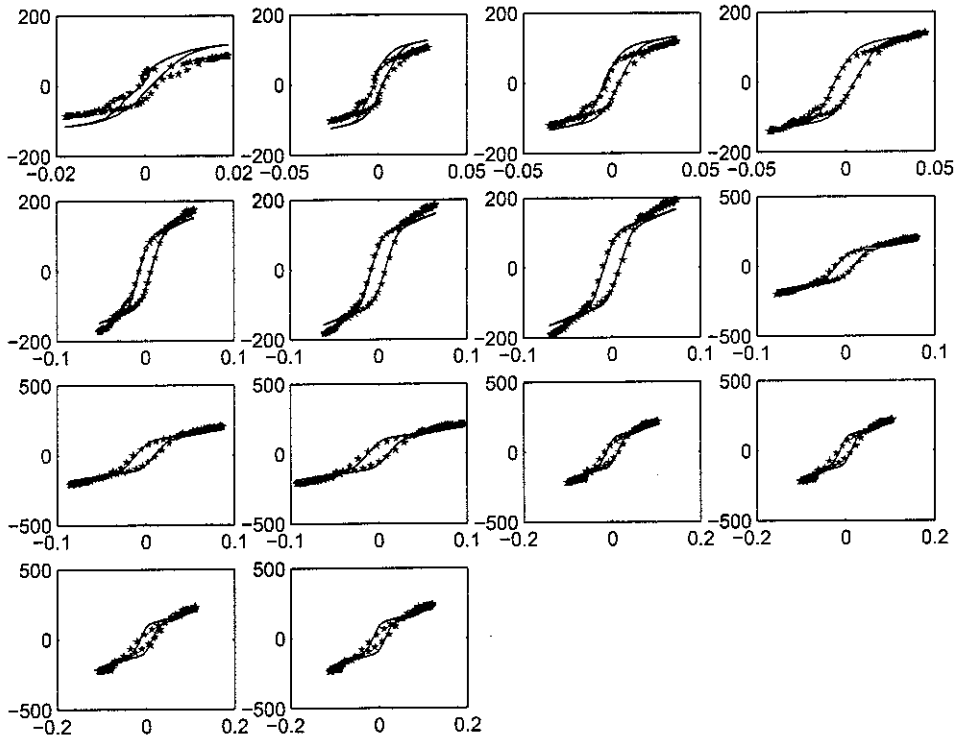

(a) for $i_c = 0.05$ amp

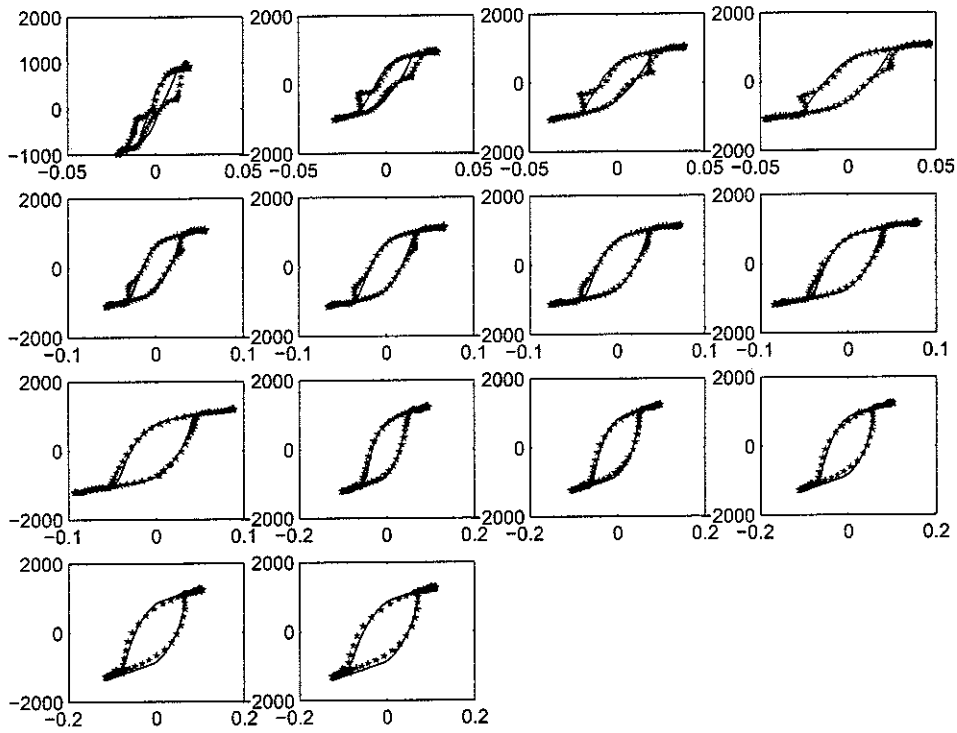

(b) for $i_c = 0.9$ amp

Figure 2.13: Comparison between ($\star$) experimental and (-) predicted velocity-force diagrams. From left to right and top to bottom: increasing frequency from 2 to 15 Hz by step of 1 Hz.

the cases of current. In figure 2.13(a), we can observe some notable differences between the model and the measurements:

- for the 5 first frequencies, F_y is over-estimated;
- for the 8 first frequencies, c_{post} is under-estimated;
- for the 5 last frequencies, the preyield slope is over-estimated.

This last phenomenon is due to the fact that our preyield mechanical analog is fluid-like (with 3 fluid material parameters) and not solid-like (see the comments in section 2.1). The same phenomenon is observed in [14].

In figure 2.13(a), a good correlation between model and experiment is observed, especially for the highest frequencies. For low frequencies, some secondary effects on the accelerating part of the curve are not captured by the model. It is partly because the identification of the quasi-steady function is based on the decelerating part (cf figure 2.5). These effects are unexplained and could be due to the bad quality of the excitation used in the experiment (the hydraulic jack gave distorted sines at low frequency).

2.4.2 Quantitative comparison of the simulation and the experimental results

In order to quantify the differences between the model simulations and the experimental results, the relative error is defined as

$$\delta = 100 \frac{\int_0^{t_e} (F_p - F_m)^2 \, dt}{\int_0^{t_{end}} F_m^2 dt} \tag{2.13}$$

where F_p and F_m are respectively the predicted and the measured forces, and t_e is the duration of experimental data acquisition (which generally corresponds to about ten periods of the excitation signal). This indicates approximately the percentage relative error over the whole measurement period.

This error is plotted against the current (figure 2.14(a)) and the frequency (figure 2.14(b)). Generally, the error does not exceed 10 %, except for two cases at 2 Hz. Figure 2.14(b) shows that the error decreases with frequency. This is in accordance with the observations of figures 2.13(a) and 2.13(b) (error in the accelerating part of the signal). For high

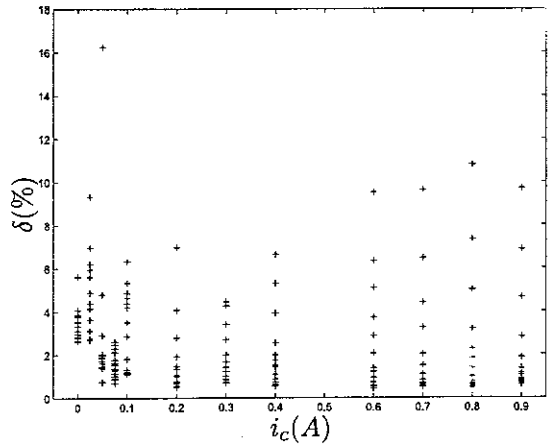

(a) As a function of current, for different frequencies

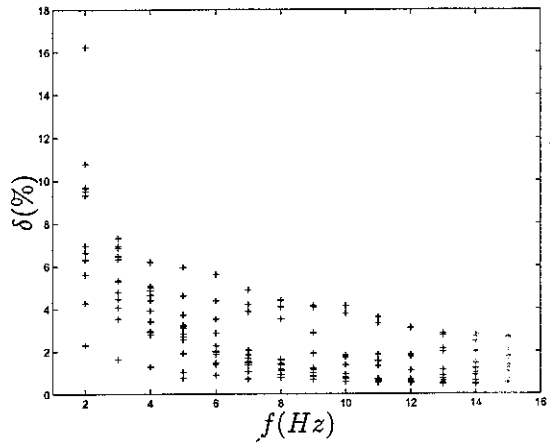

(b) As a function of frequency, for different currents

Figure 2.14: Relative error between predicted and measured damper force.

frequencies, we see in figure 2.14(a) that the error is generally below 4 % and tends to decrease with current. Again, this is in accordance with figure 2.13 where the results are clearly better for 0.9 amp than for 0.05 amp.

2.5 Summary

MR dampers have a strongly non-linear behaviour. Their modeling is necessary for realistic simulations of semi-active control, but this is a hard task. There does not exist predictive modelling approaches based on constitutive behaviour laws of the MR fluid (elasto-visco-plastic material), and on the fluid mechanics equations. The current modelling approaches are therefore phenomenological, based on measurements of the characteristics of the damper. The material non-linearities are of three types:

- for a given magnetic field, above small strain rates and above a yield stress, the fluid flows as a visco-plastic material (post-yield region). The most simple model to capture this effect is the Bingham model.

- for a given magnetic field, for small strains, the fluid has an elastic behaviour (pre-yield region), because of an elastic deformation of the chains of particles. This provokes an hysteretic behaviour of the damper. Moreover, the fluid compressibility (of the carrier liquid) participates to the hysteresis by inducing elasticity of the damper under small displacement amplitudes.

- the constitutive parameters depends non-linearly on the magnetic field.

As a consequence, the adopted damper model is a non-linear viscous element with three parameters (using the hyperbolic tangent function), in series with an elastic element (Kelvin model, two parameters). Moreover, a mass element is used to decrease the numerical stiffness of the model. Three of the six parameters depend on the current.

The identification procedure of the parameters, updated on the measurements, is presented and the model is finally compared to the experimental measurements for sinusoidal motions at various frequencies and currents. The characterization has not taken into account the influence of the displacement amplitude, which plays a fondamental role on the behaviour of MR dampers. The characterization performed here is based on the assumption that the displacement amplitudes are not small, i.e. are at least higher than 0.5 mm. There is a good correlation (less than 10% error) in the ranges of currents and frequencies that concern the application of control. The discrepancies between the model and the experiment are mainly due to an overshoot of force when the piston accelerates (stiction phenomenon) that is not captured by the model. More parameters could be used to account for this, but the chosen model seems to be a good compromise between simplicity and accuracy.

CHAPTER 3 SINGLE AXIS SEMI-ACTIVE ISOLATION

In chapter 1, a brief description of single dof semi-active isolation using the well-known clipped continuous skyhook damper control strategy was described. In this chapter, a more detailed discussion is addressed, focusing on two main aspects: the mechanical design of the isolation mount and the semi-active controller design. Prior to an experimental investigation that is reported in the next chapter, this study presents some simulations. In section 3.1, the simulation procedure and the performance criteria used to evaluate various control implementations are presented. In section 3.3, some considerations on the mechanical design of the isolation mount are reported, focusing on the hardware limitations due the MR damper properties. A study of optimisation is done to minimise the detrimental effects of these properties on the isolation performance. Finally, the semi-active control design is studied, prior to experimental verification. Because skyhook damper control, though simple, is known to be very efficient in the single dof isolation system, we focus here on various implementations of this control: explicit clipped continuous skyhook, explicit clipped on-off skyhook, clipped on-off force feedback control with a threshold force, and clipped continuous force feedback control. These two last control strategies, able to emulate any active controller, are of particular interest in more complex mechanical systems, where skyhook control might not be efficient. These implementations are presented in section 3.2 and their performance are evaluated in section 3.4.

3.1 Simulation methodology

In this section, we present the simulation methodology as follows:

- the simulation tool: Simulink for simulation in the time domain,
- the simulated system: the semi-active device models used in the isolation system[1],
- the inputs of the system: the excitation signals,

[1] the controllers are presented in the next section

- the outputs of the simulation: the performance criteria.

3.1.1 Simulations in the time domain

Simulation in the time domain is a valuable tool to design a semi-active controller. Indeed, as a semi-active isolation system is non-linear, it is not possible to use classical filter design theory in the frequency domain (analysis of stability using root loci, Nyquist criteria and so on). A way to proceed to control design is to test empirically different parameters of control until obtaining satisfactory performance of the isolation system. As a consequence, simulation enables one to save much time compared to an experimental approach. Once a controller is believed to be satisfactory, it may be tested experimentally.

However, it is important to note that, as semi-active control is an emulation of active control (it tries to replicate a prescribed active force during the dissipative phases of control), the theory of active control and all the tools of classical feedback approach or the modern control techniques can be used during the design of the active controller to be emulated. Once a satisfactory or an optimal active controller has been developed, it is assumed that it will remain satisfactory or optimal in its semi-active version. This assumption is optimistic and probably not true, but necessary. In this report, simulation is performed using Matlab-Simulink. The equations of the mechanical system and the controller are written in a block diagram form.

3.1.1.1 The problem of time integration

The explicit skyhook controllers described in section 1.1.3 and 3.2.2 require measurement of velocities, and it may be desired to know the displacements as well[2]. However, a pure integrator ($\frac{1}{s}$) has an infinite gain at 0 Hz, which can present difficulties in simulations. As a consequence, it is necessary to use a high-pass filter. One possible transfer function of the modified integrator is

$$H_{pseuint} = \frac{s}{s^2 + 2\xi_{int}\omega_{int}s + \omega_{int}^2} \tag{3.1}$$

[2]for instance, to analyse the displacement transmissibilities

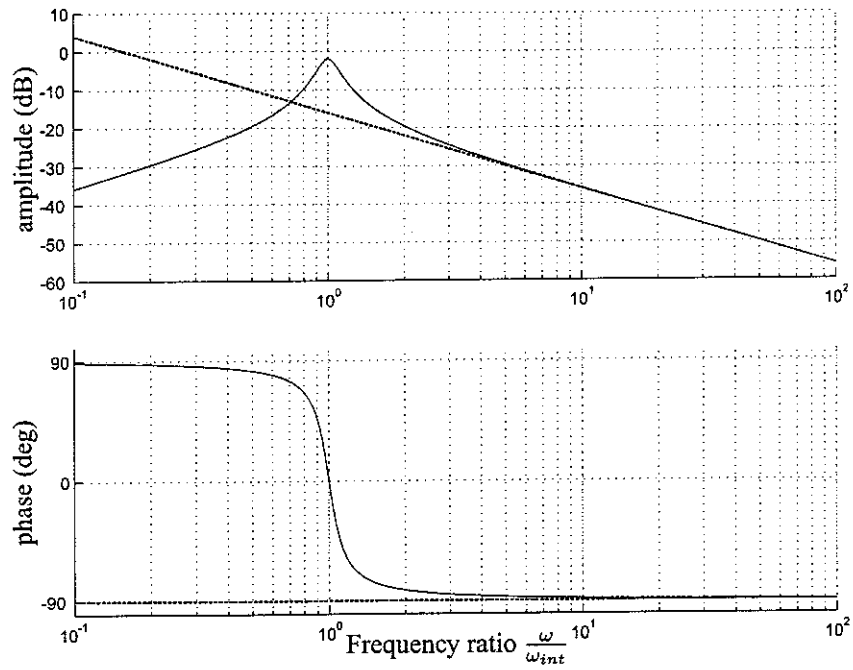

Figure 3.1: Magnitude and phase of the pure integrator (dashed) and of the pseudo-integrator(line).

where ω_{int} is chosen here to be $\omega_{exc}/10$, ω_{exc} being the excitation frequency for tonal disturbances, or the tenth of the lowest frequency contained in the spectrum of the excitation signal for broadband disturbances. ξ_{int} is chosen in most cases to be 0.1 in order not to seriously affect either the magnitude or the phase of the signals, as shown in figure 3.1. However, in some cases (it will be precised which ones), ξ_{int} may be chosen to be 0.707 in order damp more rapidly the transient response due to the modified integrator.

3.1.2 The semi-active damper models

The semi-active device model used in simulations is either the actual MR Damper (MRD) model described in chapter 2 or the model of an idealised controllable damper with variable damping coefficient illustrated in figure 3.2. Compared to the MR damper model, the ideal damper model is useful mainly for two reasons:

- the simulations using the MRD model are computationally expensive, because of the complexity of the model. Simulations with the ideal damper model are faster, which is an important criterion in a preliminary phase of research.

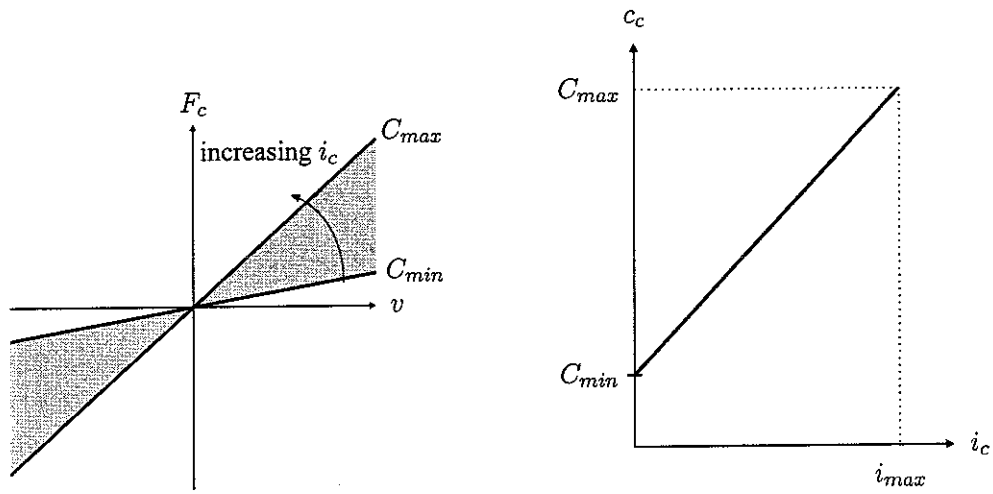

(a) Damping behaviour

(b) Current law of the controllable damping coefficient

Figure 3.2: Controllable damper with variable damping coefficient.

- the ideal damper model is invertible and causal, so it is possible to calculate the appropriate current to produce a desired force. This property is necessary to implement the explicit clipped continuous skyhook controller, which is used as a reference controller to evaluate an upper bound of semi-active skyhook control performance with an MRD. This is done in sections 3.3 and 3.4.2.

However, the use of the MRD model is necessary in the second phase for the preparation of the experimental study (control design), which is described mainly in section 3.4.

3.1.3 Excitation cases

3.1.3.1 About launcher excitations

According to the objectives of isolation during launch, there are three major sources of disturbance that have to be considered. These cases are visible in figure 3.3:

- the **lift-off** in the first ten seconds. This excitation is broadband and some launcher modes are excited, such as around: 5, 8, 11, 15 and 20 Hz;
- the **maximum pressure oscillation**. This phenomenon occurs at around 120 s. We can see that at 20 Hz, at this particular instant, the level is higher due a coupling between the longitudinal modes of the boosters and the acoustic modes due to the

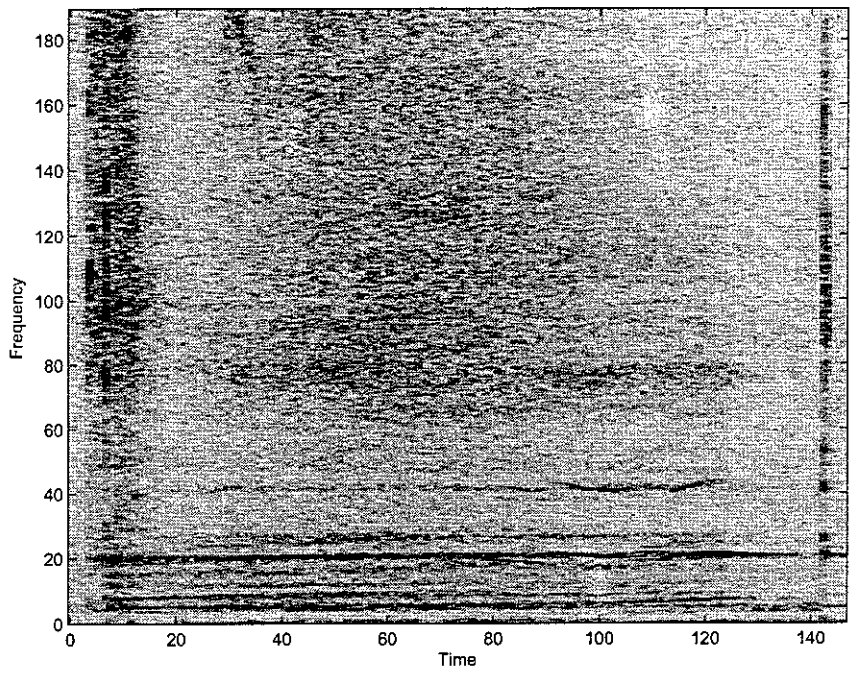

Figure 3.3: Spectrogram of one of the lateral acceleration (along y) at the payload base. (Flight measured data).

combustion inside the boosters. Note that this coupling occurs in a short time because the longitudinal modes of the boosters[3] evolve[4] during time due to the loss of mass[5] as well as the evolution of the acoustic modes[6]. This type of excitation is nearly periodic with a main contribution at 20 Hz;

- the **boosters separation** at 142 s. At this moment, due to a very short pyrotechnic combustion of the joints of the boosters on the central body of the launcher, a shock type excitation occurs. This disturbance is transient and may strongly excite the various modes of the launcher.

In the exploratory phase of the single axis isolation system, we do not deal directly with the excitations occuring during launch. But they can inspire different idealised excitations that a semi-active isolation system should deal with. These cases are described above.

[3]they are attached to the central body of the launcher via some soft viscoelastic layers.
[4]they increase, as can be seen on the spectrogram.
[5]ejection of the combustible
[6]they are linked to the volume of the cavity, which increases as combustion occurs.

3.1.3.2 *Sinusoidal excitation*

Sinusoidal excitations are not realistic compared to the launch environment, but this is a first step in evaluating the performance of a semi-active isolation system. Sinusoidal excitations are, as we will see, quite easy to deal with because the different semi-active controllers generally have the ability to bring some damping or not, depending on whether the frequency of excitation is around or above the isolator mode. The frequency of the sine excitation is in the 1-100 Hz frequency range.

3.1.3.3 *Periodic excitation with multiple harmonics*

Though being deterministic, this type of excitation is closer to launch environment than sinusoidal excitation because of the multiple modes of the launcher that filter the primary excitations (example: white-noise disturbance due to the engines). The maximum pressure oscillation case is typically of that type. This case of excitation is broadband and, for this reason, can be more difficult to deal with. Indeed it is already intuitive to think that, if the harmonics are located both below and above the cut-off frequency of the passive isolator at 0 dB[7], then it is desirable to have some significant damping for low frequencies, whereas it is better to have low or zero damping for higher frequencies. These contradictory conditions have to be studied.

However, we can notice on figure 3.3 that there is a low level of energy below 5 Hz. As a consequence, a choice of isolator frequency at 2 or 3 Hz, as claimed in sections and 5, should be a sufficient condition to avoid such problems, since then, all the harmonics would be above the cut-off frequency at 0 dB. Nevertheless, this is not guaranteed in so far as the modes of isolation system could be excited by the primary source of disturbances which are broadband. Simulation of the coupled system {launcher + isolation system} should be carried out to have a whole response. We will limit this excitation case as a two harmonics problem. Then, two cases will be studied depending on whether the frequencies of the two harmonics are located on both sides of the cut-off frequency at 0 dB or both frequencies are above this frequency.

[7] frequency from which the amplitude of payload acceleration is lower than the amplitude of base acceleration, whatever the damping ratio. This frequency is equal to $\sqrt{2}$ times the resonance frequency.

3.1.3.4 *Random excitation with a wide frequency spectrum*

As seen in figure 3.3, some random excitations occur during the flight. These are coloured-noise excitation because the nearly white noise primary disturbance is filtered by the structural modes of the launcher. However in this study, we will test the different control algorithms with a white noise process, covering a frequency range from nearly 0 Hz to 15 or 50 Hz.

3.1.3.5 *Shock excitation*

This is not considered in this report. But we keep in mind the simple, but probably efficient, idea of clipping the current from off to on at the exact instant the shock begins in order to damp faster the transient reponse of the mode of isolation.

3.1.4 Criteria of performance of a semi-active isolation system

3.1.4.1 *Tonal excitations*

Semi-active isolation is by definition non-linear and it is not possible to apply linear theory of Fourier or Laplace transforms. So we define here, for sinuoidal motions, other criteria of performance than frequency response functions such as transmissibility. A base sinusoidal motion $\ddot{x}_b(t)$ is applied and the payload response in steady state [8] $\ddot{x}_p(t)$ is found. Then to characterize the performance of the semi-active isolation system, different possible criteria of transmissibility can be tested to make an analogy with the transmissibility of linear isolators. Some criteria are

$$\begin{cases} H_{sa1} = \frac{max(\ddot{x}_p)}{max(\ddot{x}_b)} \\ H_{sa2} = \frac{RMS(\ddot{x}_p)}{RMS(\ddot{x}_b)} \\ H_{sa3} = \frac{max(x_p)}{max(x_b)} \\ H_{sa4} = \frac{RMS(x_p)}{RMS(x_b)} \end{cases} \tag{3.2}$$

Acceleration transmissibility is an important performance criterion because acceleration of the payload might be detrimental to the structure. On the other hand, displacement

[8] of course, time computing of motion equations induce a transient response which is not relevant for this performance study. So, steady state has to be waited for.

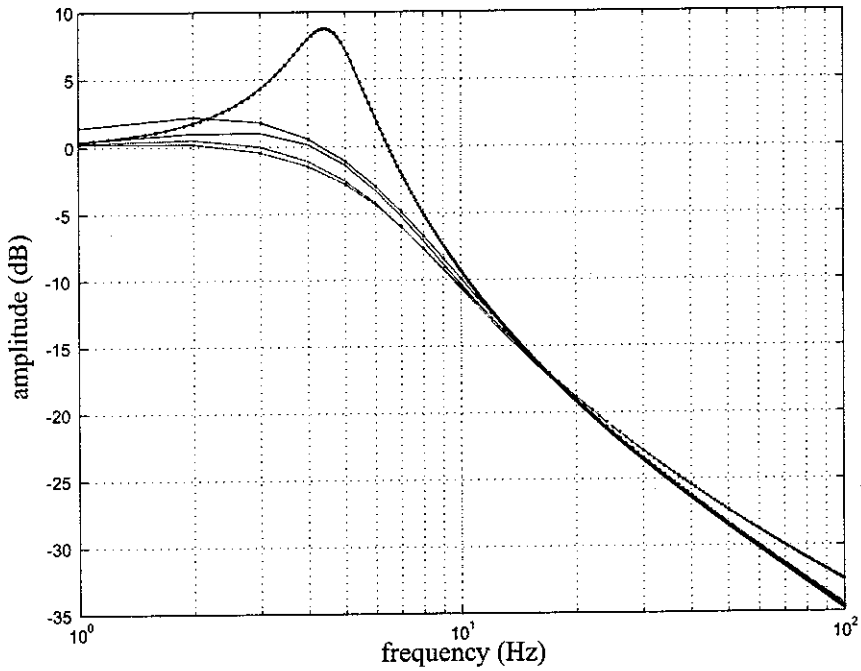

Figure 3.4: Magnitude of various transmissibilies for tonal disturbances (clipped continuous skyhook controller). In red: displacement transmissibilities. In blue: acceleration transmissibilities. (.-) based on maximum values. (-) based on RMS values. In black: passive isolator at zero current.

transmissibility is important as well since large displacements of the payload might cause the payload to impact against the fairing of the launcher. Indeed, the space between the payload corners and the fairing, which is called the rattle space, is limited. Because semi-active isolation is non-linear, acceleration and displacement transmissibilities are not the same. Indeed, semi-active control strategies are based on clipping the current in a short time, causing the damper force and so the acceleration to have some sudden changes (see the time sequence in figure 3.5). For this reason, the derivative of the acceleration, which is called jerk, may have large amplitudes[9]. On the other hand, there are no sudden changes in the displacement. As we can see in figure 3.4, there is a difference of a few dB between acceleration and displacement transmissibilities, especially at low frequency where the semi-active controller has a significant action. As regards the RMS and the maximum amplitude transmissibilities of displacement, they are very close and the criteria are nearly equivalent. From these observations, it appears that H_{sa1} is the most stringent criterion and it is the one which is the most used in this chapter.

[9]The effect of jerk has not been taken into account in this study. But we should keep in mind that jerk appears in semi-active control and might be detrimental for a structure

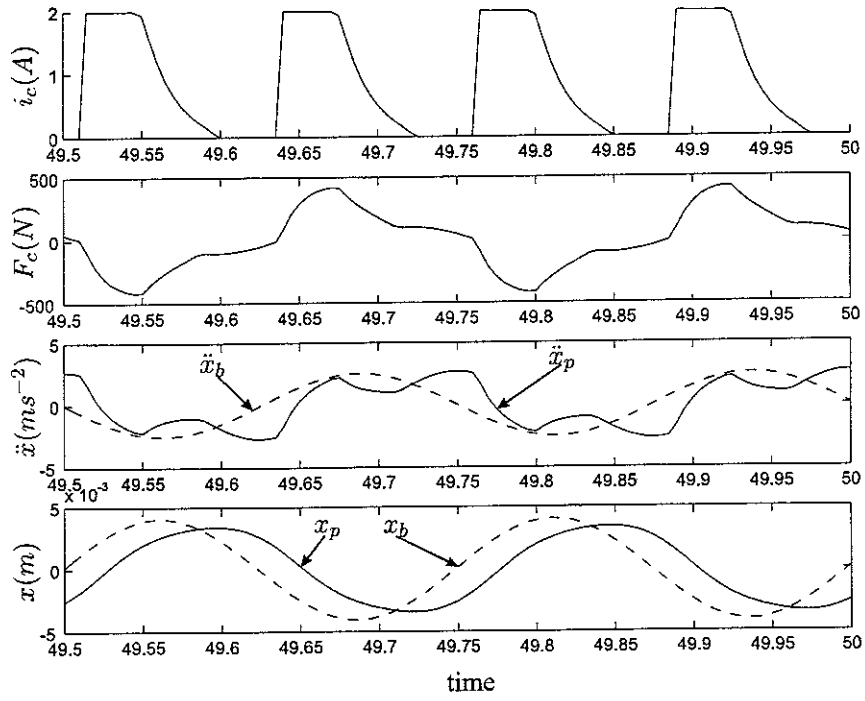

Figure 3.5: Time sequence of a simulation of a continuous skyhook controller for a sinusoidal excitation at 4 Hz.

3.1.4.2 Broadband excitations

For broadband excitations, the isolation performance can be analysed in term of either auto-power spectrum $S_x = S_{xx}$, computed from the Fourier transform of the signal x ($x = \ddot{x}_b$, in the sdof case), or transmissibility $H_{xy} = S_{yx}/S_{xx}$ (S_{yx} being the cross-power spectrum of the signals x and y, $y = \ddot{x}_p$, in the sdof case), or RMS amplitude, computed from the time signal or the frequency spectrum.

3.2 Semi-active control implementations

3.2.1 Review of semi-active control strategies

Semi-Active (SA) control has been the subject of considerable research activity, but to date, there is no clear consensus on its use. The main goal of Semi-Active Vibration Isolation (SAVI) is to provide high damping level at low frequency to reduce the resonant response, while bringing the least possible damping level at higher frequencies, in order to take advantage of the natural high frequency roll-off of the passive system. As it is

introduced in chapter 1, the Skyhook Damper Control (SDC) was found to be both simple and effective by Karnopp et al. [25]. Its extension to SAVI is termed clipped-continuous SDC [25]. The idea of the SA SDC is to emulate the active SDC only during the dissipative phases of control, because of the passivity constraint of the controllable damper[10]. Furthermore, the principle of emulation can be extended to any active control law[11]. In the literature, various optimal and robust control laws have been implemented in an SA formulation, such as SDC[12], LQG [28], [29], H_∞ [30], frequency shaping [31] and sliding mode control [32].

The real challenge in SAVI control design is how to track the prescribed force, due to the non-linearity and causality of the damper behaviour. For these reasons, it is difficult or impossible to accurately predict the required current to obtain the prescribed force. Therefore, various tracking strategies have been devised. The most simple methods are on-off or bang-bang methods, where the damping level is switched between various states. In its most simple implementation, the clipped on-off strategy has a bi-state form [33]. In section 3.4.1, we show with numerical simulations that this on-off control has intrisic limitations and presents poor performance enhancement compared to Passive Vibration Isolation (PVI). A more evolved implementation of on-off control is a n-state form, with resort to fuzzy logic [34] or neural networks [35], for instance. Clipped-continuous strategies can be used to enhance the prescribed force tracking strategy. To cope with the non-linearity of the damper behaviour, some researches have focused on an approximate linear relationship between the applied voltage and the maximum damper force [28], some others on the inversion of the damper model [30], others still on its linearization [31], [36]. Here, a tracking strategy using a continuous force feedback loop, inspired from [8] and [37], is adopted for experimental inmplementation. This control strategy is explained in section 3.2.3. Its control performance for tonal disturbances is evaluated numerically in section 3.4.2, and finally, its control performance for broadband excitation is evaluated experimentally and the results are presented in chapter 4.

It is to be noted that nothing guarantees that the performance of a clipped version of an

[10] the passivity constraint means that the damper is only able to dissipate energy

[11] Note however that the SA performance is a priori more effective if the active control law is mainly dissipative. Hence the idea is to favour active damping rather than active softening control strategies, for instance.

[12] SDC is proved to be optimal for the sdof system [26], for a white-noise base velocity. This proof is based on [27].

optimal control law will be optimal. This question is still an open issue. Some works have developed the formulation of a non-linear control problem, with a Lyapunov function to find optimal non-linear controls [38]. In particular, using the Maximum Principle of Pontryagin, an optimal SA control, which outperforms clipped-continuous SDC according to a comfort objective, was found to be a bang-bang control based on payload acceleration feedback [39].

Whatever the degree of sophistication of SA control, it should be kept in mind that the main objective of SAVI is to supply high damping around the suspension natural frequency, while bringing the least possible damping level at higher frequencies. As it has been shown in section 3.3, this goal is fully achieved for narrowband isolation with the actual devices available on the market, despite their response time. As it has been presented in section 3.3.5, the performance for tonal disturbances is very satisfactory if we proceed to an optimisation of the mechanical and control parameters of the mount. In particular, it appeared that the range of available damper force is a very important criterion. In this respect, the minimum damping force (under zero field) has to be small compared to the typical levels of prescribed force[13].

For broadband isolation (spectrum distributed both below and above $f_n\sqrt{2}$, f_n being the natural suspension frequency), this goal is harder to achieve because the damper force has a wider spectrum than the prescribed force [41]. Theoretically, SAVI performance is still much better than PVI performance [25], even if the damping level tries to switch very fast. However, it is known that the MRD response time (in the order of 25 ms) is quite large and depends on several operational factors [42]. The response time consequently deteriorates the attenuation performance, as it is shown in section 3.4.2. There are few published works on the effect of time delay on SA broadband isolation, which is nonetheless a very important limiting factor for practical applications. We can mention however on this subject the work published in [43]. Moreover, some work focuses on control strategies that take into account the damper time delay, but the spectrum of disturbance is generally not very large, [44] or even tonal, [45], [39].

This section presents a few semi-active control implementations, based on the SDC. In the next section, a study of optimisation of mechanical and control parameters for tonal disturbances is presented. Finally, this chapter ends with numerical evaluations of the

[13] Similar recommendation on the minimum damping ratio is also drawn in [40]

isolation performance of the considered control strategies, for various disturbance cases. First, it is shown that clipped on-off strategies are limited in performance, even for tonal disturbances. Then, the numerical implementation of an explicit version of the clipped continuous SDC using the idealised controllable damper is performed to assess an upper bound of performance for broadband isolation using a MRD. In particular, it is shown that the time delays of the MRD is responsible for the deterioration of performance of broadband SAVI and that SAVI is not, by nature, inadequate to broadband disturbances, as it was stated in [41]. Finally, some simulations of SAVI using the MRD model presented in chapter 2 are carried out. In these simulations, the clipped continuous SDC using a force feedback loop is implemented prior to the experimental investigation, whose results are presented in chapter 4.

3.2.2 Clipped on-off skyhook control

In equation 1.8, the clipped continuous skyhook damper control was introduced: the damping coefficient is switched between 0 and a value changing continuously over time, which justifies the name "clipped continuous" skyhook damper control. The clipped on-off version consists then to clip in a bang-bang manner, between zero current and the maximum current. However, as seen in chapter 2, the damper generates a non-zero force under zero current, which leads to a minimum value of damping coefficient C_{min}. Moreover, it has been seen that the yield force F_y saturates when the current is increased, leading the damping coefficient to reach a maximum value C_{max}. The alternative on/off strategy, consisting of switching the control current i_c as a function of time. Potentially, the current might change between 0 and its maximum value, and thus the damping coefficient from its minimum value C_{min} to its maximum value C_{max} according to the sign of $\dot{x}_p\,(\dot{x}_p - \dot{x}_b)$, i.e.

$$c_c = \begin{cases} C_{max} & \text{if } \dot{x}_p\,(\dot{x}_p - \dot{x}_b) \geq 0 \\ C_{min} & \text{if } \dot{x}_p\,(\dot{x}_p - \dot{x}_b) < 0 \end{cases} \tag{3.3}$$

This control strategy has been introduced mainly for two reasons. Historically, its introduction in the semi-active research area was motivated by the use of on-off valves in variable orifice dampers, which are less expensive than the fast responding servo-valves.

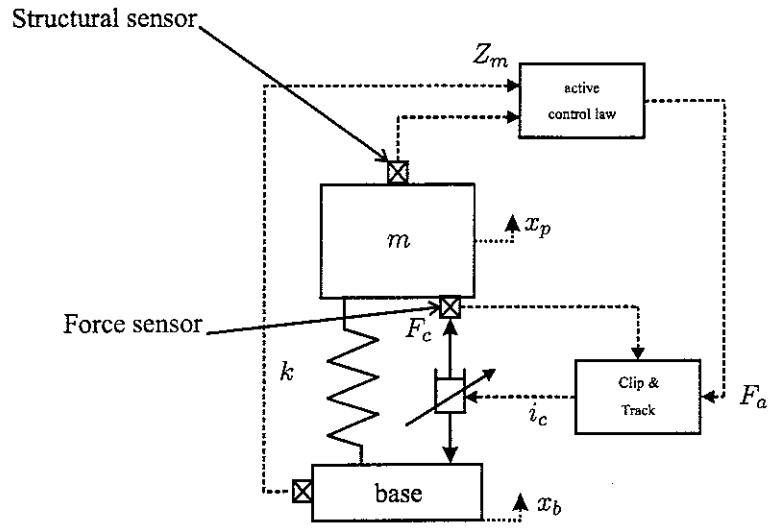

Figure 3.6: General form of a semi-active isolator.

In the area of MR dampers, which can provide by nature a continuously variable damping force[14], the clipped on-off skyhook control may be of interest since no inverse damper model is required. However, a major drawback of this control strategy is its poor isolation efficiency, as will be seen in section 3.4.1. Above the natural frequency of the mount, the transmissibility of the clipped on-off controller is almost equivalent to that of a passive isolation system whose damping coefficient is $C = \frac{C_{min}+C_{max}}{2}$, which can be detrimental if C_{max} is set to be large[15].

3.2.3 Generalised clipped continuous force feedback control

A more general semi-active strategy which applies to the emulation of any active control law is described in figure 3.6, where F_c is the MR damper force, controlled by the current i_c. Z_m is a vector of measured data that enables one to determine a desired force F_a, derived from an active controller. The semi-active isolator can be described as well in a block diagram form as seen in figure 3.7. First, an active controller calculates a desired active force F_a. Then, a secondary "clip & track" controller tries to replicate the desired force. This requires the measurement of the MRD force.

The tracking strategies can be various. Here we investigate the use of a PI controller, as

[14]This is actually one of the advantages of MR dampers, since contrary to variable orifice dampers, they can provide a continuously variable damping force without any movable part, thus they are more compact systems.

[15]which is the case if it is desired to damp the suspension resonance.

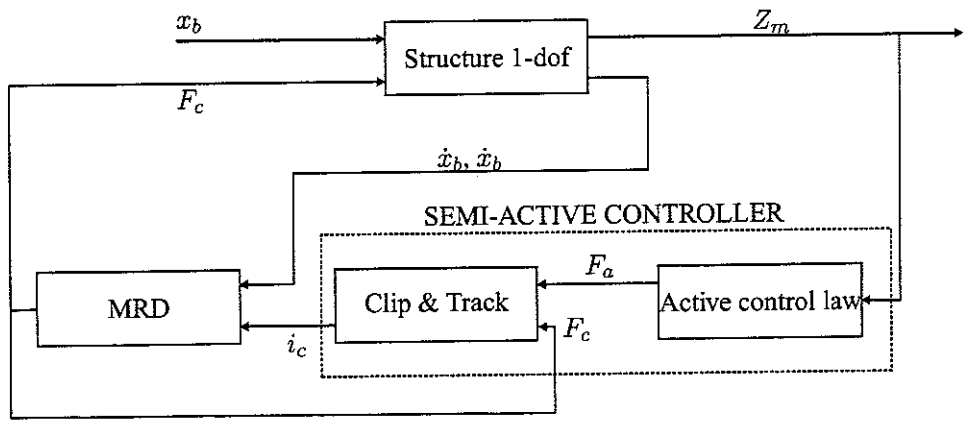

Figure 3.7: Block diagram of a general semi-active control strategy.

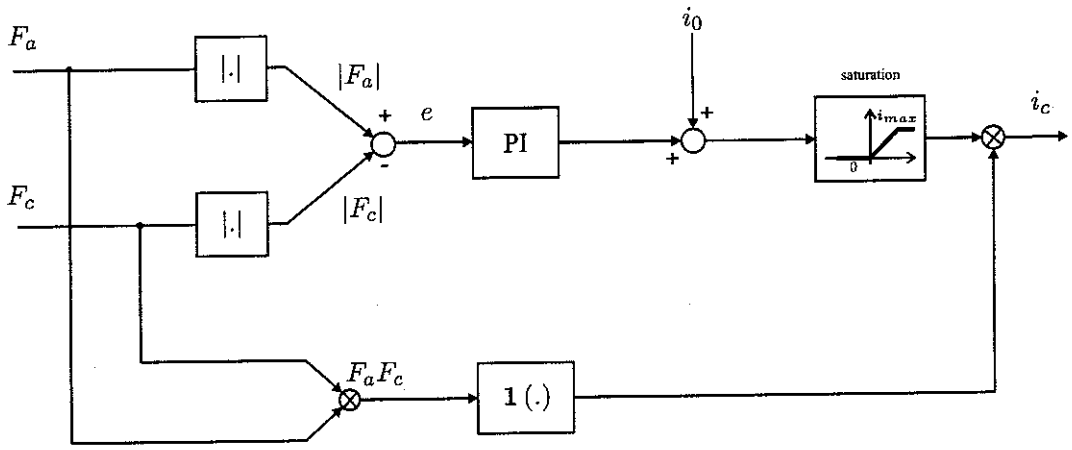

Figure 3.8: Semi-active clipped continuous force feedback control via PI controller.

shown in figure 3.8. To minimize the error between F_a and F_c, a Proportional-Integral (PI) controller is used. This PI control is realised only when F_a and F_c have the same sign (i.e. when the desired force F_a is dissipative since F_c has basically the same sign as[16] $\dot{x}_p - \dot{x}_b$, see chapter 2), hence the use of a Heaviside switching function applied to the product F_aF_c. This control is proposed in [8], without the use of the bias current i_0. This bias input is proposed in [37] in order to "increase the working band where a proportional feedback is achieved". In this study, we will not use this bias[17]. Note that in [37], a proportional controller is proposed instead of a PI controller. In [37], it is noted that in the case where the proportional gain is very large, the control is equivalent to a clipped on-off force feedback controller.

[16] except when the relative velocity changes in sign where the hysteresis effect introduce a phase lag.
[17] because the interest of such a bias is not understood

3.2.4 On-off force feedback control

As an alternative to the generalised clipped continuous force feedback approach, a clipped on-off version may be implemented. The on-off clipping strategy (figure 3.9(a)), introduced by [46], is the simplest way of achieving a tracking of the desired force. When the desired force F_a and the actual force of the damper F_c have the same sign and F_c is smaller than F_a, the current is set to its maximum value so that $|F_c|$ increases. In the opposite case, the current is set to 0 in order to have the least detrimental effect. Thus, the equation of on-off force feedback control is

$$i_c = i_{max} \mathbf{1}\left[(F_a - F_c)\, F_c\right] \tag{3.4}$$

where $\mathbf{1}(.)$ is the Heavyside function. This strategy is refered as "clipped on-off".

A variation of this strategy has been proposed in [47], where broadband disturbances were controlled with an LQG approach. It consists in applying a threshold to the controlled force, i.e. the control current remains zero below a minimum force F_{min}. The motivation of this threshold, presented in [47], is that "the desired force includes an offset and some noise because the sensor outputs in the experiment include some dc offset and noise as well. The influence of these errors can be significant in the case of small vibration. Thus, the controller may send an incorrect signal to the damper, especially for ambient vibration." However, in this study, we understand that the real motivation for applying a threshold in the clip & track strategy is that it enhances the performance of isolation of broadband disturbance, particularly at high frequencies, where it is not desirable to introduce damping. This clipped on-off strategy with threshold is schematized in figure 3.9(b) and described by the control law

$$i_c = \begin{cases} i_{max} \mathbf{1}\left[(F_a - F_c)\, F_c\right] & \text{if } F_a \geq F_{min} \\ 0 & \text{if } F_a < F_{min} \end{cases} \tag{3.5}$$

In [47], this last controller has been compared to other semi-active controllers. Associated with an optimal controller such as LQG for the active part of the semi-active control strategy, it has been proved to be well-adapted for broadband excitations such as those encountered in seismic control (where the disturbance spectrum is not very wide however).

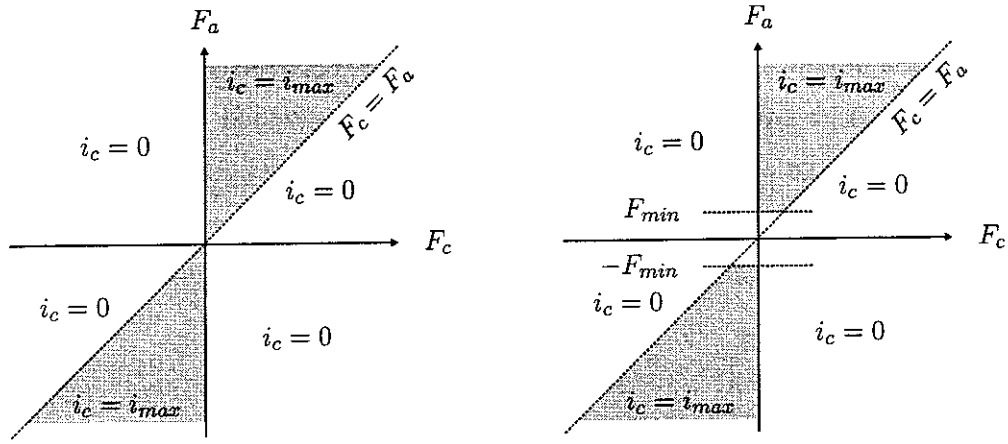

(a) Without threshold

(b) With threshold

Figure 3.9: Clipped on-off controller.

3.2.5 About the emulated active controller

The active skyhook damper control has been extensively discussed in section 1.1.2 and chapter 5. The aim of this section is to discuss LQG control and to compare it with skyhook control. However, it has been found that LQG does not give significantly better performance than skyhook damper control in the 1 dof isolation system configuration. Actually, the skyhook damper control can be derived from LQG control by regulating the deflection of the mount and the absolute payload velocity, see [1]. For brevity, we do not discuss LQG control further. The LQG controller as a MIMO controller will probably be of interest with regard to the hexapod isolation system, in so far as the coupling between the struts reduces the performance of a multi-SISO approach (a feedback loop between the accelerometer and the actuator/MR damper in each strut).

3.3 Optimisation of the mechanical design of the isolation mount taking into account MR damper dynamics

3.3.1 Presentation of the problem

In section 1.1.3, it has been seen that, in theory, a semi-active skyhook control with a clipped continuous strategy can emulate very closely an active skyhook controller in terms of performance of displacement transmissibility (figure 1.9). However, from the-

ory to practical implementation, there exist some differences, which can deteriorate the performance of the isolation system using semi-active control. In particular, there exist some hardware limitations inherent in the MR damper, such as the minimum damping force under zero current, the maximum deliverable damping force of the damper and the response time of the magnetic coil to produce a desired current. In this section, the effects of hardware limitations on isolation performance are discussed regardless of the limits due to the practical implementation of the controller (such the implementation of the clipped continuous strategy using force feedback, see section 3.2.3), and regardless of the non-linear effects of the MR damper. The idealised damper represented in figure 3.2 is used in the isolation mount and is controlled by a skyhook damper controller with a clipped continuous strategy, used as a reference control strategy. This analysis gives an upper bound of the performance that an isolation mount using a MR damper can achieve.

Two types of mechanical design problems can be considered:

- **Case 1:** given a payload of a certain mass that is to be isolated from 5 Hz upwards, what stiffness should be chosen, and what are the desired properties of the controllable damper? This problem is an illustration, on a single axis configuration, of the problem of the design of the launch vibration isolation system. Concerning the choice of stiffness, it has been shown that a natural frequency of 2 Hz may meet the isolation objectives, but that a natural frequency around 3 Hz would be more appropriate with the constraint of permitted quasi-static deflection (see section 5.1). As a consequence, it will be shown in this part that, for sinusoidal excitations and a 3 Hz natural frequency, 12 dB of attenuation is not achievable from 5 Hz upwards, but can occur from around 7 Hz upwards. It is possible to obtain around 8 dB attenuation at 5 Hz. The aim of this section is to find the best achievable isolation performance with a 3 Hz isolation system.

- **Case 2:** given the properties of an existing controllable damper, for which values of mass and stiffness is the damper best suited? In the single axis experiment, which is aimed at demonstrating the feasibility of a semi-active isolation mount, we are faced with this type of problem. Additional contraints exist: the hydraulic exciting system has a limited available power, so the mass is limited. Moreover, the coil springs available on the market have a minimum stiffness. The features of the experimental isolation mount are summarized in table 3.1.

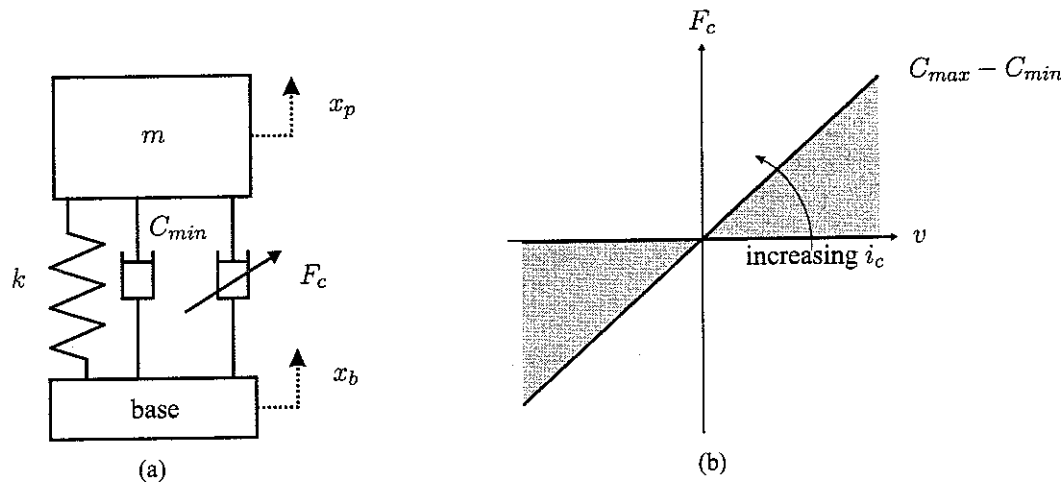

Figure 3.10: Equivalent isolation mount with a zero damping coefficient controllable damper.

$f_n(Hz)$	$m(kg)$	$k(kNm^{-1})$
4.57	110	90.7

Table 3.1: Features of the single axis semi-active isolation system used in the experiment and in some simulations.

3.3.2 Limitation due to the damping coefficient at zero current

The controllable damper has a minimum damping coefficient C_{min} at zero current and the corresponding minimum damping ratio is $\xi_{min} = \frac{C_{min}}{2M\omega_n}$. As a consequence, the isolation system is the equivalent of the mount represented in figure 3.10, where a controllable damper with zero damping coefficient at zero current is in parallel with a passive damper of damping coefficient C_{min}.

Thus, this system is the emulation of an active skyhook damper with an additional passive damper whose transfer function is given in equation 1.4. The detrimental effect of added damping on high frequency control has been seen in figure 1.7. Obviously, the same effect is present in a semi-active system as illustrated in figure 3.11, where an ideal damper without any response delays and with no restriction on the maximum deliverable force has been simulated.

From this observation, if an MR damper is to be designed, it follows that the minimum damping force under zero current has to be considered and minimised. This recommen-

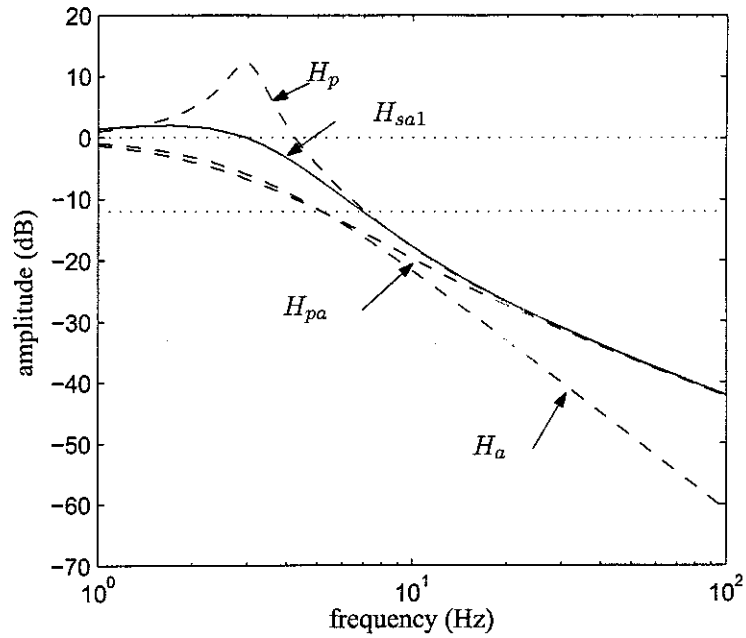

Figure 3.11: High frequency limitation of SA SDC due to ξ_{min}. $f_n = 3Hz$. H_p: passive isolator (zero current, $\xi_p = 0.127$). H_a: active isolator ($\xi_{sky} = 1$). H_{pa}: active isolator with added damping ($\xi_{sky} = 1$ and $\xi_p = 0.127$). H_{sa1} transmissibity for SA SDC , with $\xi_{min} = 0.127$.

dation was also reported in [40]. However, as will be seen, another limitation on the maximum deliverable force adds a constraint on the choice of ξ_{min}.

3.3.3 Limitation due to the maximum damping coefficient

MR dampers have a limited force range due to saturation of the yield force with current resulting in a maximum damping coefficient C_{max}. On the specimen used in the experiment, the MR damper has a maximum deliverable force of about 1200 N at $i_c = 2$ A, at a velocity of 0.1 ms^{-1}. This limitation on the maximum deliverable force is crucial because it determines the ability of the semi-active controller to damp the vibrations around the suspension natural frequency. This is illustrated in figure 3.12 for 3 values of the maximum damping ratios: 10, 5 and 2 times the value of the minimum damping ratio. If the maximum deliverable force is less than the desired force (case $\xi_{max} = 2\ \xi_{min}$ for instance), the vibrations around the suspension natural frequency are not damped enough. So the maximum value of ξ_{max} has to be such that the MR damper might is able to produce any desired force.

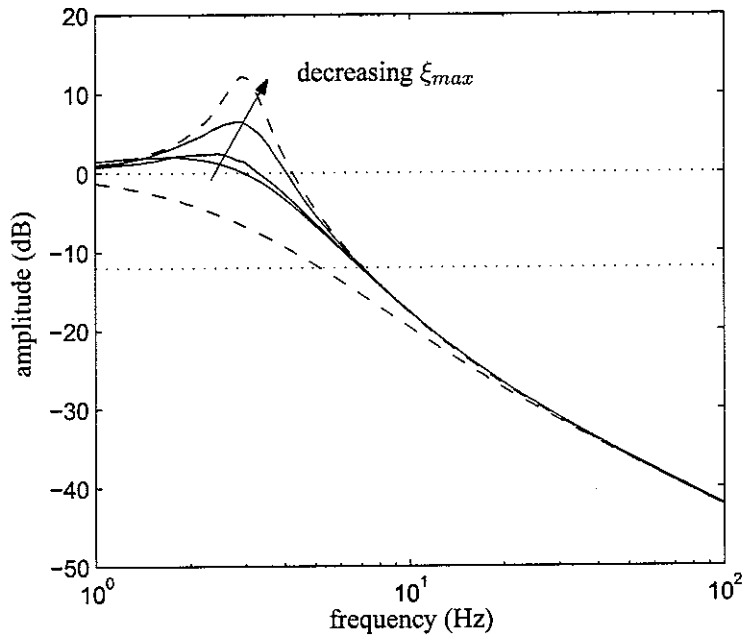

Figure 3.12: Influence of the maximum deliverable force on the isolation performance. 3 Hz isolator configuration with $\xi_{min} = 0.127$, no response time of the magnetic coil, explicit skyhook damper strategy. (dashed lines) H_p and H_{pa} with $\xi_{sky} = 1$ and $\xi_p = 0.127$. (solid lines) H_{sa1} for 3 values of maximum damping ratios: $\xi_{max} = (10,\ 5,\ 2)\,\xi_{min}$.

In figure 3.13, it is interesting to note that the semi-active isolator combines the best features of the passive "off" (zero current, $\xi_p = \xi_{min}$) and the passive "on" (maximum current, $\xi_p = \xi_{max}$) dampers. At low frequencies, the transmissibility of the semi-active isolation system tends to that of the passive system with $\xi_p = \xi_{max}$, while at high frequencies, it tends to that of the passive system with $\xi_p = \xi_{min}$.

3.3.4 Limitation due to response time of the electrical circuit

The magnetic field in the MR damper valve is created by an electric coil. This coil is a LR circuit, L and R being the inductance and the resistance of the coil. The current i_c flowing through the coil is governed by the equation

$$L\frac{di_c}{dt} + Ri_c = U \tag{3.6}$$

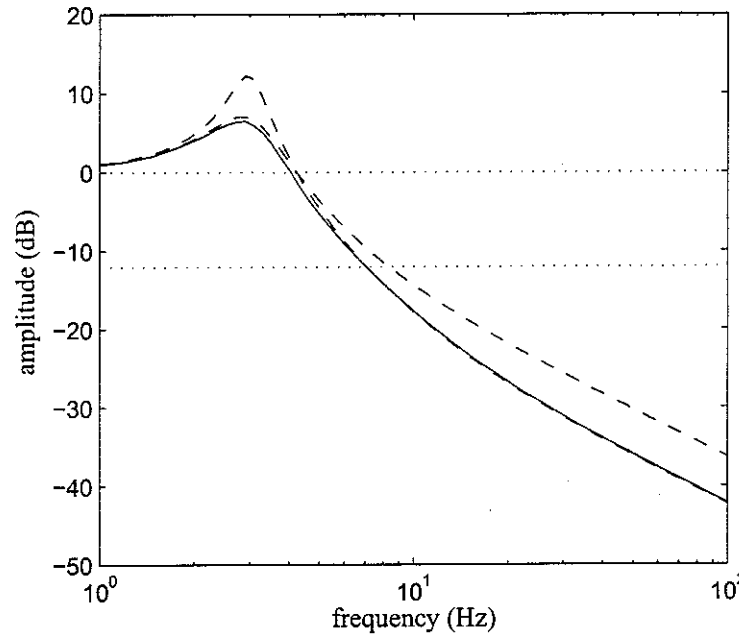

Figure 3.13: Comparison of the SA transmissibility (H_{sal}) for $\xi_{min} = 0.127$, $\xi_{max} = 0.254$ (solid line) with the passive isolator transmissibilities for $\xi_p = 0.127$ and $\xi_p = 0.254$ (dashed lines).

where U is the voltage applied to the electrical load. Thus the time constant of the coil is

$$\tau = \frac{L}{R} \tag{3.7}$$

Measurements of L and R on the MR damper used in the experiment give $\tau = 25$ ms, which is quite large if we consider that, for a step input, the 95% settling time is attained after $t = 3\tau$ and that for a sine excitation, the controller makes the current clip 4 times during one period (figure 3.5). According to these considerations, the electrical time constant of the coil should satisfy

$$\tau \leq \frac{1}{12 f_{exc}} \tag{3.8}$$

where f_{exc} is the frequency of the disturbance signal.

We can consider that the control bandwidth of the controllable damper has to be at least from 0 to 2.33 f_n Hz, the higher frequency being approximately the frequency above which the attenuation is at least 12 dB. In case 1, (3 Hz isolation system), $f_n = 3$ Hz.

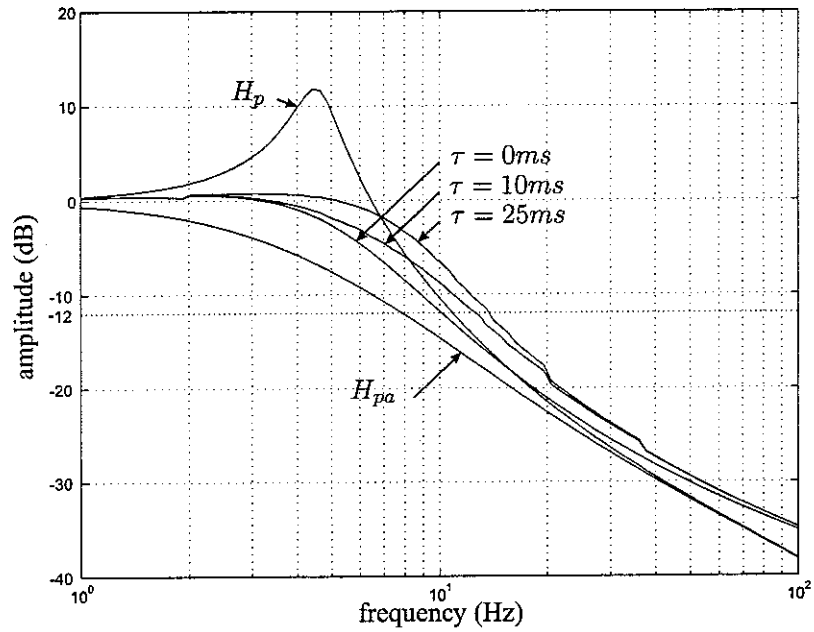

Figure 3.14: Effect of the response time. $f_n = 4.57Hz$. H_p: passive isolator (zero current, $\xi_p = 0.127$). H_{pa}: active isolator with added damping ($\xi_{sky} = 1$ and $\xi_p = 0.127$). The other curves are H_{sa1} transmissibility ($\xi_{min} = 0.127$ and $\xi_{max} = 1.27$) for different electrical time constants.

This implies that τ should not be greater than 12 ms. Fortunately, the current is controlled by a PWM driver (Pulse Width Modulation, see [8]), which decreases the time constant to 10 ms. The PWM driver has a non-linear response, but can be modelled in a first approximation by a first order system, which is done in the simulations. In case 2, (4.57 Hz isolation system), $f_n = 4.57$ Hz. This implies that τ should not be greater than 7 ms. As a consequence, the response time of the electrical circuit in the experimental case presented in the next chapter is a limiting factor.

Taking into account different electrical time constants, the effect of electrical circuit response time on transmissibility can be seen in figure 3.14. While the time constant increases from 0 ms to 10 ms and 25 ms, the cut-off frequency at -12 dB moves from 10 Hz to 12.5 Hz and 13.5 Hz.

3.3.5 Optimal design of a semi-active isolator

In the previous sections, it has been seen that ξ_{min} has to be as low as possible whereas ξ_{max} needs to be large enough. These two objectives of the mechanical design are con-

flicting in so far as the force range of real, controllable dampers is limited. It leads to a trade-off in the choice of those parameters. For example, the MR damper commercialised by the Lord Corporation, the RD-1005-3, used in the experimental setup, has a force range from about 120 N at $i_c = 0$ A, to about 1200 N at $i_c = 2$ A, for a piston velocity of 0.1 ms^{-1}. Thus, whatever the mass of the payload and the stiffness of the isolation mount, the approximate damping force range is such that

$$\frac{F_{max}}{F_{min}} = 10 \tag{3.9}$$

In some studies, such as [48] or [33], as well as in our experimental configuration, the whole force range of the damper is not exploited because the damper may not have been designed optimally for the actual configuration of the isolation mount, or because the isolation mount has not been optimised for the MR damper (the case of our experimental setup). Here, it is recommended that the whole force range of the damper should be exploited. This leads to the constraint

$$F_{max}^{used} = F_{max}^{available} \tag{3.10}$$

If we denote $\xi_{max} = \frac{C_{max}^{used}}{2M\omega_n}$, the constraint may be written as

$$\xi_{min} = \frac{\xi_{max}}{10} \tag{3.11}$$

There remains one degree of freedom in the choice of the above parameters, let us say ξ_{max}. On the other hand, to enhance control performance of the clipped continuous sky-hook damper control strategy, Karnopp ([25]) recommends that the gain of the desired force be increased, that is to say c_{sky}, and consequently ξ_{sky}. However, increase in isolation performance only occurs with respect to the RMS transmissibilities and the maximum displacement transmissibility (H_{sa2}, H_{sa3} and H_{sa4}). The increase of ξ_{sky} is not necessarily relevant as regards the maximum acceleration transmissibility H_{sa1}. We know as well that a low level of feedback gain c_{sky} has the consequence of decreasing the isolation performance. As a consequence, there is also a compromise on the choice of ξ_{sky}, as illustrated in figure 3.15.

3.3.5.1 *Optimisation of the parameters for a 3 Hz isolation configuration*

In this section a parametric study concerning the choice of ξ_{sky} and ξ_{max} is proposed as follows: which set of (ξ_{sky}, ξ_{max}) optimises the isolation performance of the 3 Hz isolation mount configuration, for a clipped continuous skyhook damper strategy, while using the whole force range of the controllable damper? It remains to define an index of isolation performance.

It is not desired to produce a very high attenuation rate at high frequencies, provided that the attenuation is at least of 12 dB. The goal is to provide this level of attenuation from the lowest frequency possible, while not producing amplification around the resonance frequency. It follows that the performance index may be expressed as

$$J = \int_{\omega_{min}}^{\omega_{-12}} \left(G_{sa1}(\omega) - (-12)\right) d\omega \tag{3.12}$$

where $G_{sa1} = 20 \log_{10} |H_{sa1}|$ and ω_{-12} is the frequency such that $G_{sa1}(\omega) \leq -12\ dB$ if $\omega \geq \omega_{-12}$. This performance index is the area between the magnitude of the transmissibility (in dB) and the goal of attenuation, as illustrated in figure 3.15. Note that the solution of the optimisation problem is depends on the performance index, whether it is defined with a linear or logarithmic scale.

The optimisation problem described above is written mathematically as

$$\min_{\Xi} J \tag{3.13}$$

where $\Xi = (\xi_{sky}, \xi_{max})$.

To find this minimum, the Matlab function "fminsearch" is used, which is based on the Nelder-Mead simplex optimisation algorithm, [49]. This method is particularly suited to low order problems. This is a direct search method that does not use numerical or analytic gradients. If n is the number of parameters, a simplex in n-dimensional space is characterized by the $n + 1$ distinct vectors that are its vertices. In two-space, a simplex is a triangle; in three-space, it is a pyramid. At each step of the search, a new point in or near the current simplex is generated. The function value at the new point is compared

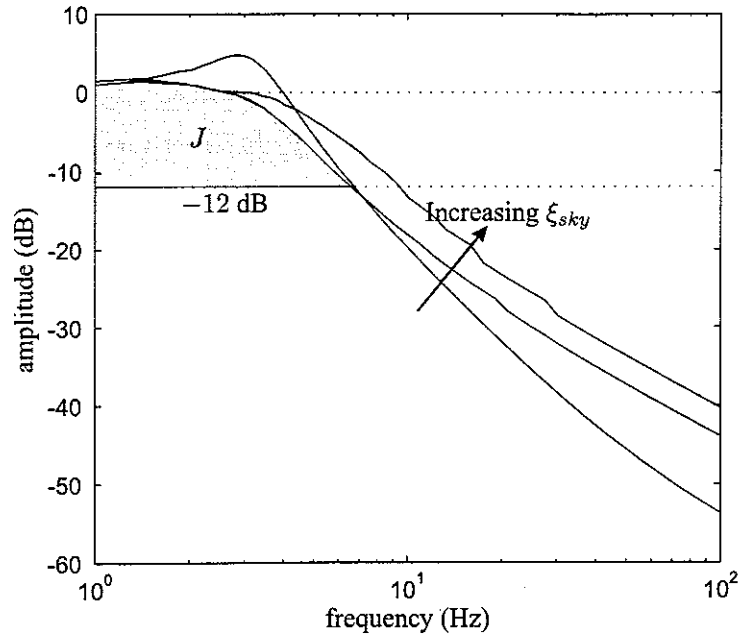

Figure 3.15: Performance of the semi-active 3 Hz isolation system (H_{sa1}) for 3 values of ξ_{sky}: $0.2, 1, 1.5$ with $\xi_{max} = 1.3\ \xi_{sky}$ and $\xi_{min} = 0.1\ \xi_{max}$. In grey, performance index J for $\xi_{sky} = 1$.

with the function's values at the vertices of the simplex and, usually, one of the vertices is replaced by the new point, giving a new simplex. This step is repeated until the diameter of the simplex is less than the specified tolerance.

In this study, the individual steps of the optimisation process were the following:

1. Pre-processing phase: Compute the performance index for a rough mesh of Ξ in the bounds $[0.2, 1.6] \times [0.25, 3]$.

2. Pre-processing phase: Plot the graph surface $J(\Xi)$. In so far as the surface seems convex, assume that there is a global minimum, apparently located around $\Xi = (1, 1)$ for the example considered here.

3. Processing phase : proceed to the optimisation algorithm with a starting guess $\Xi_0 = (1, 1)$. After 40 iterations with 77 evaluations of J, the evaluated solution is $\Xi = (0.92, 1.27)$ (to 2 decimal places).

4. Post-processing phase: Compute the performance index for a mesh of Ξ in the bounds $[0.2, 1.6] \times [0.25, 3]$ refined around the minimum found by the algorithm.

The results are shown in figure 3.16 where contours of J are plotted. The surface appears to be convex and we can hence infer that the algorithm locates a global minimum. Moreover, this surface is characterised by a gradient around the minimum that varies slowly as a function of the parameters. This means that a whole region of Ξ-space gives a performance close to the optimal performance. In practice, it is found that there is a change of less than 5% in J in the region $\Xi = [0.8,\ 1] \times [1,\ 1.5]$. We can retain one major design recommendation: $\frac{\xi_{max}}{\xi_{sky}} \geq 1.25$ with $0.7 \leq \xi_{sky} \leq 1$.

The feedback gain of the emulated skyhook damper control has to be close to critical damping, but surprisingly, must not be higher, which is contradictory with a result found in [25]. In this paper it was found that, with regard to the RMS displacement transmissibility H_{sa4}, it was favourable to increase the feedback gain[18]. Here, we find that too large a feedback gain is not only detrimental to H_{sa1}, but also to H_{sa4}, as can be seen in figure 3.17. The cause of this phenomenon might be the time delay induced by the electrical circuit, which was not considered in [25].

Concerning the optimised isolation system found in this simulation, we can see that the isolation performance is quite satisfactory because the amplification around resonance, summarized in table 3.2, is low, and the system provides isolation of -12 dB from 6.8 Hz upwards, while at 5 Hz the attenuation is 7.4 dB. Of course, this is less than the initial design objectives of the problem (-12 dB from 5 Hz upwards).

Finally, the figure 3.18 shows a time sequence for a sinusoidal excitation at 3 Hz. We can notice two aspects. Firstly, the response time of the coil has a natural antijerk effect[19], as can be seen by the payload acceleration response. Secondly, the amplitude of $\dot{x}_b - \dot{x}_p$ is lower than the amplitude of $\dot{x}_p$, which explains the recommendation written as $\frac{\xi_{max}}{\xi_{sky}} \geq 1.25$.

	H_{sa1}	H_{sa2}	H_{sa3}	H_{sa4}
amplification (%)	16	16	7	10
amplification (dB)	1.3	1.3	0.6	0.9

Table 3.2: Level of amplification around resonance for various performance criteria. Optimised semi-active isolation system.

[18] to the detriment of maximum acceleration transmissibilities, which was not reported in the paper.

[19] the jerk is the derivative of acceleration. It can be a cause of incomfort, so it is often considered in automotive applications using semi-active control. Indeed, by clipping on and off the current in a short time, the magnitude of the force, and so of the acceleration, can suddenly change, causing high jerk.

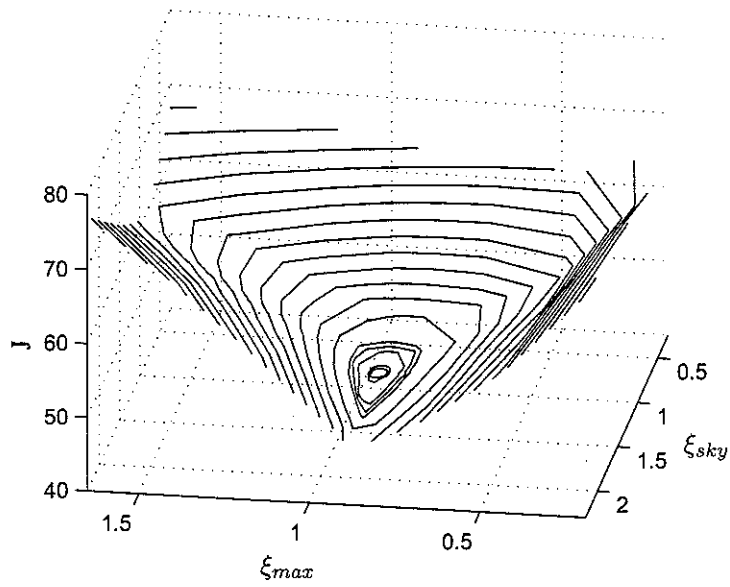

Figure 3.16: Three-dimensional contour graph of the surface $J(\Xi)$.

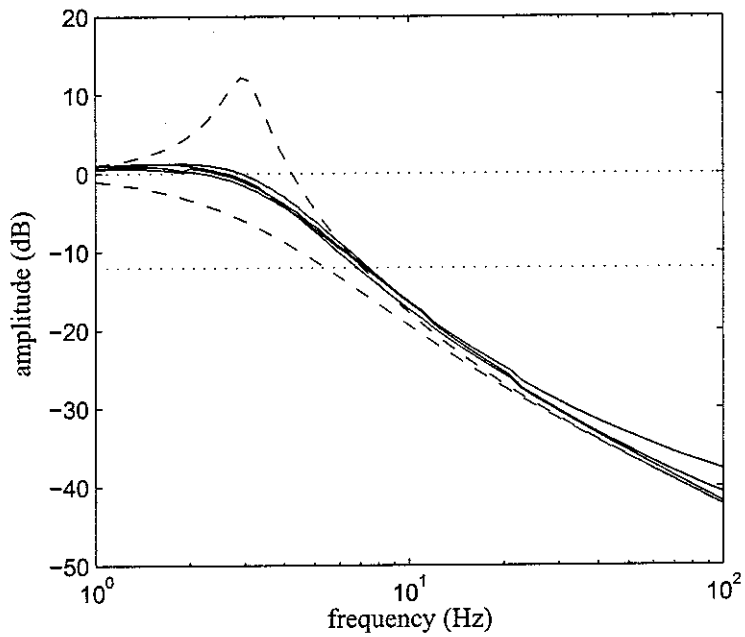

Figure 3.17: Isolation performance of the clipped continuous skyhook control for the optimal set of parameters: $\xi_{sky} = 0.92$, $\xi_{max} = 1.27$ and $\xi_{min} = 0.127$. In solid lines, H_{sai}, $i = [1, 4]$. In dotted lines, H_p passive isolation for $\xi_p = 0.127$ and H_{pa} active skyhook damper isolation $\xi_{sky} = 0.92$ with passive damping $\xi_p = 0.127$.

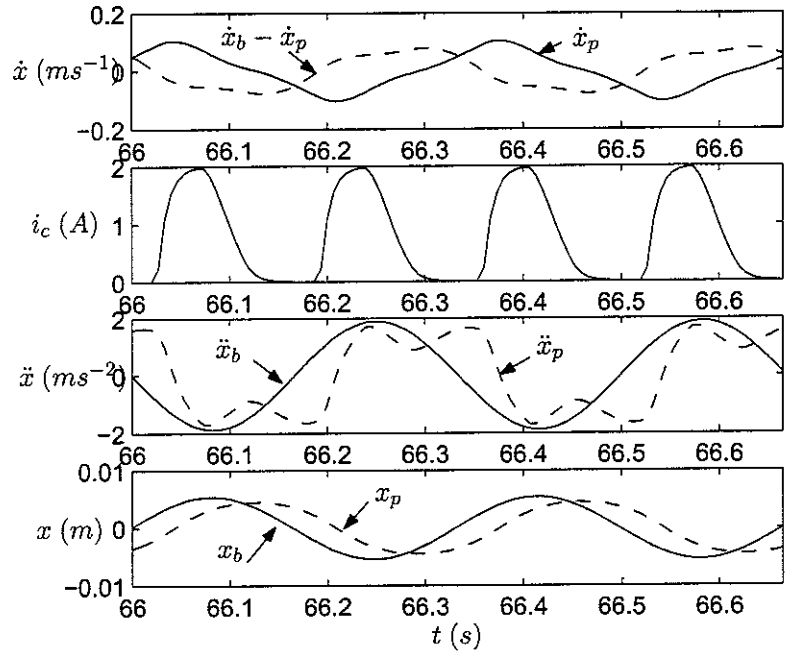

Figure 3.18: Time sequence of some isolation system variables during semi-active control, under a sinusoidal excitation at 3 Hz.

3.3.5.2 Robustness of the optimal set of parameters

The first question is: "Is the optimal set of parameters found in the previous part robust with respect to the payload mass, provided that the isolator natural frequency remains the same?" The answer is "yes": the same simulations as before are repeated but with the payload mass changed from 110 kg (experimental setup) to 3000 kg (the order of a satellite mass), while keeping the natural frequency of the isolator at 3 Hz. The optimal set of parameters remains the same. This is due to the fact that we work with damping ratios ξ, and not with damping coefficient C.

The second question is: "Is the optimal set of parameters found in the previous part robust with respect to the natural frequency of the isolation system ?" The answer is "no": the same simulations as before are done by setting the natural frequency of the isolator to 4.57 Hz, which is the configuration of the experimental setup. The optimal set of parameters is found to be $\xi_{sky} = 0.76$, $\xi_{max} = 1.20$ and $\xi_{min} = 0.12$.

The optimisation problem depends on factors additional to the suspension frequency, such as:

- the nature of disturbance. Here the problem is optimised for sinusoidal excitation at random frequencies;
- the semi-active control strategy;
- the response time of the controllable damper.

So a particular case results in a particular solution. However the interest of this study is to provide a general guideline to the optimisation of semi-active isolation systems. Moreover, whatever the configuration of control and isolation frequency, three recommendations would seem to be

$$F_{max}^{used} = F_{max}^{available} \tag{3.14}$$

$$\frac{F_{max}}{F_a} \geq 1.25 \tag{3.15}$$

$$0.7 \leq \xi_{sky} \leq 1.1 \tag{3.16}$$

where F_a is the amplitude of the prescribed active control force.

It is to be noticed, that for random inputs, there are rare, very large, prescribed forces. It could be desired to limit F_{max}^{used} in order to give a better ξ_{max}/ξ_{min}.

3.3.5.3 Recommendations for the experimental setup

According to the foregoing observations, an optimal design of the experimental setup, aimed at demonstrating the performance of semi-active control using MR dampers, employing the MR damper RD-1005-3 of Lord Corporation can be defined. This should provide the best attenuation in the 5-100 Hz frequency range, with respect to the performance index defined in equation 3.12. The parameters are listed in table 3.3.

$f_n(Hz)$	$m(kg)$	$k(kNm^{-1})$	ξ_{min}	ξ_{max}	ξ_{sky}
3	250	88.8	0.127	1.27	0.92

Table 3.3: Optimal features of the experimental demonstrator of single-axis semi-active isolation system

However, as already mentioned, it was not possible to construct a 3 Hz isolation system with the available rig, so a 4.57 Hz isolation was used. With this isolation frequency, the optimal set of parameters are listed in table 3.4.

$f_n(Hz)$	$m(kg)$	$k(kNm^{-1})$	ξ_{min}	ξ_{max}	ξ_{sky}
4.57	265	218.5	0.12	1.20	0.76

Table 3.4: Optimal features of the experimental demonstrator of single-axis semi-active isolation system, for a 4.57 Hz natural frequency

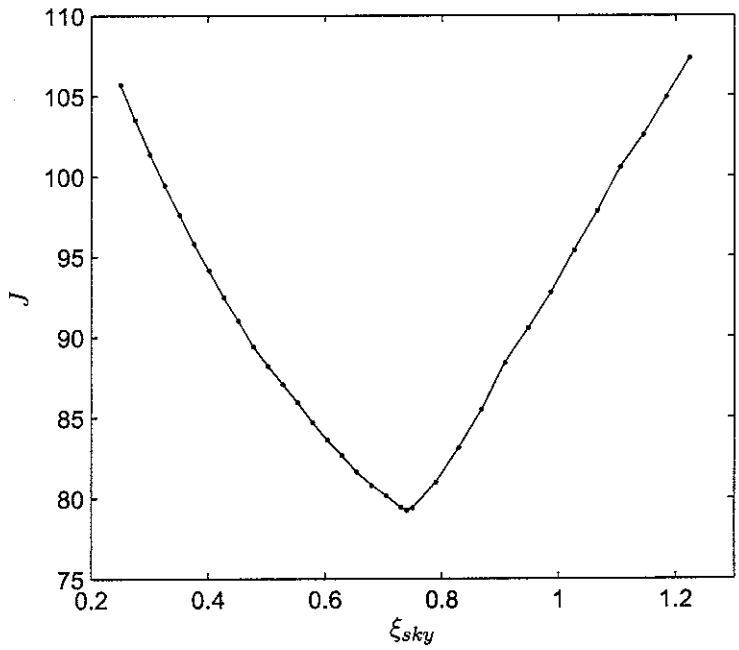

Figure 3.19: Performance index as a function of ξ_{sky} for the actual experimental setup with $f_n = 4.57Hz$, $\xi_{max} = 2$ and $\xi_{min} = 0.2$.

Finally, because a mass of 265 kg is not easy to excitate in the experiment (because of the limited hydraulic power), the configuration used in the experiment is described in table 3.5. For the MR damper RD-1005-3, the nominal damping ratios for the mass and stiffness parameters listed in table 3.5 are $\xi_{min} = 0.2$ and $\xi_{max} = 2$ (for a velocity amplitude of $0.1\ ms^{-1}$), which is not optimal.

Another optimisation process has been carried out to find the optimal value of ξ_{sky} for this system. The results are shown in figure 3.19. The optimal value of ξ_{sky} is $\xi_{sky} = 0.73$.

$f_n(Hz)$	$m(kg)$	$k(kNm^{-1})$	ξ_{min}	ξ_{max}	ξ_{sky}
4.57	110	59.4	0.2	2	0.73

Table 3.5: Features of the actual experimental demonstrator

3.4 Simulation results

In the previous section, four implementations of the skyhook damper control have been described. In this section, their performance are evaluated for different excitation cases, and compared to the performance of the clipped continuous skyhook damper control, explicitely implemented with the idealised controllable damper presented in figure 3.2.

3.4.1 Limits of clipped on-off methods for tonal disturbances

To evaluate the isolation performance of this simple strategy, the idealised damper model with an instantaneous time response ($\tau = 0$ ms) is used, which provides an upper bound of the isolation performance that a MR damper could achieve with the explicit clipped on-off strategy. The performance is evaluated for tonal excitations at various frequencies. The natural frequency of the isolator is chosen to be 3 Hz. In order to damp correctly the isolator mode, a minimum value of ξ_{max} is required. This value is chosen to be $\xi_{max} = 1.27$. The minimum damping ratio is supposed to be ten times smaller than its maximum damping ratio, that is to say $\xi_{min} = 0.127$.

The performance of the clipped on-off skyhook damper control presented in the figure 3.20 can be compared to figure 3.17 for the continuous version. The isolation frequency at -12 dB moves from 6.8 Hz (continuous) to 16 Hz (on-off), this without even considering any time delay due to the magnetic coil. The performance of the clipped on-off skyhook damper control is much worse that the clipped continuous version. Indeed, as shown in figure 3.20, the semi-active isolation performance is very close:

- to that of a passive isolation system with a damping ratio of $\xi = \frac{\xi_{min}+\xi_{max}}{2}$, at high frequency;
- to that of a passive isolation system with $\xi = \xi_{max}$, at low frequency.

As a consequence, compared to the passive system with $\xi = \frac{\xi_{min}+\xi_{max}}{2}$, there is only 1dB (10%) of improvement around the resonance. So, it is probably not necessary to implement a semi-active isolation system for such a marginal improvement. Note however that in terms of the other transmissibilities the isolation performance is better: the frequency of isolation at -12 dB occurs at 10 and 7 Hz respectively for H_{sa2} and H_{sa3}. It is worth noting

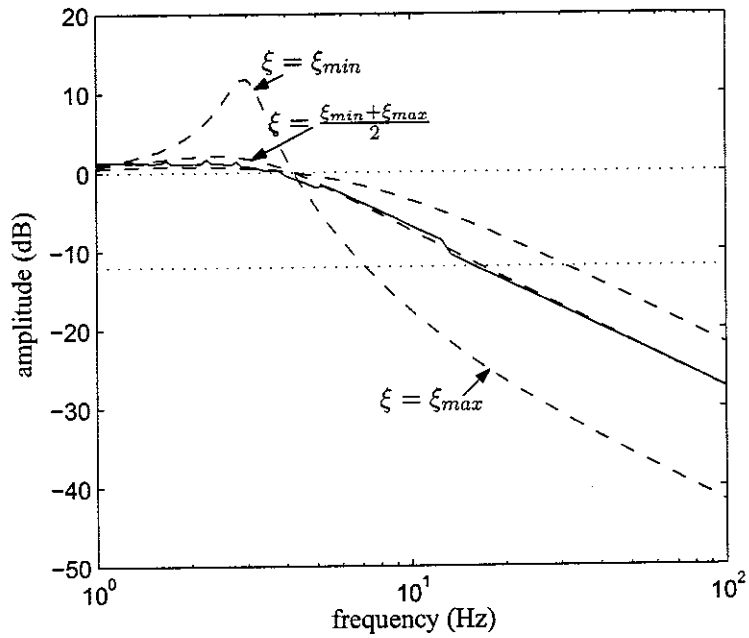

Figure 3.20: Performance of the clipped on-off skyhook damper control with $\xi_{min} = 0.127$ and $\xi_{max} = 1.2$ (H_{sa1}). (solid line) semi-active control, (dashed) passive isolator for various damping ratios.

that several studies (e.g. [33], [50]) compare the performance of the clipped on-off control (and other semi-active controls) with the performance of the passive off ($\xi = \xi_{min}$) and the passive on ($\xi = \xi_{max}$). Some of these studies conclude that, under certain type of excitations (either low frequency or high, but not in a wide frequency range), the semi-active system provides better results than such passive systems. However, we conclude here that the clipped on-off strategy is nearly equivalent to a passive system with $\xi = \frac{\xi_{min}+\xi_{max}}{2}$. This observation is similar to some conclusions found in [48], where a set of four MR dampers were installed on heavy truck primary suspension.

The utilization of this control strategy is therefore very arguable. The interest of such a method could be for broadband disturbances using a force threshold, as presented in equation 3.5. Indeed, for broadband disturbances, clipped continuous methods provide less good efficiency than for tonal disturbances, because of the response time of the damper, as it is shown in the next section. However, a mean to reduce the electrical time delay is the use of very fast electrical switches, which are only suited to on-off control. Further investigations on this subject could be interesting.

3.4.2 Semi-active isolation of broadband disturbances - Time delay effect

This section is aimed at establishing some upper bound of what could be achievable using a MR damper for broadband vibration. In section 3.3.5, tonal excitation has been extensively discussed. It was shown that, for an optimised suspension system, isolation at -12 dB occurs from 6.8 Hz upwards. In this section, we focus on the performance of SAVI for broadband disturbance. The test case used as reference of broadband disturbance is a random white-noise base velocity.

To establish the upper limit of performance, the explicit version of the clipped continuous SDC is implemented, as was done in section 3.3.5. As a consequence, we use the idealised controllable damper model and its inverted model, to avoid the resort of the force feedback control loop, which could be an additional factor of performance deterioration.

3.4.2.1 The problem of broadband SAVI.

As seen in the previous section, SAVI works well for narrowband disturbances. However, it would be totally erroneous to conclude that this is the case as well for broadband disturbances, since SA control is inherently non-linear. One has therefore to be cautious concerning the use of SAVI for broadband excitations, because SA control "tends to be less effective when subjected to wide-band disturbances", as it is shown in [37]. Moreover, an additional factor, usually neglected and perhaps more important than the way SA control inherently operates, is the presence of time delays in the damping device. In [41], it is explained that SAVI "faces the difficulty that the relative velocity between the two bodies $\dot{x}_p - \dot{x}_b$ on which the SA controller operates contains higher frequency components than $\dot{x}_p$, which one tries to emulate". This assertion is true but maybe not damning. In fact, as shown in [25] for a white-noise base velocity between 0.8 Hz and 15 Hz, and as figures 3.21(a) and 3.21(b) show for a white-noise base velocity between 0.5 Hz and 50 Hz (first-order band-pass filter), the performance is quite acceptable and even close to the narrowband case, if there is no time delay.

3.4.2.2 *Effect of time delay.*

As soon as we introduce a time delay, for instance through a time constant of 10 ms (typical of an MRD), the performance deteriorates, see Figure 3.21(a), for the same reasons as explained in the narrowband case, that is to say that the delay induces some damping during the non-dissipative phases, as shown in Figure 3.21(c). But contrary to the narrowband case, the frequency of transition from non-dissipative to dissipative behaviour is roughly equal to the highest frequency of the spectrum of $\dot{x}_b$. Thus, the bandwidth of currently available controllable dampers does not enable one to achieve SAVI performance that is comparable to AVI.

However, SAVI performance can remain significantly better than any passive system for broadband disturbance, at least with disturbance spectra of moderate frequency bandwidth, as the experimental results presented in the next chapter show.

3.4.3 Clipped continuous force feedback control

The simulation results of the chosen control strategy, the so-called clipped continuous strategy with a force feedback proportional loop, are not reported here for the sake of brevity. However, it is to be noticed that the simulations with the MR damper model developed in the previous chapter have proved a priori satisfactory performance of the controller, for both tonal and broadband disturbances. This performance is quantitatively evaluated in the experimental measurements reported in the next chapter. More importantly, it is worth noting that the control simulations seem quite predictive, since the control gains values, i.e. K_p (force feedback gain) and c_{sky} (skyhook gain), have been predimensionned in simulation and the same order of optimal values ($K_p \cong 0.1$, $\xi_{sky} \cong 1$) were found experimentally. Further investigations on the predictability of simulation will be carried out, by comparing the time and frequency responses, in order to know exactly whether the simulations are fully predictible, or gives simply good orders of values (which is already a noticeable progress).

3.5 Summary

In this chapter, some simulations of semi-active isolation for a single degree-of-freedom were presented. First, the simulation methodology is explained: the simulation are carried out in the time domain using Matlab-Simulink, the excitations taken into account are narrowband and broadband and the criteria of isolation performance are defined. Two models of controllable dampers are used. An idealised controllable damper is defined to perform some simulations of explicit Semi-Active (SA) Skyhook Damper Control (SDC), in order to have a physical insight on the limitations of performance of SA control and to find an upper bound of the performance that can be achieved with actual devices. To carry out predictive simulations of control using an MR damper, the MR damper model developed in chapter 2 is used.

Because of the non-linearity of the MR damper, the explicit version of SA SDC can not be used, and one must resort to more complicated control laws. A review of SA control strategies found in the literature is done. Among the various existing strategies, the clipped continuous control using a force feedback loop is chosen and applied to SDC for the single dof study.

Various simulation results are presented. First, an optimisation of the mechanical and control parameters of the SA mount is carried out, for tonal disturbances. It is shown that, despite the response time of the damper, the optimised mount gives very satisfactory performance. Then, to illustrate the interest of clipped continuous methods compared to clipped on-off ones, it is shown that performance at high frequency of clipped on-off methods are inevitably worse than clipped continuous ones. In particular, this control gives hardly better performance than a passive system (10% improvement). A variation of this strategy using a switch above a force threshold could enhance its performance. Finally, one investigates the performance of SA control for broadband vibration, which is a controversial subject. It is clearly shown that the deterioration of performance generally observed for broadband disturbances (compared to narrowband disturbances) is not due to the way SA control inherently operates, but to the various time delays present in controllable damping devices. In other words, this deterioration is not due to the control itself but to the actuation technology, which is perfectible. To confirm the interest of the chosen SA control strategy emphasized by the simulation results, an experimental implementa-

tion of the clipped continuous strategy with a force feedback loop has been performed. The results are presented in the next chapter.

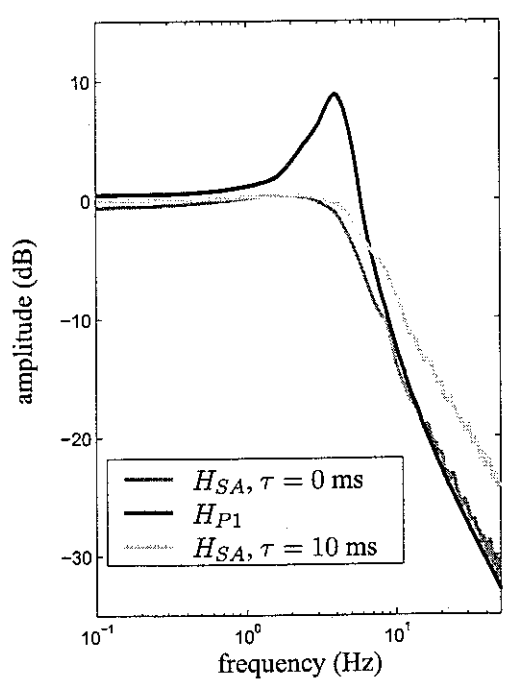

(a) Transmissibilities.

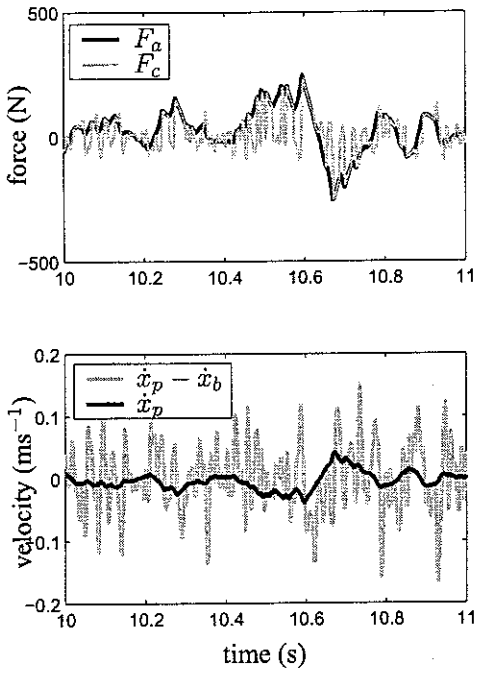

(b) Time response, $\tau = 0$ ms.

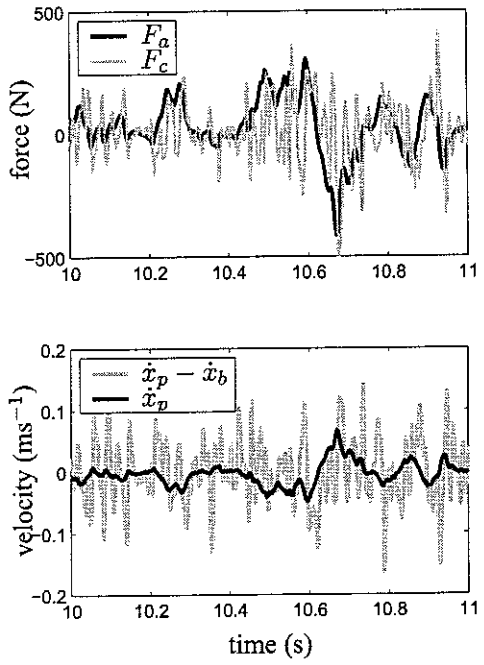

(c) Time response, $\tau = 10$ ms.

Figure 3.21: Isolation performance for white-noise broadband vibration - Simulation results.

CHAPTER 4 SINGLE AXIS ISOLATION EXPERIMENT

4.1 Test rig

The experimental rig is shown and described in Figure 4.1(a). The main features of this setup are the following: natural frequency of the mount, $f_n = 4.1$ Hz, minimum damping ratio, $\xi_{min} = 0.14$ (at $i_c = 0$ A), maximum damping ratio, $\xi_{max} = 1.5$ (at $i_c = 1.7$ A).

In this experiment, the base motion is imposed by an hydraulic jack, whose transfer function (displacement/input voltage) is a first order low-pass filter. In the results reported here, the input voltage was band limited white noise in the range 0.05-50 Hz. The resulting base motion spectra (displacement, velocity, acceleration) are shown in Figure 4.1(b). We can see that the base velocity spectrum contains mainly high frequency components, in the range 10-50 Hz, which is detrimental to the control performance. It is therefore a test case, which demonstrates the effect of time delay on SAVI performance for broadband disturbances. Note however that we could regret that this disturbance is different from the simulations (white noise velocity in the band 0.05-50 Hz). Further experimental investigations for this excitation and several other ones would be worthwhile, to get more general conclusions.

4.2 Isolation performance for narrowband disturbances

The results are not reported here, for brevity. But the SA control performed very well for tonal excitations, in same order than that found in the simulations of explicit clipped continuous SDC, with an idealised damper model. In particular, the SA controller was able to attenuate highly the sinusoidal excitations with frequencies around the suspension frequency, while providing the minimum damping for high frequency sinusoidal excitations.

4.3 Isolation performance for broadband disturbances

The isolation performance can be analysed in term of either auto-power spectrum ($S_x = S_{xx}$, Figure 4.2(a)), or transmissibility ($H_{xy} = S_{yx}/S_{xx}$, Figure 4.2(b)), or RMS amplitude (Figure 4.2(c)). The SAVI performance is compared to the PVI performance. Concerning SAVI, the force feedback gain is maintained at $K_p = 0.11$ while various skyhook gains are selected: $\xi_{sky} = [0,\ 0.73,\ 1,\ 1.1,\ 1.25,\ 1.75]$. Among these values, the subscript $_{SA}$ denotes the case $\xi_{sky} = 1.1$. Concerning PVI, several values of constant currents are selected: $i_c = [0,\ 0.1,\ 0.2,\ 0.3,\ 0.5,\ 1.7]$ amps. Among these values, the subscripts $_{P1}$ and $_{P2}$ denotes respectively the cases $i_c = 0$ amp ($\xi = 0.14$) and $i_c = 0.3$ amp ($\xi = 0.7$).

In Figures 4.2(a) and 4.2(b), we see that the isolator with control is able to provide quite good isolation at high frequency, while damping the level of vibration around the resonance, contrary to the passive cases. The trade-off in damping (or damping conflict) of PVI appears clearly. This trade-off is barely evident for SAVI with the controller considered. A common performance criterion in VI is a balance between the RMS acceleration and the RMS deflection of the suspension, see [27] and [36], though, in our study, this criterion is not so relevant (sufficient clearance space). On the other hand, a resonance of the isolator is not desirable because it could be observed by nearby accelerometers, which are being used for attitude control of the transportation system. As a consequence, we define the following performance criterion

$$J = \ddot{x}^{rms}_{p,\Delta f_2} + \rho\, \ddot{x}^{rms}_{p,\Delta f_1} \tag{4.1}$$

Each term of the weighting represents the RMS vibration level in a specified frequency range Δf. In this study, we choose $\Delta f_1 = 0 - 5.8$ Hz (the resonant region, since $f_n\sqrt{2} = 5.8$ Hz) and $\Delta f_2 = 0 - 50$ Hz (the range of isolation). f_n is fixed, ρ depends on ξ in PVI and on (ξ_{sky}, K_p) in SAVI. The levels of vibration resulting from the various aforementioned passive and semi-active cases are plotted in Figure 4.2(c), in a so-called conflict curve. Again, we see that SAVI is subject to the damping conflict much less than PVI. The isolation performance for the case ($\xi_{sky} = 1.25,\ K_p = 0.11$) is -20 dB in Δf_2 with only +1dB in Δf_1, which is better than any passive system.

Although the isolation performance of SAVI with this controller is quite satisfactory, the

transmissibility (Figure 4.2(b)) is less good than for tonal disturbances. In the latter case, the transmissibility of the SAVI system is very close to the passive-off system for frequencies above $f_n\sqrt{2}$, without any amplification below $f_n\sqrt{2}$. This deterioration in performance from narrowband to broadband disturbance is in agreement with the simulation results reported in the previous section.

4.4 Summary

The experimental results confirm that the implementation of an SA mount improves significantly the performance of a passive mount, for narrowband as well as for a certain type of broadband disturbance. From a performance index defined by a weighting between the level of vibration around resonance and the level of vibration at high frequency, we can conclude that, for the broadband disturbance studied here, SA isolation is not subject to the damping conflict, despite the hardware limitations (especially the time delays), contrary to passive isolation. This constitutes a major advantage for SA isolation and fully justifies the cost of complexity induced by an SA mount, compared to a passive solution. It would be interesting however to extend the investigation on broadband SA isolation, by studying various types of broadband disturbances. Moreover, it is imperative to check that the same trend occurs for launch excitations (coloured noise).

In the single degree of freedom configuration, SA isolation performs significantly better than passive isolation. This study has to be extended to multiple degrees of freedom systems. The next chapter presents some preliminary results on a single axis multiple dof system.

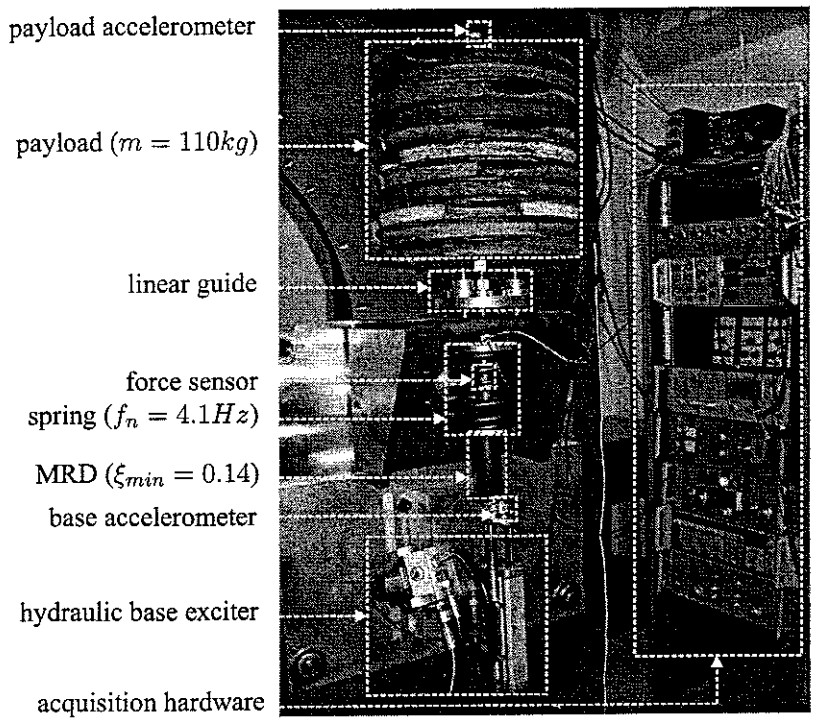

(a) Experimental rig.

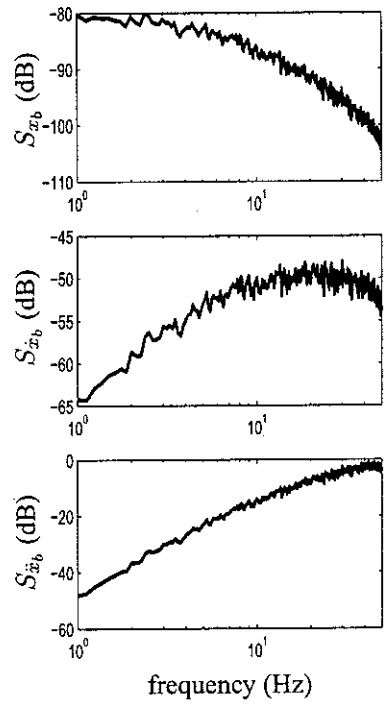

(b) Base auto-power spectra (displacement, velocity, acceleration).

Figure 4.1: Experimental implementation of semi-active isolation.

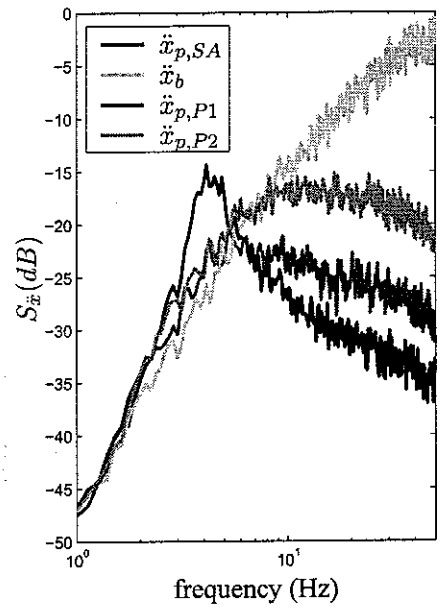

(a) Base and payload accelerations auto-power spectra.

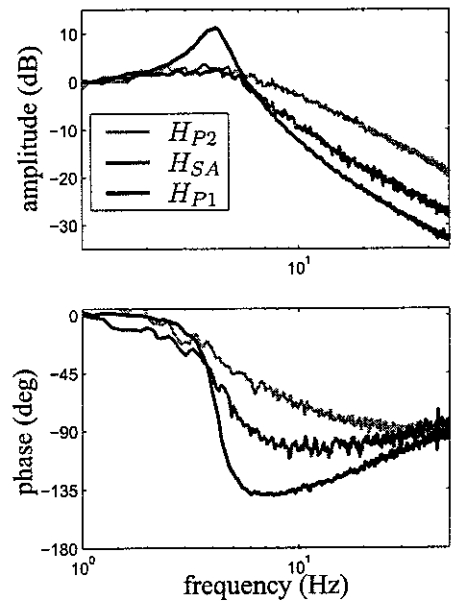

(b) Transmissibilities.

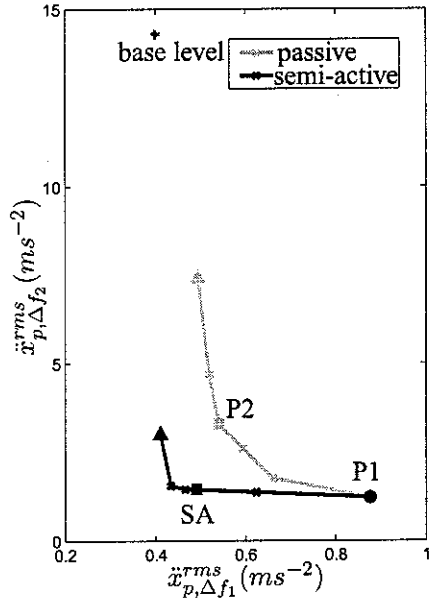

(c) Conflict curves. triangles : set-point high; • : set-point low.

Figure 4.2: Comparison between PVI and SAVI for broadband excitation. P1: passive, $\xi = 0.14$; P2: passive, $\xi = 0.7$; SA, $\xi_{sky} = 1$ - Experimental results.

CHAPTER 5 COUPLING OF A SINGLE DOF ISOLATION SYSTEM WITH A FLEXIBLE BASE AND A FLEXIBLE PAYLOAD

In section 1.1, we introduced the concept of vibration isolation with the single degree of freedom (dof) isolation system. In such a model, the payload and the base are supposed rigid. This model is idealised since in reality, most engineering structures are flexible. In particular, in the problem of attenuation of the transmission of launch vibration loads at the interface between the launcher and the payload, the rocket launcher is known to have a large number of modes in the frequency range of 5-100 Hz. As ARIANE 5 is a very flexible launcher, it has its first bending modes at as low as 1 Hz. The satellites mounted on the launcher may also have several modes in that bandwidth. For example, the European satellite Envisat has its first lateral (bending) mode at 8.1 Hz.

In a first approach, considering an uncoupled problem, i.e. considering the base and the payload as rigid, enables one to make a preliminary design of the isolation system, in term of mechanical dimensioning as well as controller design. Once this preliminary work has been carried out, it is necessary to verify that the isolation performance is not altered by coupling between the modes of the rocket launcher and the satellite, and the modes of the isolation mount.

To illustrate this problem of coupling, this preliminary study is focused on a single axis isolation system. The aim of this chapter is to study the system composed of the base, the isolator, and the payload, and to compare an uncoupled model of this system, where the base and the payload are rigid (Rigid Base and Rigid Payload: RBRP), as shown in figure 5.1(a), with a fully coupled model of the system, where the base and the payload are flexible (Flexible Base and Flexible Payload: FBFP), as shown in figure 5.1(b). However, to separate the different effects of base and payload, we investigate first separately a rigid base with a flexible payload (called RBFP, see section 5.2), and then a flexible base with a rigid payload (called FBRP, see section 5.3).

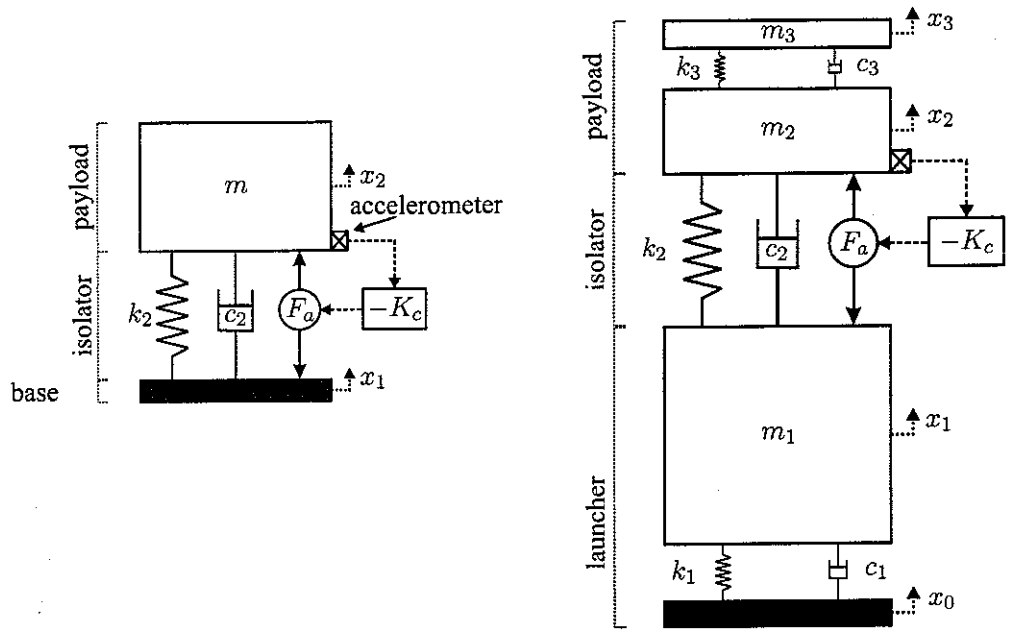

(a) Uncoupled model (RBRP)

(b) Fully coupled model (FBFP)

Figure 5.1: Two approaches of the single axis isolation system.

The isolation mount in the RBRP configuration considered here has a natural frequency of $f_n = 3$ Hz ($k_2 = m\omega_n$, $\omega_n = 2\pi f_n$), and both passive and active skyhook damper isolation are investigated. Refering to figure 5.1, a passive isolation system corresponds to the case where $F_a = 0$ (system in open-loop), whereas a purely active isolation system corresponds to the closed-loop system where $c_2 = 0$. The modes of the base and the payload have a damping ratio of 0.001, which is typical of lightly damped structures in space applications (use of carbon fibers composites and so on), and their natural frequencies are respectively chosen to be 5 Hz and 8 Hz respectively, i.e $\sqrt{k_1/m_1} = 2\pi 5$ and $\sqrt{k_2/m_2} = 2\pi 8$.

It is important to note that considering a realistic 6-dof isolation mount (or more if we consider internal modes such as strut modes), a finite element model of the launcher and the satellite would be necessary in a final stage of this study, and **could finally lead to different conclusions than those that are drawn in this chapter**. However, considering a single axis isolation system is helpful to understand the major concepts of vibration isolation of flexible systems.

5.1 The uncoupled model (RBRP) and the dimensioning

First of all, let us review some basic concepts inherent to the single dof isolation problem. In section 1.1, a single dof isolation system where the base and the payload are rigid was considered. Passive isolation (figure 1.1) as well as active skyhook damper (figure 1.4) isolation were introduced. In this chapter, the subscripts refering to the base and the payload are respectively "1" and "2".

By varying the damping ratio of the isolator mode, the inherent trade-off of passive isolation has been discussed. On the other hand, the well-known active skyhook damper control strategy avoids this trade-off by adding some active damping to the isolator mode, without altering the performance of isolation at high frequencies.

Thus, in order to attenuate vibration by 12 dB above 5 Hz, a suitable spring rate has to be chosen appropriately. For the active skyhook damper control strategy, with a feedback gain $c_{sky} = 2m\omega_n$ (critical damping), the active mount attenuates by 12 dB from a frequency above $f_{att} = 1.73\ f_n$. To achieve attenuation from 5 Hz upwards, the spring rate has to be such that the natural frequency of the isolator is at most 2.9 Hz. However, as shown in chapter 3, providing skyhook damping by a semi-active rather than active isolation system, f_{att} is greater than $1.73\ f_n$ by a small amount ($f_{att} = 2.33\ f_n$). Taking into account the considerations of chapter 3, a natural frequency of 2 Hz would be acceptable.

This concept of a compliant mount recalls an old idea in vibration isolation that was discussed by Den Hartog in [51]. Den Hartog answers his own question " ... how do we have to design the main spring [of an automobile] for maximum riding comfort... ?" with the answer, "the spring has to be made as soft as possible...". This assertion, which was related to passive suspension, is still valid if we consider active damping of a suspension system. It is worth to noting, however, that active isolation has other capabilities than damping, such as active softening (see [52] for example). Nevertheless, providing isolation by a compliant mount remains of great interest.

A major constraint in the lower bound of spring rate for isolation is the static deflection. As has already been stated, a natural frequency of 2 Hz would be optimal if we take into account the performance of semi-active control using MR dampers. However there is a major limitation because of the quasi-static acceleration (due to the thrust of the launcher) during the flight: the associated quasi-static deflection (which is mainly longitudinal,

along the thrust direction) may be too large. This defelection is given by

$$(x_2 - x_1)_{stat} = \frac{mG}{k} = \frac{G}{\omega_n^2} \tag{5.1}$$

where x_2 and x_1 are the payload and base axial displacements, m the payload mass, k the axial stiffness of the isolating mount, ω_n the axial natural frequency of the mount with the payload and G is the quasi-static acceleration. The maximal quasi-static acceleration is around $G = 4g_0$, where g_0 is the constant of gravity. It follows that

$$(x_2 - x_1)_{stat}^{max} \cong \frac{4g_0}{4\pi^2 f_n^2} \tag{5.2}$$

If $f_n = 2$ Hz, we obtain $(x_2 - x_1)_{stat}^{max} = 25$ cm, which is too large when we consider that the final isolator in the launcher has to be included in a volume that is not more than 50 cm high. As a consequence, a natural frequency of 3 Hz would be more reasonable, since it induces a deflection in the order of 10 cm. The MR damper stroke is theoretically unlimited, whereas it may be more difficult to design springs that accept such a deflection. This point will be considered further later.

5.2 Rigid Base Flexible Payload sytem (RBFP)

5.2.1 Definition of the model and formation of the equations

In order to see the influence of the payload mode on the isolator transmissibility, the uncoupled model of figure 5.2(a) and the coupled model of figure 5.2(b) are compared. The following parameters are used:

$$\begin{cases} m_2 + m_3 = m \\ m_3 = \mu_3 m_2 \\ \omega_2 = \omega_n \\ k_2 = k = m\omega_2^2 \\ c_2 = 2\xi_2 m\omega_2 \\ k_3 = m_3\omega_3^2 \\ c_3 = 2\xi_3 m\omega_3 \end{cases} \tag{5.3}$$

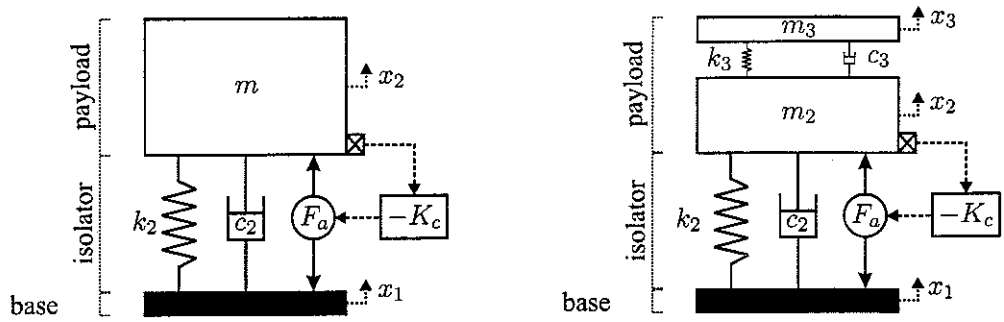

(a) Uncoupled model (RBRP)

(b) Coupled model with a flexible payload (RBFP)

Figure 5.2: Isolation system with a rigid base and a flexible payload.

where $\mu_3 = 0.3$. As already said, $\xi_3 = 0.001$, $f_3 = 8$ Hz, and $f_n = 3$ Hz. ξ_2 is chosen in this study to be arbitrarily 0.1 (which would correspond to an isolation system using a MR damper in its passive mode, at zero current).

In this chapter, we use state-space forms of the motion equations. We define the following notation convention:

- $\alpha_{i,j}$ an $i \times j$ matrix, each element of which equals α (usually $\alpha = 0$ or 1),
- $\alpha_k = \alpha_{k,k}$,
- I_k is the identity matrix of dimension k,
- ^{t} is the transposition operator.

In order to make the presentation more compact, we synthesize the two problems of passive and active isolation as a unique problem where the passive isolation problem is treated as the system in open-loop form ($F_a = 0$), whereas the active isolation is the problem in the closed-loop form. We consider the problem where $\xi_2 = 0.1$, even when it deals with active isolation. Refering to figure 5.2, this means that we do not consider the purely active isolation problem. However the following conclusions that are drawn remains valid for a purely active isolation problem. Moreover, this configuration is closer to the problem of semi-active isolation with MR dampers since these devices have residual damping at zero current (see chapter 3).

Defining the displacements $w_i = x_i - x_1$, $i = [2, 3]$, relative to the base displacement, and the vector of relative displacements $w = [w_2\ w_3]^t$, the equations of motion of the

system may be expressed as

$$M\ddot{w} + C\dot{w} + Kw = -M\mathbf{1}_{2,1}\ddot{x}_1 + \Lambda F_a \tag{5.4}$$

where $\Lambda = [1\ 0]^t$ gives the position of the actuator, and the mass, damping and stiffness matrices are, respectively,

$$M = \begin{bmatrix} m_2 & 0 \\ 0 & m_3 \end{bmatrix}, \quad C = \begin{bmatrix} c_2 + c_3 & -c_3 \\ -c_3 & c_3 \end{bmatrix}, \quad K = \begin{bmatrix} k_2 + k_3 & -k_3 \\ -k_3 & k_3 \end{bmatrix} \tag{5.5}$$

Defining the state vector as $x = [w\ \dot{w}]^t$, the output vector as $y = [\ddot{x}_2\ \ddot{x}_3]^t$, the controlled input as $u = F_a$ and the disturbance input as $\ddot{x}_1$, the state-space form of the equation of motion 5.4 is given by

$$\begin{aligned} \dot{x} &= Ax + Bu + E\ddot{x}_1 \\ y &= C_y x + Du + F\ddot{x}_1 \end{aligned}$$

$$A = \begin{bmatrix} \mathbf{0}_2 & I_2 \\ -M^{-1}K & -M^{-1}C \end{bmatrix}, \quad B = \begin{bmatrix} \mathbf{0}_{2,1} \\ M^{-1}\Lambda \end{bmatrix}, \quad E = \begin{bmatrix} \mathbf{0}_{2,1} \\ -\mathbf{1}_{2,1} \end{bmatrix} \tag{5.6}$$

$$C_y = \begin{bmatrix} -M^{-1}K & -M^{-1}C \end{bmatrix}, \quad D = \begin{bmatrix} M^{-1}\Lambda \end{bmatrix}, \quad F = \begin{bmatrix} \mathbf{0}_{2,1} \end{bmatrix}$$

The active control strategy considered in this chapter is the active skyhook damper control. The controlled output $\ddot{x}_2$ is fed back through a integrator and multiplied by a gain c_{sky}. Thus, the controller transfer function is $K_c = -\frac{c_{sky}}{s}$ (acceleration feedback). We define the active damping ratio as $\xi_{sky} = \frac{c_{sky}}{2m\omega_n}$, as in section 1.1.

The Laplace transform of equation 5.6 enables one to derive the transfer matrix between inputs and outputs, expressed as

$$\begin{aligned} & Y(s) = G(s)\,U(s) \\ \text{with} \quad & G(s) = C_y(sI - A)^{-1}E + D_y \end{aligned} \tag{5.7}$$

which in our case is a (2,2) matrix. We are interested in particular in the two following

tranfer functions:

- between the disturbance input $\ddot{x}_1$ and the ouput $\ddot{x}_2$, (payload base), which is the transmissibility of the isolator,
- between the disturbance input $\ddot{x}_1$ and the ouput $\ddot{x}_3$, which represents the response of the payload mode.

Defining G_{ij} as the transfer function between $\ddot{x}_i$ and $\ddot{x}_j$, the two above transfer functions are

$$\begin{bmatrix} G_{21}(s) \\ G_{31}(s) \end{bmatrix} = \begin{bmatrix} \frac{N_{21}(s)}{D(s)} \\ \frac{N_{31}(s)}{D(s)} \end{bmatrix} \tag{5.8}$$

Note that they have a common denominator $D(s)$, so they have the same poles. The formula 5.7 enables one to compute the frfs easily, but it becomes more difficult to derive the transfer functions when the number of dofs increases. Here, for the passive case, the analytical transfer functions have been found directly from the equations of motion. In the case of the open-loop system (passive isolation), the numerators and the denominator are

$$\begin{gathered} N_{21}^{OL}(s) = \left(2\xi_2\omega_2 s + \omega_2^2\right)\left(s^2 + 2\xi_3\omega_3 s + \omega_3^2\right) \\ N_{31}^{OL}(s) = \left(2\xi_2\omega_2 s + \omega_2^2\right)\left(2\xi_3\omega_3 s + \omega_3^2\right) \\ D^{OL}(s) = \left(s^2 + \left(2\xi_2\omega_2 + 2\mu_3\xi_3\omega_3\right)s + \left(\omega_2^2 + \mu_3\omega_3^2\right)\right)\left(s^2 + 2\xi_3\omega_3 s + \omega_3^2\right) \\ -\mu_3\left(2\xi_3\omega_3 s + \omega_3^2\right)^2 \end{gathered} \tag{5.9}$$

5.2.2 Comparison between the uncoupled and the coupled models

To compare the uncoupled and the coupled models, and investigate whether the isolation performance is deteriorated by any coupling between the isolator mode and the payload mode, we can compare the isolation transmissibility (G_{21}) and the payload response (G_{31}).

5.2.2.1 Comparison of isolation transmissibility

Here we focus on the transmissibility of the isolator in both open-loop (passive isolation) and closed-loop (active isolation) forms, comparing the cases of:

- the uncoupled model: isolator with a rigid payload, as a reference case that was studied in 1.1. The passive transmissibility is denoted by H^p_{ref} and the active transmissibility is denoted by H^a_{ref},
- the coupled model: isolator with a flexible payload. The passive isolator transmissibility is denoted by G^{OL}_{21} (defined analytically in equation 5.9) and the active isolator transmissibility is denoted by G^{CL}_{21}.

where the reference transmissibilities are (see section 1.1)

$$\begin{cases} H^p_{ref} = \dfrac{\frac{2\xi_2}{\omega_2}s+1}{\frac{s^2}{\omega_2^2}+\frac{2\xi_2}{\omega_2}s+1} \\ H^a_{ref} = \dfrac{\frac{2\xi_2}{\omega_2}s+1}{\frac{s^2}{\omega_2^2}+\frac{2\left(\xi_{sky}+\xi_2\right)}{\omega_2}s+1} \end{cases} \tag{5.10}$$

The Bode diagrams of the different transfer functions and their pole-zero locations are shown in figure 5.3.

In figures 5.3(a) and 5.3(b), we can see that the isolator transmissibility is substantially modified around the frequency of the mode of the payload. In particular, the apparition of an antiresonance at 8 Hz followed by a mode at a slightly higher frequency (9.3 Hz for the passive isolation, and 8.6 Hz for active isolation) is clear. The features of G^{OL}_{21} and G^{CL}_{21} are described below:

- The antiresonance is visible on the pole-zero map by two complex conjugate zeros. As described in [37], the antiresonance frequencies corresponds to the frequencies of the modes of the system where the output is constrained (fixed dof). An antiresonance means indeed that whatever the amplitude of the input at that particular frequency, the amplitude of the ouput is zero (or close to zero). In our case, constraining the ouput $\ddot{x}_2$ leads to an antiresonance at the frequency of the payload mode, the payload being clamped at its base, that is to say at ω_3, which can be verified by the frfs of G^{OL}_{21} and G^{CL}_{21} ($f_3 = 8$ Hz), and analytically in N^{OL}_{21}, cf equation 5.9. The phase changes by 180 deg at the antiresonance.
- The second mode of G^{OL}_{21} appears at 9.3 Hz. The associated complex conjugate poles are very close to the pair of zeros. Note that their relative position is determined by the mass ratio μ_3. Concerning G^{CL}_{21}, it is worth to noting that for $\xi_{sky} = 1$,

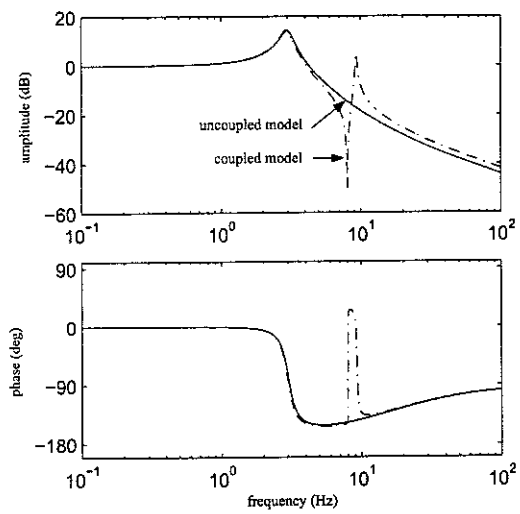

(a) Passive isolation transmissibility (open-loop): (-) H^p_{ref}, (dash-dot) G^{OL}_{21}

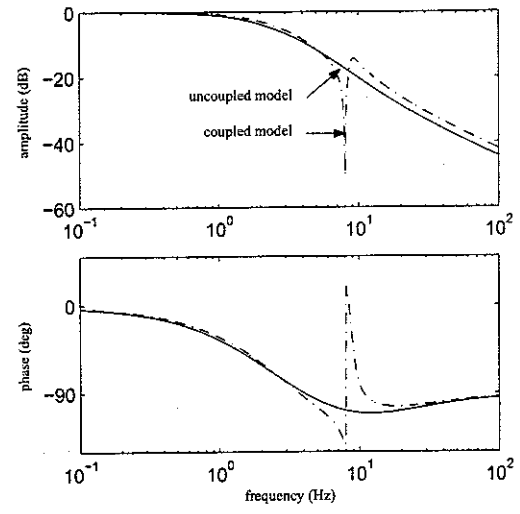

(b) Active isolation transmissibility (closed-loop), (-) H^a_{ref}, (dash-dot) G^{CL}_{21}

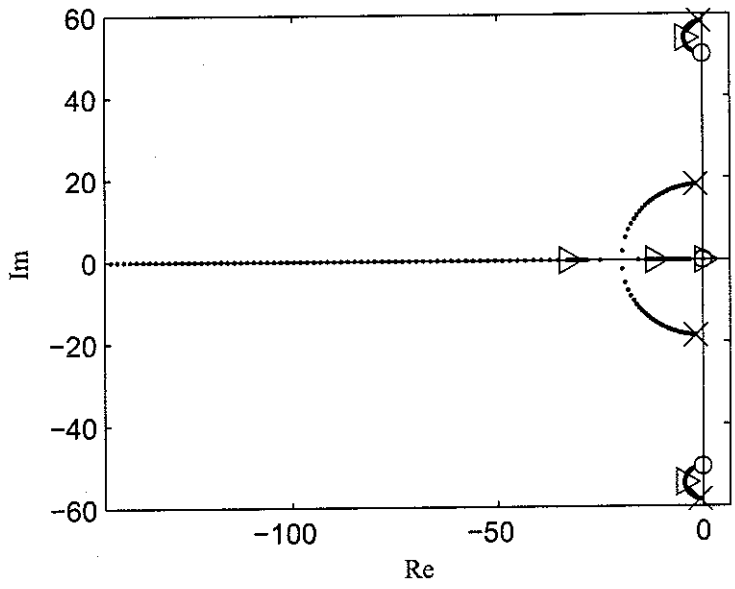

(c) Root locus

Figure 5.3: Comparison between the coupled model and the uncoupled model. The root locus corresponds to a feedback gain range such that $\xi_{sky} = 0.001$ to 3. ($\times$ and o): open-loop poles and zeros. ($\triangleright$): closed-loop poles for $\xi_{sky} = 1$.

the damping of the second mode is maximized since the associated poles (triangles) are on the left part of the circle of the root locus. We can see on the Bode diagram that this mode is much more damped with active isolation than with passive isolation. This means that the actuator has some control authority on the payload mode in the RBFP case, which is not the case in the FBRP configuration (see next section).

- The other pair of poles correspond to the suspension mode. Concerning G_{21}^{OL}, this mode is nearly the same as that for the coupled model. As regards G_{21}^{CL}, the associated real poles (equal in RBRP with $\xi_{sky} = 1$, at the intersection of the half-circle and the real axis) move slightly on the left and right (triangles on the real axis). As a result, the mode becomes slightly overdamped. To have critical damping, the feedback gain should be changed such that $\xi_{sky} = 0.885$.

- A real zero far from the imaginary axis is present ($z_3 = -\omega_2/(2\xi_2)$), see equation 5.9). On the Bode diagram, it is visible (not represented here) at very high frequencies with a change of +20 dB/dec of the roll-off slope and of +90 deg of the phase. Finally, a zero equal to zero appears due to the pure integrator in the feedback loop.

As regards the passive isolation, it can be concluded that the main change in G_{21}^{OL} that could be important in a passive isolation system is that the transmissibility of the isolator is nearly equal to 0 dB at 9.3 Hz, which means no isolation. However, if we consider that the mode of the payload is changed from 8 to 9.3 Hz, we can consider that its level is substantially decreased and that the isolation system plays its role. This is verified in the next part (comparison of G_{31}^{OL}).

5.2.2.2 Comparison of the payload response

Here we focus on the response of the payload, in both open-loop (passive isolation) and closed-loop (active isolation) forms, comparing the cases of:

- the uncoupled model. The responses of the payload with passive and active isolation are respectively H_{payl}^{p} and H_{payl}^{a},

- the coupled model. The responses of the payload with passive and active isolation are G_{31}^{OL} (equation 5.9) and G_{31}^{CL}.

H^p_{payl} and H^a_{payl} are obtained by multiplying the payload transfer function and the transfer functions of the passive and active isolators (defined in 5.10)

$$\begin{cases} H^p_{payl} = H_{payl} * H^p_{ref} \\ H^a_{payl} = H_{payl} * H^a_{ref} \\ \text{with } H_{payl} = \frac{\frac{2\xi_3}{\omega_3}s+1}{\frac{s^2}{\omega_3^2}+\frac{2\xi_3}{\omega_3}s+1} \end{cases} \tag{5.11}$$

Again, there are some notable differences between the uncoupled and the coupled model. In particular, as regards active isolation, if we compare the 2 frfs without and with the isolator, we can see in figure 5.4(b) that, for the coupled model, the peak response of the payload mode is decreased by 57 dB (antiresonance + shifted payload mode effect), whereas the uncoupled model predicts an attenuation of 18 dB only around 8 Hz. We might conclude that, not only does the skyhook damper control with $f_n = 3$ Hz attenuate vibrations above $3 * 1.73 = 5.19$ Hz of at least 12 dB, but also provides much more attenuation at the frequencies of the modes of the payload[1]? This type of conclusion is to be taken cautiously, however, because we deal here with a very simple model. A real system would probably behave differently. However, according to [37], it is assured that there is alternance between poles and zeros if frequencies of the payload modes are higher than that of the isolation system. This alternance is the cause of the improved efficiency of the control aforementioned. It would be interesting to see if this effect occur in a more realistic system.

5.3 Flexible Base Rigid Payload sytem (FBRP)

In this section, we carry out the same type of study as in the previous section, considering now a flexible base, due to a launcher mode, and a rigid payload.

[1] at least of the modes that the actuator has a control authority on, which could be due to the fact these modes are observable/controllable at the interface between the isolator and the payload

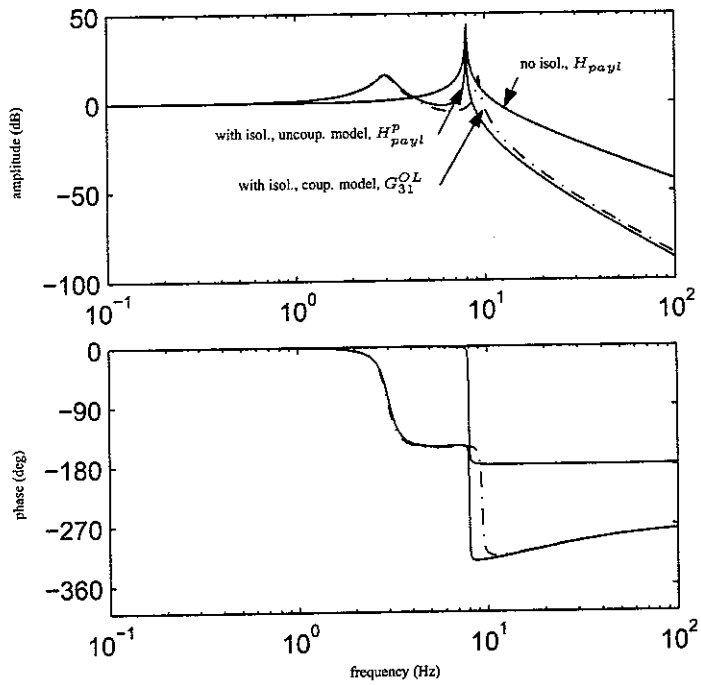

(a) Passive isolation (open-loop)

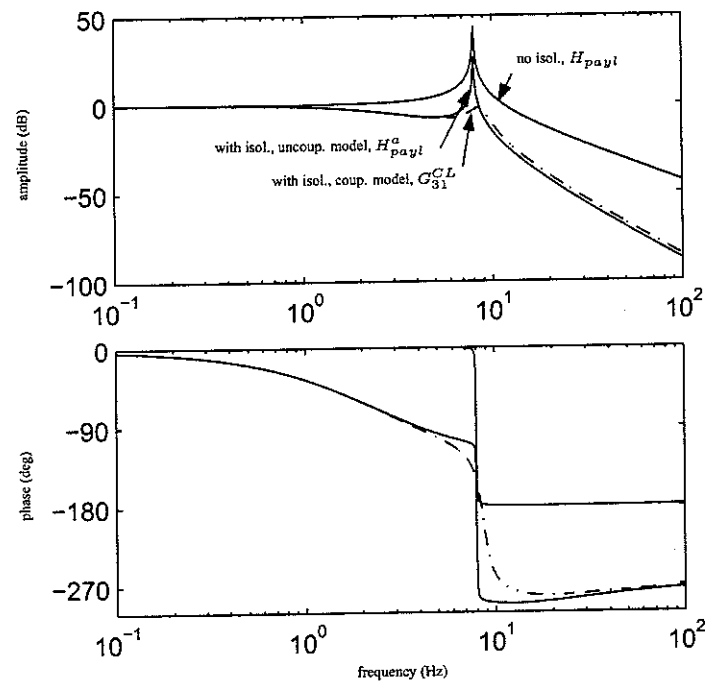

(b) Active isolation (closed-loop)

Figure 5.4: Comparison of the payload response with and without isolation, according to the coupled model and the uncoupled model in the RBFP case. The isolation performance is increased due to coupling effects.

5.3.1 Definition of the model and formation of the equations

In order to see the influence of the launcher mode on the isolator transmissibility, the uncoupled model of figure 5.5(a) and the coupled model of figure 5.5(b) are compared. The following parameters are used

$$\begin{cases} m_1 = \mu_1 m \\ \omega_2 = \omega_n \\ k_2 = k = m\omega_2^2 \\ c_2 = 2\xi_2 m\omega_2 \\ k_1 = m_1\omega_1^2 \\ c_1 = 2\xi_1 m_1\omega_1 \end{cases} \tag{5.12}$$

recalling that with the uncoupled model, a mount stiffness k has been chosen such that $\omega_n^2 = \frac{k}{m}$, where m is the payload mass. Here $\mu_1 = 10$: the base is much more massive than the payload. This assumption is reasonable in the launcher configuration (ARIANE 5 has a mass of around 500 tons, the satellites are typically of several tons). As already said, $\xi_1 = 0.001$[2], $f_1 = 5$ Hz, and $f_n = 3$ Hz.

Defining the displacements $w_i = x_i - x_1$, $i = [1, 2]$, relative to the base displacement, and the vector of relative displacements $w = [w_1\ w_2]^t$, the equations of motion of the system may be expressed as

$$M\ddot{w} + C\dot{w} + Kw = -M\mathbf{1}_{2,1}\ddot{x}_0 + \Lambda F_a \tag{5.13}$$

where $\Lambda = [-1\ 1]^t$ gives the position of the actuator, and the mass, damping and stiffness matrices are, respectively,

$$M = \begin{bmatrix} m_1 & 0 \\ 0 & m \end{bmatrix}, \qquad C = \begin{bmatrix} c_1 + c_2 & -c_2 \\ -c_2 & c_2 \end{bmatrix}, \qquad K = \begin{bmatrix} k_1 + k_2 & -k_2 \\ -k_2 & k_2 \end{bmatrix} \tag{5.14}$$

Defining the state vector as $x = [w\ \dot{w}]^t$, the output vector as $y = [\ddot{x}_1\ \ddot{x}_2]^t$, the controlled input as $u = F_a$ and the disturbance input as $\ddot{x}_0$, the state-space form of the equation of

[2]note that ARIANE 5 contains many dissipative elements, the damping of some modes may be higher than 0.001

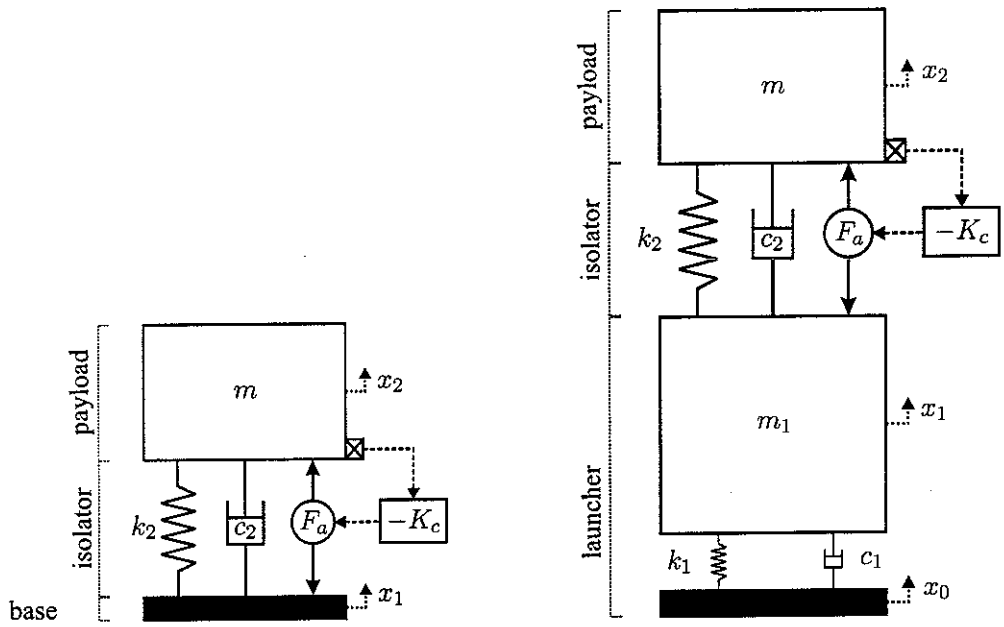

(a) Uncoupled model (RBRP)

(b) Coupled model with a flexible base (FBRP)

Figure 5.5: Isolation system with a flexible base and a rigid payload.

motion 5.13 is given by

$$\dot{x} = Ax + Bu + E\ddot{x}_1$$
$$y = C_y x + Du + F\ddot{x}_1$$

where

$$A = \begin{bmatrix} \mathbf{0}_2 & I_2 \\ -M^{-1}K & -M^{-1}C \end{bmatrix}, \quad B = \begin{bmatrix} \mathbf{0}_{2,1} \\ M^{-1}\Lambda \end{bmatrix}, \quad E = \begin{bmatrix} \mathbf{0}_{2,1} \\ -\mathbf{1}_{2,1} \end{bmatrix} \tag{5.15}$$

$$C_y = \begin{bmatrix} -M^{-1}K & -M^{-1}C \end{bmatrix}, \quad D = \begin{bmatrix} M^{-1}\Lambda \end{bmatrix}, \quad F = \begin{bmatrix} \mathbf{0}_{2,1} \end{bmatrix}$$

Again, we define G_{ij} as the transfer function between $\ddot{x}_i$ and $\ddot{x}_j$. Here the isolator transmissibility G_{21} can not be derived from the state-space form because both $\ddot{x}_1$ and $\ddot{x}_2$ are inputs. As a consequence, we find G_{21} as

$$G_{21} = \frac{G_{20}}{G_{10}} \tag{5.16}$$

where G_{20} and G_{10} are computed numerically from the state-space model according to the formula 5.7.

5.3.2 Comparison between the uncoupled and the coupled models

To compare the uncoupled and the coupled models, and investigate whether the isolation performance is not deteriorated by any coupling between the isolator mode and the launcher mode, we can compare the isolation transmissibility (G_{21}) and the payload response (G_{20}). On the other hand, the base mode may be analysed with and without the isolator in order to see if the introduction of an isolation system disturbs the base mode, which could be a sign of a potential risk of disturbance of the launcher[3].

5.3.2.1 Comparison of isolation transmissibility

The isolator transmissibilities (passive and active) for RBRP (equation 5.10) and for FBRP (equation 5.16) are identical: a flexible mode of the base does not change the isolation transmissibility. This can be explained for the passive case as follows. Let us consider the expressions 5.9 stated for the RBFP configuration. In the passive case, the RBFP and FBRP configurations are equivalent (2 dof systems) by replacing the subscripts 3, 2, 1 by respectively 2, 1, 0 in 5.9 and the expression of G_{21} can be derived as

$$\begin{aligned} G_{21} = \frac{G_{20}}{G_{10}} &= \frac{N_{20}}{D}\frac{D}{N_{10}} = \frac{N_{20}}{N_{10}} \\ &= \frac{\left(2\xi_1\omega_1 s+\omega_1^2\right)\left(2\xi_2\omega_2 s+\omega_2^2\right)}{\left(2\xi_1\omega_1 s+\omega_1^2\right)\left(s^2+2\xi_2\omega_2 s+\omega_2^2\right)} \\ &= \frac{2\xi_2\omega_2 s+\omega_2^2}{s^2+2\xi_2\omega_2 s+\omega_2^2} \end{aligned} \tag{5.17}$$

which is indeed the passive reference transmissibility (RBRP).

Thus the isolator transmissibility for the FBRP case is the same as that for the RBRP case. This is not the case for RBFP, as seen in the previous section. In fact, the explanation is obvious: for FBRP, by definition of transmissibility between x_2 and x_1, the motion of x_1 is imposed. The presence of a mode associated to x_1 has no effect on this imposed motion. On the contrary, for RBFP, the fact to impose the motion of x_1 does not impose any restriction to the masses m_2 and m_3 to resonate.

With the same sort of argument, we can think that the frf of G_{20} has two modes (isolator

[3] what might be particularly critical is that the accelerometers used in the control loop of trajectory of the launcher are located under the payload attach fitting (at the moment, a rigid conical structure, which would be replaced by an isolation system). As a consequence, the introduction of low frequency modes due to the isolator could disturb the trajectory control.

and base) and possibly some coupling effects of the two modes. This is verified in the following paragraph.

5.3.2.2 Comparison of payload response

Figure 5.6 shows the payload response G_{20} obtained by the coupled and uncoupled models, for both passive and active isolation. The results of the coupled and uncoupled models are very similar except at the vicinity of the modes where there are some slight differences. Again, these differences are due to the appearance of two antiresonances or two pairs of poles that can be seen in the pole-zero diagram 5.6(c). In figure 5.6(b), the uncoupled model predicts an attenuation of 12 dB at 5 Hz whereas the coupled model gives an attenuation of 34 dB.

Finally, we can notice that the loop of the second mode in the root locus 5.6(c) is much smaller than in the RBFP configuration. This is due to the difference of mass ratios in the two cases ($\mu_3 = 0.3$ whereas $\mu_2 = 10$). The mass involved in the base mode is much larger. As a consequence, the control authority (active damping) of the actuator is inferior than in the RBFP case.

5.4 Flexible Base Flexible Payload system (FBFP)

Let us consider finally the fully coupled analysis taking into account the structural response of both base and payload. The uncoupled model of figure 5.7(a) and the coupled model of figure 5.7(b) are compared. The default used parameters are those in the two previous sections.

5.4.1 Definition of the model and formation of the equations

Defining the displacements $w_i = x_i - x_1$, $i = [1, 2, 3]$, relative to the base displacement, and the vector of relative displacements $w = [w_1\ w_2\ w_2]^t$, the equations of motion of the system may be expressed as

$$M\ddot{w} + C\dot{w} + Kw = -M\mathbf{1}_{2,1}\ddot{x}_0 + \Lambda F_a \tag{5.18}$$

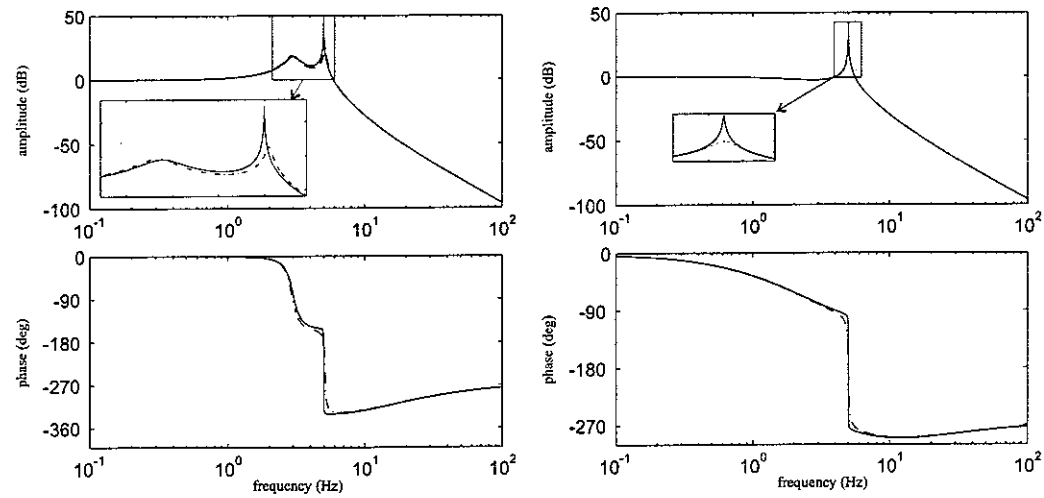

(a) Passive isolation (open-loop), (-) uncoupled, (dash-dot) coupled model.

(b) Active isolation (closed-loop), (-) uncoupled, (dash-dot) coupled model.

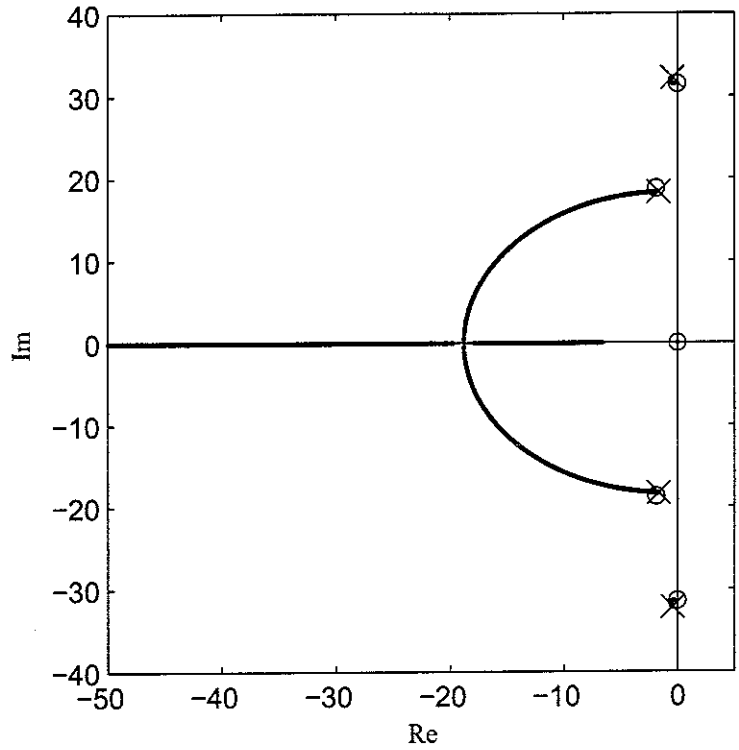

(c) Root locus

Figure 5.6: Comparison between the coupled model (-.) and the uncoupled (-) model. The root locus corresponds to a feedback gain range such that $\xi_{sky} = 0.001$ to 1.5. ($\times$ and o): open-loop poles and zeros.

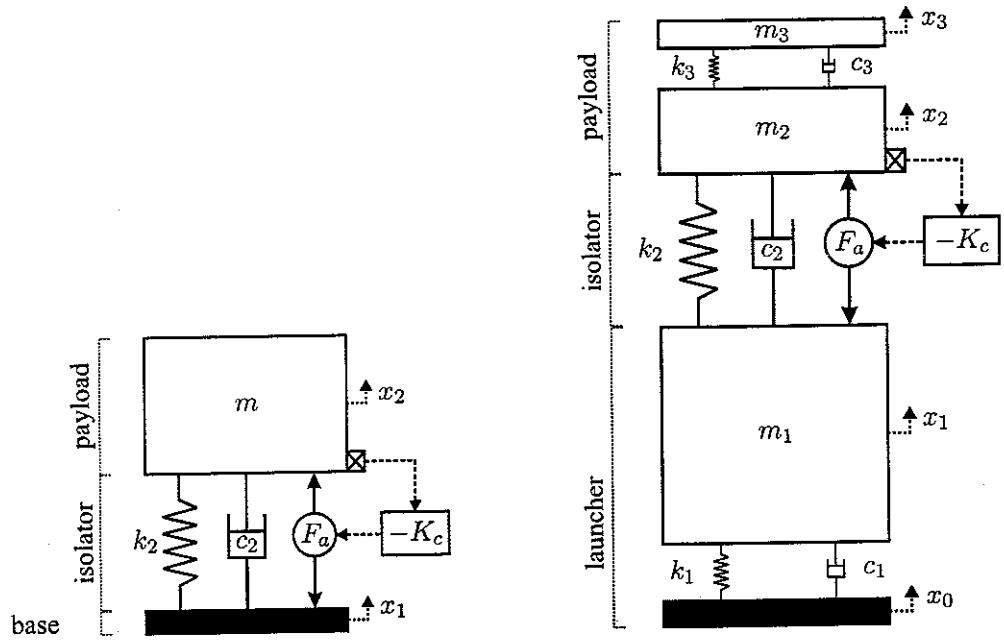

(a) Uncoupled model (RBRP)

(b) Fully coupled model (FBFP)

Figure 5.7: Isolation system with a flexible base and a flexible payload.

where $\Lambda = [-1\ 1\ 0]^t$ gives the position of the actuator, and the mass, damping and stiffness matrices are, respectively,

$$M = \begin{bmatrix} m_1 & 0 & 0 \\ 0 & m2 & 0 \\ 0 & 0 & m3 \end{bmatrix}, \quad C = \begin{bmatrix} c_1 + c_2 & -c_2 & 0 \\ -c_2 & c_2 + c_3 & -c_3 \\ 0 & -c_3 & c_3 \end{bmatrix}, \tag{5.19}$$

$$K = \begin{bmatrix} k_1 + k_2 & -k_2 & 0 \\ -k_2 & k_2 + k_3 & -k_3 \\ 0 & -k_3 & k_3 \end{bmatrix}$$

Defining the state vector as $x = [w\ \dot{w}]^t$, the output vector as $y = [\ddot{x}_1\ \ddot{x}_2\ \ddot{x}_2]^t$, the controlled input as $u = F_a$ and the disturbance input as $\ddot{x}_0$, the state-space form of the equation of

motion 5.13 is given by

$$\dot{x} = Ax + Bu + E\ddot{x}_1$$
$$y = C_y x + Du + F\ddot{x}_1$$

$$A = \begin{bmatrix} 0_3 & I_3 \\ -M^{-1}K & -M^{-1}C \end{bmatrix}, \quad B = \begin{bmatrix} 0_{3,1} \\ M^{-1}\Lambda \end{bmatrix}, \quad E = \begin{bmatrix} 0_{3,1} \\ -1_{3,1} \end{bmatrix} \tag{5.20}$$

$$C_y = \begin{bmatrix} -M^{-1}K & -M^{-1}C \end{bmatrix}, \quad D = \begin{bmatrix} M^{-1}\Lambda \end{bmatrix}, \quad F = \begin{bmatrix} 0_{3,1} \end{bmatrix}$$

Again, we define G_{ij} as the transfer function between $\ddot{x}_i$ and $\ddot{x}_j$ and derive the isolator transmissibility G_{21} as in equation 5.16.

5.4.2 Comparison between the uncoupled and the coupled models

The difference between the frfs obtained from the uncoupled and the coupled models are very similar to those described in the two previous sections. The effects occuring in the problem of FBFP are just the addition of the effects of RBFP and FBRP problems. In particular, it is observed that the isolator transmissibility is not affected by the addition of a base mode whereas it is by the addition of a payload mode. In figure 5.8, we can see the three loops corresponding to the three modes associated to the base, isolator and payload.

5.4.3 Comparison with and without isolation

In figure 5.9, the frfs of G_{30} with both passive and active isolation are shown, and compared with the case without isolation. The case without isolation is simulated by stiffening the interface between the base and the payload (i.e. stiffening the isolator) such that the features of the isolator become[4]: $f_2 = 30$ Hz and $\xi_2 = 0.001$.

Again, we can remark in figure 5.9(b) that the actuator has more control authority on the payload mode (48 dB of attenuation) than on the base mode (34 dB of attenuation) because of the mass ratios. It is again remarkable that those attenuations are more important due

[4]the current interface in the launcher is a stiff payload attach fitting in fiber carbon with an axial natural frequency of 30 Hz

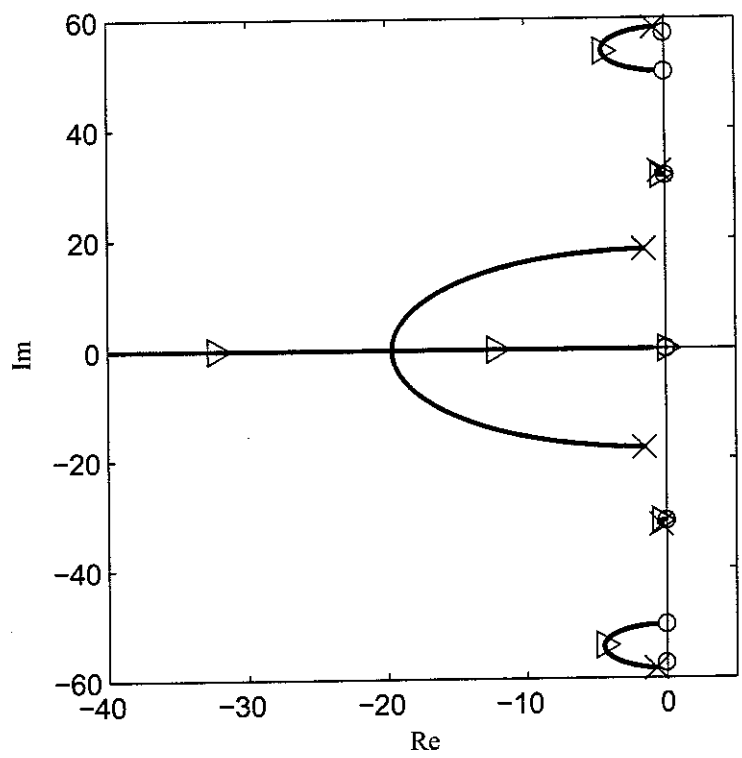

Figure 5.8: Root locus for a feedback gain range such that $\xi_{sky} = 0.001$ to 10. ($\times$ and o): open-loop poles and zeros. ($\triangleright$): closed-loop poles for $\xi_{sky} = 1$.

to coupling effects than what is predicted with a uncoupled model: 34 dB instead of 12 dB at 5 Hz and 48 dB instead of 17.6 dB at 8 Hz.

The response of the base dof (G_{10}) may be quite interesting as well. Its frfs in both passive and active isolation configurations are shown in figure 5.10. We see that the resonance associated to the launcher/payload interface does not appear clearly for an isolating (soft) interface contrary to the case where the interface is stiff. Moreover, we clearly see the ability of the isolation system to decouple the base and the payload structural responses: for an isolating interface, the payload resonance does not appear in the frf of G_{10}.

To further illustrate this decoupling effect, the frfs of G_{30} and G_{10}, without and with active isolation, in a case where the base and the payload have coincident natural frequencies at 8 Hz, which is a case of maximal coupling effects when there is no isolation, are shown in figure 5.11. In the case where there is no isolation, the two coincident modes are changed and their resonance appear on both sides of 8 Hz, which is a typical coupling effect. By inserting an active isolation system at the interface of the base and the payload, this effect is cancelled and each structure recovers its original properties. This decoupling effect is one of the objectives of an isolation system in the launcher. With such a function, the studies of coupling between the launcher and the payload structures that are currently carried out before each flight[5] might be avoided, thus enabling the launcher operator to reduce its costs and time delays.

5.5 Summary

This chapter has dealt with the question of coupling effects between a flexible base, a soft isolation system and a flexible payload. This problem may be of crucial importance. Actually, in a first approach, the design of a passive, active or semi-active isolation system is carried out with the assumption that the base and the payload are rigid, which is called the uncoupled model of the system. This assumption is very helpful to determine a starting point for subsequent work: the mechanical configuration of the isolating structure as well as the primary function and so the primary structure of the controller. In this study, the concept of a soft semi-active isolation system (and in a first analysis of a soft active

[5]because each satellite and even nearly each launcher have different properties from one flight to another

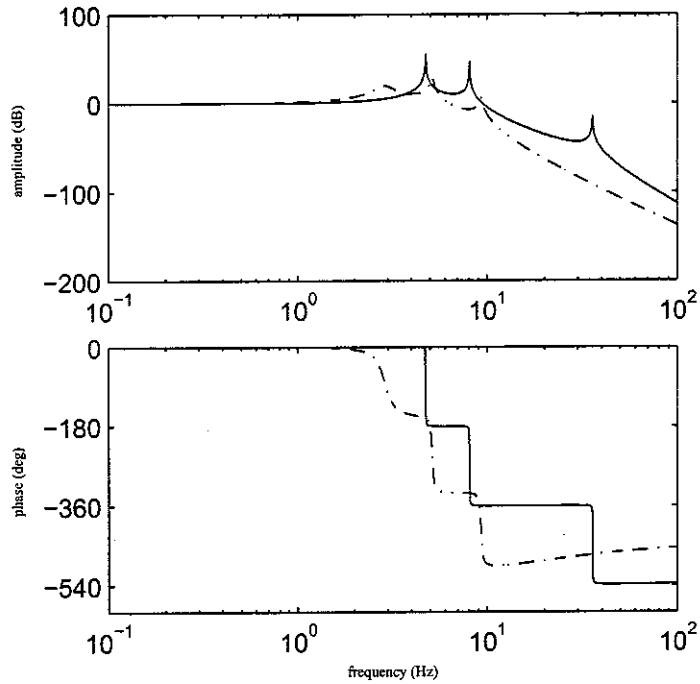

(a) Passive isolation (G_{30} in open-loop), (-) stiff interface (30 Hz interface mode), (dash-dot) isolating interface (3 Hz isolator).

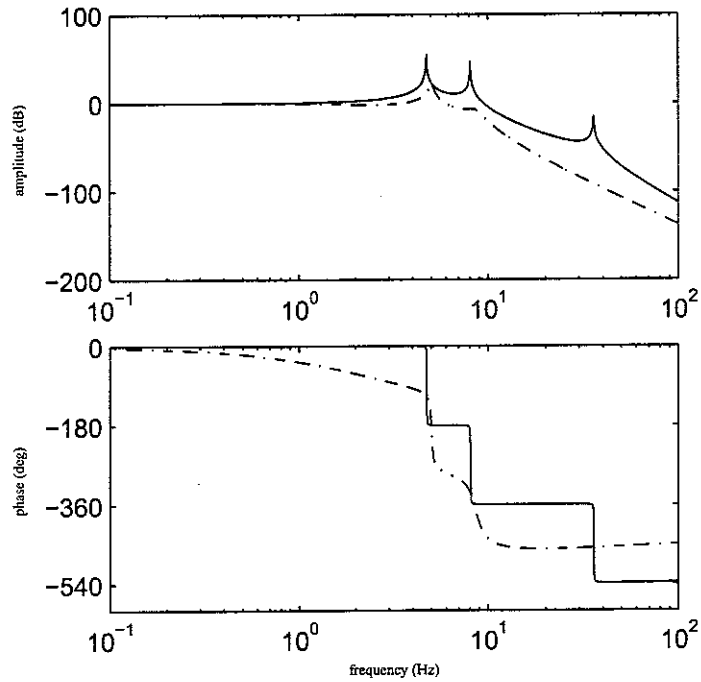

(b) Active isolation (G_{30} in closed-loop), (-) stiff interface (30 Hz interface mode), (dash-dot) isolating interface (3 Hz isolator).

Figure 5.9: Comparison of the payload response with and without isolation.

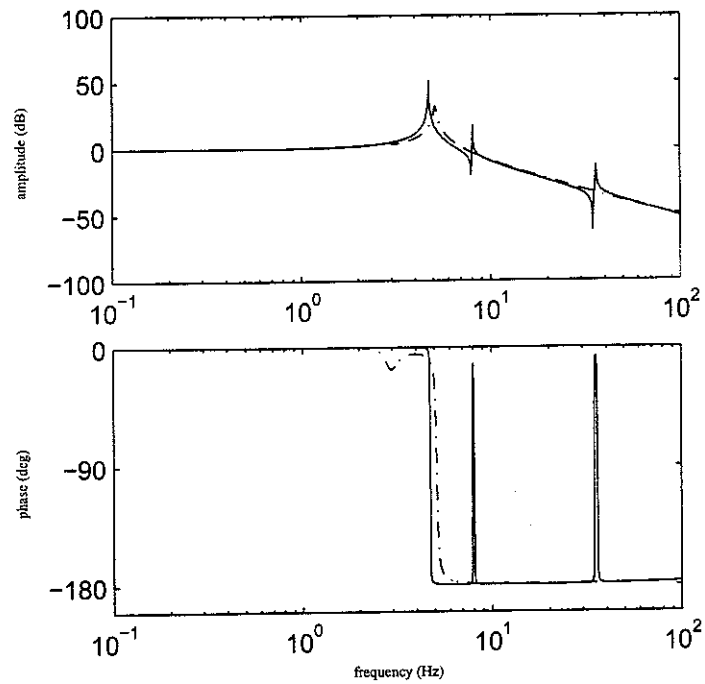

(a) Passive isolation (G_{10} in open-loop), (-) stiff interface (30 Hz interface mode), (dash-dot) isolating interface (3 Hz isolator).

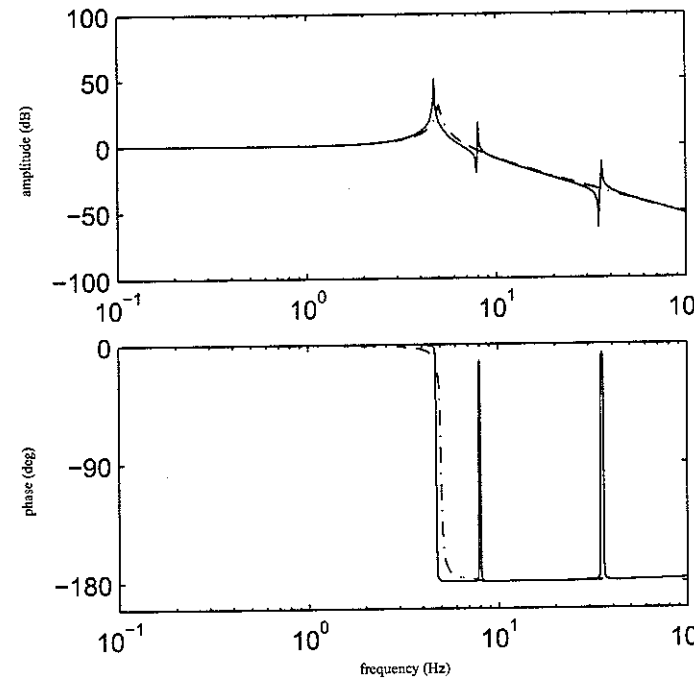

(b) Active isolation (G_{10} in closed-loop), (-) stiff interface (30 Hz interface mode), (dash-dot) isolating interface (3 Hz isolator).

Figure 5.10: Comparison of the base response with and without isolation.

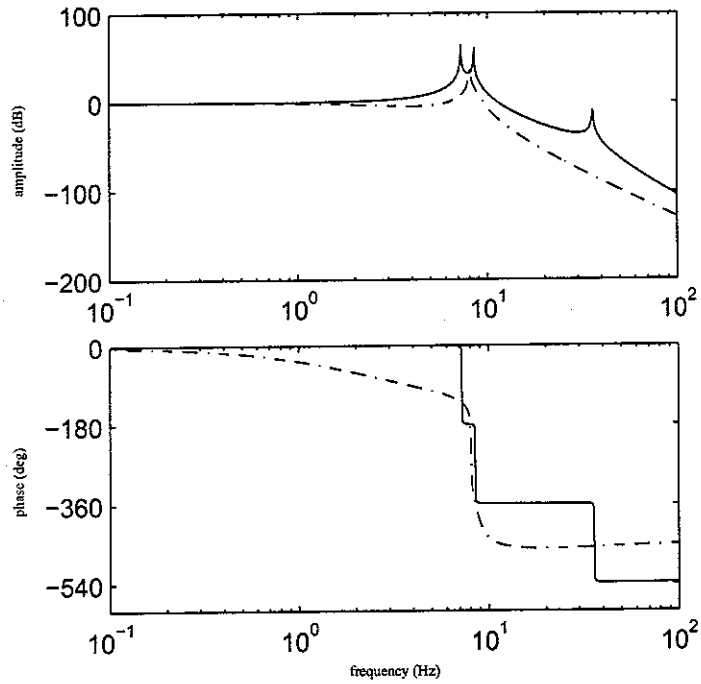

(a) Payload response G_{30}, (-) stiff interface (30 Hz interface mode), (dash-dot) isolating interface (3 Hz isolator).

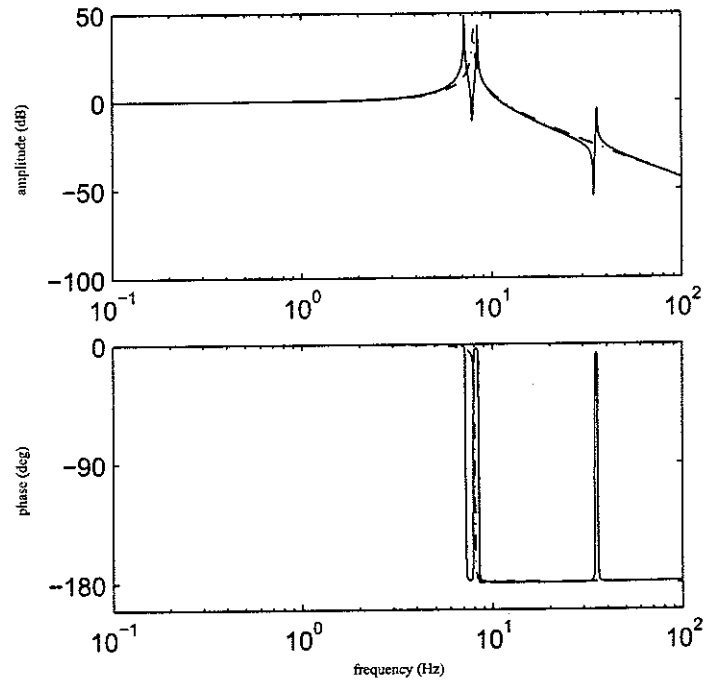

(b) Base response G_{10}, (-) stiff interface (30 Hz interface mode), (dash-dot) isolating interface (3 Hz isolator).

Figure 5.11: Decoupling effect of the isolation system (active) for a case where the base and the payload have a coincident frequency at 8 Hz.

isolation system) rests on the fact that the isolation at high frequency is provided by a soft spring rate while the semi-active (or active) controller provides a strong attenuation of the resonance of the isolation system at low frequency, which entails a transmissibility of 1 at low frequency, or even a slight attenuation. Such a control can be achieved by the well-known skyhook damper strategy, in SISO or multi-SISO control, or by modern control approaches such as LQG in MIMO control.

Under the uncoupled model assumption, once a design of both the mechanical structure and the controller of the isolation system are defined, some criteria regarding performance, stability and eventually robustness must be addressed: are the performance, stability and robustness still guaranteed if a fully coupled model of the system is considered, i.e. a flexible base and payload?.

To illustrate this problem, a single axis system composed of a 1 dof isolation system, 1 dof base and 1 dof payload was considered, taking into account mass, stiffness and damping that are somewhat typical in a launcher configuration. In the single axis configuration, it was shown that the coupling effects are conservative, i.e. that the performance of isolation are not damaged. On the contrary, it seems that the attenuation provided by the isolation system may be even improved locally, around the modes of the base or the payload, due to the appearance of antiresonances very close to these modes and the control authority of the actuator on these modes. This appearance of antiresonances is intrinsic to multiple dof structures due to the properties alternating poles-zeros structures. Because of the typical mass ratios between the base and the payload, performance improvements due to the alternating poles-zeros effect are particularly true for payload modes. **It would be wrong to generalise those observations to a 6 dof isolation system implemented in a launcher because then, the problem is much more complex. However a particular attention has to be paid to see if such effects occur.** Moreover, an aspect has not been studied here. Indeed, the presence of modes in connected structures can reduce stability margins, in the case for example where a payload mode contributes to the signal that is fed back. Even if semi-active control is said to be intrinsiquely stable, because of the passivity constraint, this sort of effects could probably deteriorate the isolation performance. Particular attention on this aspect will have to be paid.

Finally, a property of decoupling by isolation, that is bound to exist in a 6 dof isolation system with a flexible launcher structure and a flexible payload, has been noticed in

the single axis configuration. The isolation system being soft, it tends to decouple the connected structures, making them independent from each other. With this function of decoupling of the isolation system, the studies of coupling between the launcher and the payload structures that are currently carried out before each launch might be avoided, thus enabling the launcher operator to reduce costs and time delays.

CONCLUDING REMARKS

The launch is one of the most severe environments that a spacecraft is subjected to during its lifetime. In this context, whole-spacecraft vibration isolation of axial and lateral loads in the frequency range of 5-100 Hz using smart materials is studied.

Passive isolation systems have been used for a long time because of their simplicity, but they have two major drawbacks. Firstly, they are subject to a stiffness conflict, in so far as there is a trade-off between good isolation at high frequency and limitation of quasi-static deflection. Secondly, there is a conflict in the demand for damping, which consists in a trade-off between isolation at high frequency and control of suspension resonance. Although an active vibration control system is not subject to these trade-offs and has better performance than the best possible passive systems, they are generally more costly, more complex, are potentially unstable and therefore are often less reliable than passive systems.

An alternative to those concepts of vibration isolation is offered by semi-active systems, among which those using controllable damping devices. For tonal vibration, semi-active damping is not subject to the damping conflict, which constitutes a major advantage over passive systems. For broadband disturbances, the performance is more controversial and this report is partly dedicated to this problem. The stiffness conflict exists also for semi-active damping control. For the launch vibration isolation problem, this leads to a trade-off between clearance space and vibration isolation. With the current knowledge of the problem, the isolator natural frequencies should be between 3 and 8 Hz.

Among controllable damping devices, Magneto-Rheological dampers have undeniable advantages such as continuously variable damping, simple geometry (no movable parts), and improved bandwidth. However, their behaviour is highly non-linear. Their modeling is necessary for realistic simulations of semi-active control, but this is a hard task. This report presents a phenomenological model, consisting in a non-linear viscous element (three parameters), in series with an elastic element (two parameters). The identification procedure is presented and the model is compared to the experimental measurements for

sinusoidal motions. There is a good correlation (less than 10% error) in the ranges of currents and frequencies that concern the application of control.

Once a correct model of the MR damper is available, the simulation of semi-active control using an MR damper is possible. This report is dedicated to the single degree-of-freedom isolation problem. The simulations have two main goals. The first one is to have a physical insight on the limitations of performance of SA control. By simplifying the problem using an idealised controllable damper model, it was possible to determine limiting factors of performance, which are the minimum damping ratio, the maximum damping ratio, and the response time of the damper. By optimising the mechanical and control parameters of the SA mount, it was possible to determine a satisfactory design for the experimental rig implemented. Moreover, a major result has been found: the deterioration of performance generally observed for broadband disturbances (compared to narrowband disturbances) is not due to the way SA control inherently operates, but to the various time delays present in controllable damping devices. In other words, this deterioration is not due to the control itself but to the actuation technology, which can be improved.

The second goal of the simulations is to predict the controller, i.e. the control strategy and the control parameters, prior to an experimental investigation. These simulations were useful because there does not exist any theory of semi-active control, contrary to linear active control. Through simulations, an interesting controller has been determined, so-called clipped continuous control with a force feedback loop, which performs much better than clipped on-off methods. Its performance has been tested experimentally for tonal as well as broadband disturbances. The broadband tests confirm that the implementation of a semi-active mount improves significantly the performance of a passive mount. In particular, we conclude that, for the considered broadband case, with this controller, semi-active isolation is not subject to the damping conflict, despite the technological limitations (especially the time delays), contrary to passive isolation. This constitutes a major advantage for semi-active isolation and fully justifies the cost of complexity induced by an SA mount in a single degree of freedom system.

This study has to be extended to multiple degrees of freedom systems. In real systems, the multiple degrees of freedom come from the nearby structures that we want to isolate, which are flexible structures, or from the multiple degrees of freedom of the isolation system itself, and generally from both structures. This report ends with some preliminary

results on a single axis multiple dof system. This study tends to show that the assumption of rigid adjacent structures is quite satisfactory in a first approach, since it gives conservative performance of isolation. However, the presence of modes in connected structures can complicate the control problem and reduce stability margins in an active case. Even if semi-active control is said to be intrinsiquely stable, because of the passivity constraint, this would probably result in a deterioration of isolation performance. Particular attention on this aspect will have to be paid.

REFERENCES

[1] D. C. Karnopp, "Active and semiactive vibration isolation," *Journal of Vibrations and Acoustics*, vol. 117, pp. 177–185, 1995.

[2] J. D. Carlson, D. N. Catanzarite, and K. A. S. Clair, "Commercial magneto-rheological fluid devices," in *5th Int. Conf. on ER Fluids, MR Suspensions and Associated Technology* (W. Bullough, ed.), World Scientific, pp. 20–28, 1996.

[3] M. R. Jolly, J. W. Bender, and J. D. Carlson, "Properties and applications of commercial magnetorheological fluids.," in *Smart Structures and Materials*, vol. 3327 of *Proc. SPIE*, pp. 262–275, 1998.

[4] R. Phillips, *Engineering applications of fluids with a variable yield stress.* PhD thesis, University of California, Berkeley, California., 1969.

[5] L. Pang, G. Kamath, and N. Wereley, "Analysis and testing of a linear stroke magnetorheological damper," in *AIAA/ASME/AHS Adaptive Structures Forum* (N. M. Wereley, ed.), vol. 98-2040. of *AIAA*, pp. 2841–2856, 1998.

[6] N. Wereley and L. Pang, "Nondimensional analysis of semi-active electrorheological and magnetorheological dampers using approximate parallel plate models," *Smart Mater. Struct.*, vol. 7, p. 732743, 1998.

[7] K. D. Weiss, J. D. Carlson, and D. A. Nixon, "Viscoelastic properties of magneto- and electro-rheological fluids.," *Journal of Intelligent Material Systems and Structures*, vol. 5, p. 772775, 1994.

[8] G. Yang, *Large-scale magnetorheological fluid damper for vibration mitigation: modeling, testing and control.* PhD thesis, University of Notre Dame, Indiana, 2001.

[9] X. Wang and F. Gordaninejad, "Flow analysis of field-controllable, electro- and magneto-rheological fluids using herschel-bulkley model," *Journal of Intelligent Material Systems and Structures*, vol. 10, pp. 601–608, 1999.

[10] R. Stanway, J. Sproston, and A. El-Wahed, "Application of electro-rheological fluids in vibration control: a survey," *Smart Mater. Struct.*, vol. 5, pp. 464–482, 1996.

[11] N. D. Sims and N. M. Wereley, "Modelling of smart fluid dampers," in *Smart Structures and Materials: Damping and Isolation*, vol. 5052 of *Proc. SPIE*, pp. 163–174, 2003.

[12] P. Jean, R. Ohayon, and D. L. Bihan, "Payload/launcher vibration isolation: Mr dampers modeling with fluid compressibility and inertia effects through continuity and momentum equations," in *9nth International Conference on ER Fluids and MR Suspensions*, World Scientific, 2004.

[13] N. Phan-Thien, M. Newberry, and R. Tanner, "Non-linear oscillatory flow of a soft solid-like viscoelastic material," *J. Non-Newtonian Fluid Mech.*, vol. 92, p. 6780, 2000.

[14] N. D. Sims, N. J. Holmes, and R. Stanway, "A unified modelling and model updating procedure for electrorheological and magnetorheological vibration dampers," *Smart Mater. Struct.*, vol. 13, pp. 100–121, 2004.

[15] R. Stanway, J. Sproston, and N. Stevens, "Non-linear modelling of an electro-rheological vibration damper.s," *J. Electrostatics*, vol. 20, p. 167184, 1987.

[16] D. Gamota and F. Filisko, "Dynamic mechanical studies of electrorheological materials: moderate frequencies.," *J. Rheology*, vol. 35, pp. 399–425, 1991.

[17] G. Kamath and N. Wereley, "A nonlinear viscoelasticplastic model for electrorheological fluids.," *Smart Materials and Structures*, vol. 6, p. 351359, 1997.

[18] N. Makris, S. Burton, D. Hill, and M. Jordan, "Analysis and design of er damper for seismic protection of structures.," *J. Engineering Mechanics*, vol. 122, p. 10031011, 1996.

[19] N. Makris, S. Burton, and D. Taylor, "Electrorheological damper with annular ducts for seismic protection applications.," *Smart Materials and Structures*, vol. 5, p. 551564, 1996.

[20] F. Gandhi and W. Bullough, "On the phenomenological modeling of electrorheological and magnetorheological fluid preyield behavior," *Journal of Intelligent Material Systems and Structures*, vol. 16, pp. 237–248, 2005.

[21] W. H. Li, H. Du, G. Chen, S. Yeo, and N. Guo, "Nonlinear viscoelastic properties of mr fluids under large-amplitude-oscillatory-shear," *Rheol. Acta*, vol. 42, p. 280286, 2003.

[22] B. F. S. Jr., S. J. Dyke, M. K. Sain, and J. D. Carlson, "Phenomenological model for magnetorheological dampers.," *J. Engineering Mechanics*, vol. 123, p. 230238, 1997.

[23] H. Gavin, "Multi-duct er dampers," *Journal of Intelligent Material Systems and Structures*, vol. 12, pp. 353–366, 2001.

[24] J. Claracq, J. Sarrazin, and J. Montfort, "Viscoelastic properties of magnetorheological fluids," *Rheol. Acta*, vol. 43, p. 3849, 2004.

[25] D. C. Karnopp, M. J. Crosby, and R. A. Harwood, "Vibration control using semi-active force generators," *Journal of Engineering for Industry*, vol. 96, pp. 619–626, 1974.

[26] D. C. Karnopp and A. K. Trikha, "Comparative study of optimization techniques for shock and vibration isolation," *Journal of Engineering for Industry*, vol. 91, pp. 1128–1132, 1969.

[27] E. K. Bender, "Optimum linear control of random vibrations," in *Joint Automatic Control Conference*, Proc. JACC, pp. 135–143, 1967.

[28] O. Yoshida and S. J. Dyke, "Seismic control of nonlinear benchmark building using smart dampers," *Journal of Engineering Mechanics*, vol. 130, pp. 386–392, 2004.

[29] D. H. Wang and W. H. Liao, "Ride quality improvement ability of semi-active, active and passive suspension systems for railway vehicles," in *Smart Structures and Materials* (A. M. Baz, ed.), vol. 5056 of *Proc. SPIE*, pp. 201–212, 2003.

[30] H. Du, K. Y. Sze, and J. Lam, "Semi-active h_∞ control of vehicle suspension with magneto-rheological dampers," *Journal of Sound and Vibration*, vol. 283, pp. 981–996, 2005.

[31] T. Kawabe, O. Isobe, Y. Watanabe, S. Hanba, and Y. Miyasato, "New semi-active suspension controller design using quasi-linearization and frequency shaping," *Control Engineering Practices*, vol. 6, pp. 1183–1191, 1998.

[32] Y. T. Choi and N. M. Wereley, "Vibration control of a landing gear system featuring electrorheological/magnetorheological fluids," *Journal of Aircraft*, vol. 40, pp. 432–439, 2003.

[33] Y. T. Choi, N. M. Wereley, and Y.-S. Jeon, "Semi-active vibration isolation using magnetorheological isolators," in *Smart Structures and Materials*, vol. 4697 of *Proc. SPIE*, pp. 284–291, 2002.

[34] T. Sun, Z. Huang, and D. Chen, "Signal frequency-based semi-active fuzzy control for two-stage vibration isolation system," *Journal of Sound and Vibration*, vol. 280, pp. 965–981, 2005.

[35] Z. D. Xu, Y. P. Shen, and Y. Q. Guo, "Semi-active control of structures incorporated with magnetorheological dampers using neural networks," *Smart materials and structures*, vol. 12, pp. 80–87, 2003.

[36] D. C. Batterbee and N. D. Sims, "Vibration isolation with smart fluid dampers: a benchmarking study," *Smart Structures and Systems*, vol. 1, pp. 235–256, 2005.

[37] A. Preumont, *Vibration control of active structures - An introduction - 2nd edition.* Solid Mechanics and its Applications - Kluwer Academic Press, 2002.

[38] Z. G. Ying, W. Q. Zhu, and T. T. Soong, "A stochastic optimal semi-active control strategy for er/mr dampers," *Journal of Sound and Vibration*, vol. 259, pp. 45–62, 2003.

[39] S. Savaresi, E. Silani, and S. Bittanti, "Acceleration-driven-damper (add): an optimal control algorithm for comfort-oriented semiactive suspensions," *Journal of dynamic systems, measurement and control*, vol. 127, pp. 218–229, 2005.

[40] H. Gavin and C. Alhan, "Guidelines for low-transmissibility semi-active vibration isolation," *Smart Materials and Structures*, vol. 14, pp. 297 – 306, 2005/04.

[41] P. D. Man, P. Lemerle, P. Mistrot, J. P. Vershueren, and A. Preumont, "An investigation of a semi-active suspension for a lift truck," in *Proceedings of Euromech Colloquium of Semi-active Vibration Suppression*, pp. 1–14, 2004.

[42] J. H. Koo, F. D. Goncalves, and M. Ahmadian, "Investigation of the response time of magnetorheological fluid dampers," in *Smart Structures and Materials*, vol. 5386 of *Proc. SPIE*, pp. 63–71, 2004.

[43] D. Fischer and R. Isermann, "Mechatronic semi-active and active vehicle suspensions," *Control Engineering Practices*, vol. 12, pp. 1353–1367, 2003.

[44] X. M. Dong, M. Yu, S. L. Huang, Z. Li, and W. M. Chen, "Half car magnetorheological suspension system accounting for nonlinearity and time delay," in *9nth International Conference on ER Fluids and MR Suspensions*, World Scientific, 2004.

[45] C. Park and D. Jeon, "Semi-active control of a smart seat with an mr fluid damper considering its time delay," *Journal of Intelligent Material Systems and Structures*, vol. 13, pp. 521–524, 2002.

[46] S. J. Dyke, B. F. S. Jr., M. K. Sain, and J. D. Carlson, "Modeling and control of magnetorheological dampers for seismic response reduction.," *Smart Materials and Structures*, vol. 5, p. 565575, 1996.

[47] H. Yoshioka, J. C. Ramallo, and B. F. Spencer, "Smart base isolation strategies employing magnetorheological dampers," *J. Engineering Mechanics*, vol. 128, pp. 540–551, 2002.

[48] N. McLellan, "On the development of a real-time embedded digital controller for heavy truck semiactive suspensions," Master's thesis, Faculty of Virginia Tech, 1998.

[49] J. Lagarias, J. Reeds, M. Wright, and P. Wright, "Convergence properties of the nelder-mead simplex method in low dimensions," *SIAM Journal of Optimization*, vol. 9, pp. 112–147, 1998.

[50] Y. Lee and D. Jeon, "A study on the vibration attenuation of a driver seat using an mr fluid damper," *Journal of Intelligent Material Systems and Structures*, vol. 13, pp. 437–441, 2002.

[51] J. Den Hartog, *Mechanical vibrations*. McGraw Hill, N.Y., 1947.

[52] D. Thayer, M. Campbell, and J. Vagners, "Six axis vibration isolation using modern control techniques," in *21st Annual AAS Guidance and Control Conference*, American Astronautical Society, pp. 1–15, 1998.